SYNCHROTRON TEXTURE ANALYSIS OF FINE GRAINED EARTH MATERIALS

by

Michael Jugle

A thesis submitted to the faculty of
The University of Utah
in partial fulfillment of the requirements for the degree of

Master of Science

in

Geophysics

Department of Geology and Geophysics

The University of Utah

August 2017

The University of Utah Graduate School

STATEMENT OF THESIS APPROVAL

The thesis of **Michael Jugle**

has been approved by the following supervisory committee members:

Lowell Miyagi	, Chair	**5/30/2017** Date Approved
Fan-Chi Lin	, Member	**5/30/2017** Date Approved
Waruntorn Kanitpanyacharoen	, Member	**5/30/2017** Date Approved

and by **Thure Cerling**, Chair of

the Department of **Geology and Geophysics**

and by David B. Kieda, Dean of The Graduate School.

ABSTRACT

Synchrotron x-ray diffraction can be a useful tool in the study of fine grained materials. The highly focused, high energy beams combined with fast 2-dimensional detectors allow for the quantitative study of crystallographic preferred orientation (texture) of these difficult to study materials. Here, two different studies were done that demonstrate the range of applications for this technique.

Shales display a large degree of seismic anisotropy, largely due to texturing of clay minerals. Eleven samples from the Green River and Mancos Shale formations were studied. P- and S-wave velocities were calculated based on orientation distributions obtained through Rietveld analysis. P-wave anisotropy was found to range from 0.4% to 7.1% in Green River samples, and from 1.8% to 7.6% in Mancos Shale samples. This is found to be similar to, but generally lower than, that of other shales previously studied around the world. This is due to lower average clay volume fractions in the Green River and Mancos samples studied here. The clay volume fraction and the intrinsic P-wave anisotropy in the samples studied here and in previous work show a linear correlation.

The D" region of the lower mantle lies just above the core mantle boundary and exhibits complex seismic anisotropy. The post-perovskite phase of $(Mg,Fe)SiO_3$ is thought to be one of the main mineral phases here, and it is possible that texturing (preferred orientation) of the mineral is responsible for a large portion of the seismic anisotropy observed in the D". Texture development in other post-perovskite structured

compounds, including $MgSiO_3$, $MgGeO_3$, and $CaIrO_3$, have been studied. In this thesis, a new experiment was done on the $NaMgF_3$ post-perovskite analog in order to further the study of these compounds. $NaMgF_3$ perovskite was found to develop a strong (100) texture. $NaMgF_3$ post-perovskite, synthesized from the perovskite phase, was found to have an initial texture of (130) oriented at high angles to compression. Upon compression, a secondary maximum near (001) develops, consistent with a dominant slip on (001)[100].

TABLE OF CONTENTS

LIST OF FIGURES

LIST OF TABLES

PREFACE

Crystallographic preferred orientation, or texture, is an important characteristic of many materials. Texture in a rock composed of anisotropic crystals can result in bulk anisotropy of physical properties such as thermal and electric conductivity, magnetic properties, and elastic properties. Deposition of anisotropically shaped crystals, crystal growth, and deformation can result in the development of texture. This can be further modified by phase transformations and recrystallization. In Earth materials, texture can provide information about magnetic fields, depositional processes, temperature gradients, and deformation. In geophysics, one of the most important properties related to texturing is seismic anisotropy.

There are several different methods available for the measurement of texture, including conventional x-ray goniometry, neutron diffraction, electron back-scatter diffraction (EBSD), and synchrotron x-ray diffraction, which is the method used here. Conventional x-ray goniometry is quick and inexpensive; however, pole figures can only be adequately measured if the diffraction peaks of a material are sufficiently far apart. This limits its usefulness to samples with a very low number of phases (Wenk & Van Houtte, 2004). Additionally, penetration depth is limited, so x-ray goniometry is primarily surface sensitive rather than representing a volume average. Neutron diffraction has a very low absorption in most materials, making it useful for large samples and thus yielding volume averaged textures. Low attenuation also gives the ability to use sample

environment cells, for controlling temperature and/or pressure. Some of the disadvantages of neutron diffraction include its slow data collection and analysis (Wenk & Van Houtte, 2004). EBSD provides localized information about orientations or misorientations and is able to see microstructure and subgrains, as samples are analyzed in a grid-pattern (Randle & Engler, 2000). EBSD only provides information about the surface of a sample, though there are techniques such as focused ion beam (FIB) milling, which are destructive. EBSD can also be problematic for analyzing samples with very fine and poorly crystalline grains, such as clay minerals. Clays typically have defects and stacking faults, which make it difficult to obtain good EBSD patterns. Additionally, it can be difficult to get a high enough surface polish for EBSD on clays.

The use of synchrotron x-ray sources for texture measurements is relatively new. It has only been since the mid-1990s that sources and fast detectors capable of being used to measure texture have been utilized (Wenk & Grigull, 2003). Synchrotrons provide several key advantages over other techniques, including the ability to provide very high intensity, highly focused x-ray beams of short wavelengths. The high intensity beams allow for faster, higher resolution data and better peak separation, eliminating some of the problems with conventional x-ray sources. The use of area detectors allows one to record full Debye rings as diffraction images, increasing pole figure coverage. Additionally, synchrotron x-rays in transmission geometry can penetrate much thicker samples than conventional x-rays, and are able to obtain volume averaged textures. Synchrotron x-ray diffraction provides some advantages over neutron diffraction. Neutron diffraction is useful for bulk materials due to its low absorption, and has advantages for very large and coarse-grained samples. However, the high energy beams

of the synchrotron can penetrate relatively thick (cm scale) samples, and data collection is significantly faster than neutron diffraction (Wenk, 1991). Synchrotron x-ray detectors can capture diffraction images in seconds or minutes, rather than the hours needed for neutron diffraction.

Synchrotron diffraction is also useful for samples in a diamond anvil cell (DAC) under high pressure. EBSD is unable to provide in-situ measurements at high pressures, and would not be useful unless the sample is quenchable. In order to generate high pressures in the DAC, sample sizes need to be very small. The small (several μm) beam size of the synchrotron x-ray beam allows for the diffraction of the sample, while avoiding diffraction from the DAC and gasket assembly. In general, neutron diffraction beams are too large to accomplish this.

In this thesis, synchrotron x-ray diffraction was used in two separate experiments. Shale samples from the Green River and Mancos Shale formations were analyzed, demonstrating this technique's ability to measure texture in fine grained, multiphase samples. Intrinsic anisotropy was calculated using the measured texture. The second experiment is a high-pressure deformation experiment of $NaMgF_3$ in the DAC. In-situ texture measurements were taken while increasing pressure, showing deformation and transformation textures. These provide insight into deformation mechanisms and slip systems.

CHAPTER 1

CLAY TEXTURE AND SEISMIC ANISOTROPY IN THE GREEN RIVER AND MANCOS SHALES

Introduction

The study of shales has become increasingly important due to their role as hydrocarbon source rocks and reservoirs, as well as their role as cap rocks. They are also viable targets for CO_2 and nuclear sequestration. Shales are composed largely of platey, elastically anisotropic phyllosilicate clay minerals. During deposition, compaction, and lithification, these clay minerals develop the preferred orientations (texture) that control the bulk anisotropic elastic properties of shale. This results in seismic anisotropy. Seismic anisotropy is controlled by texture and elastic anisotropy of the constituent mineral phases, fractures, and porosity, as well as fluids that may be present (Hornby, 1994; Sayers, 1994). It has been found that intrinsic anisotropy, due to texturing of minerals, is the dominant source of anisotropy in shales (Allan, Kanitpanyacharoen, & Vanorio, 2015). Quantitative studies of clay textures in shales are difficult due to their very fine grain size and poor crystallinity. Methods of studying texture using synchrotron x-ray diffraction have been developed recently, and have been applied to a limited number of shale formations (Easley, 2014; Kanitpanyacharoen, Wenk, Kets, Lehr, & Wirth, 2011; Lonardelli, Wenk, & Ren, 2007; Voltolini, Wenk, Mondol, Bjorlykke, &

Jahren, 2009; Wenk, Voltolini, Kern, Popp, & Mazurek, 2008b; Wenk, Voltolini, Mazurek, van Loon, & Vinsot, 2008a).

The anisotropic properties of shale are a concern for seismic surveys, particularly as they relate to hydrocarbon exploration. Shales comprise roughly 75% of rocks in typical sedimentary basins and act as both source rocks and reservoir seals (Jones & Wang, 1981). In many cases, shales are assumed to be isotropic for the purposes of developing models in seismic surveys. This assumption can lead to significant errors, particularly in regards to depth (Banik, 1984). Shale formations, if bedding is close to horizontal, can cause units to appear deeper than they actually are. Seismic models can be improved if anisotropy is taken into consideration. However, anisotropy is difficult to constrain as it can vary widely. As cores samples are commonly taken during hydrocarbon exploration, shale samples can easily be studied for mineralogy. One of the goals of this study is to establish a method to estimate anisotropy based on the clay content of a shale.

The shale samples used in this study come from the Mancos Shale and the Green River formation. The samples used have been studied previously using sedimentological methods (e.g., DOE, 2011; Horton, 2012). Neither formation has been studied for texture. Synchrotron x-ray diffraction data were collected, and then analyzed using a Rietveld analysis to obtain texture information for the minerals present in each sample, with a particular interest in clay minerals. Compressional (P) and shear (S) wave velocities for the bulk samples were calculated based on mineral texture information, in combination wih single crystal elastic properties. Calculated properties were compared to other shales around the world on which similar studies have been conducted.

Geologic Setting

Geologic Setting of the Mancos Shale

The geology of the western part of North America during the Late Cretaceous was largely controlled by the subduction of the Farallon plate underneath the North American plate. The result of this subduction was the thickening of the crust in the region through thrusting and folding (Livaccari, 1991). Low angle thrust fault systems are ubiquitous in the region. The older thrusts faults tend to be mostly towards the west, with the younger faults being more to the east. Younger thrust faults are typically lower angle than the western faults and are associated with the Sevier orogeny (Dickinson et al., 1988). These thrust faults resulted in a crustal shortening of roughly 100 km in Utah, and produced a structural relief of approximately 25 km (DeCelles, 1994). A foredeep basin was formed to the east of the thrust systems by subsidence from the loading of the crust. This newly formed Rocky Mountain foreland basin then began to be filled with sediment (Decelles & Giles, 1996)

The Western Interior Seaway covered much of North America during the Cretaceous, with several hundreds of meters of sediment accumulating in the various basins around the Seaway (Kauffman, 1977). The Mancos Shale was first described in Colorado in the Mancos River Valley (Cross & Purington, 1899). Outcrops of the Mancos Shale formation can be found around southern and southeastern Utah. The Mancos Shale was deposited from 95-75 Ma. It was deposited as a marine shale across the Uinta Basin, and averages approximately 4000 ft. thick throughout the Basin (Council, 2009). A map of the Western Interior Seaway and the Uinta Basin is shown in Figure 1.

The Mancos Shale is considered to be a more distal expression of units deposited

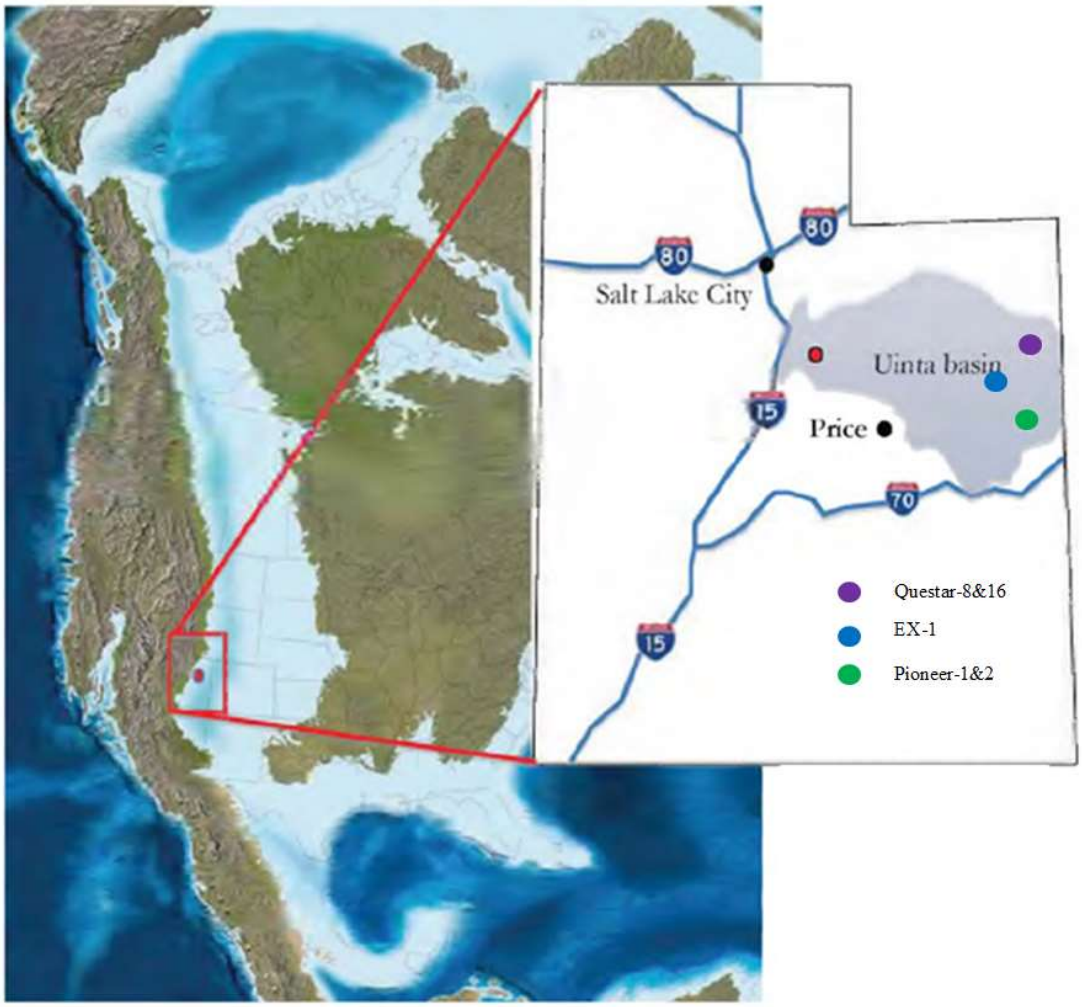

Figure 1: Map of the Cretaceous Western Interior Seaway and the location of the Uinta Basin. Locations wells Questar-8 & 16, Pioneer-1&2 and EX-1 are shown.
(Modified from Kennedy, 2011)

more proximal to the source. Some of these more proximal units are the Ferron and Emery Sandstones, and the Blackhawk formation. Multiple transgressions and regressions of the Interior Seaway are recorded in these units during the late Cretaceous (Yoshida, 2000). In the western portion of the Mancos Shale, it can be found interfingered with these more coarse-grained formations.

After the Mancos Shale was deposited, the tectonic setting changed from the Sevier style of deformation, to the Laramide style of deformation. The Laramide orogeny is characterized by faults that extend deep into the basement rocks, whereas the Sevier orogeny consisted of more shallow faulting. This is sometimes called thick-skinned deformation and thin-skinned deformation (Johnson, 2003). Whereas the Sevier orogeny was characterized by north-south trending thrust faults, the Laramide orogeny resulted in a range of fault orientations. The Uinta basin today is thus defined largely by Laramide aged deformation, as the Rocky Mountain foreland basin from the Sevier orogeny was divided up into smaller basins (Figure 2). The boundaries of the Uinta basin are the Uinta uplift to the north, and the San Rafael Swell to the south. To the east, the Douglas Creek Arch separates the Uinta basin from the Piceance Basin.

Geologic Setting of the Green River Formation

During the Eocene, the Rocky Mountain region was dominated by large lake systems in the various basins that were created by the Laramide orogeny. The Green River formation consists of lacustrine sediments that were deposited in the Rocky Mountain basins during the Eocene. These sediments represent a broad range of facies, ranging from fresh water to hypersaline lake environments (Smith, Singer, & Carroll, 2003)

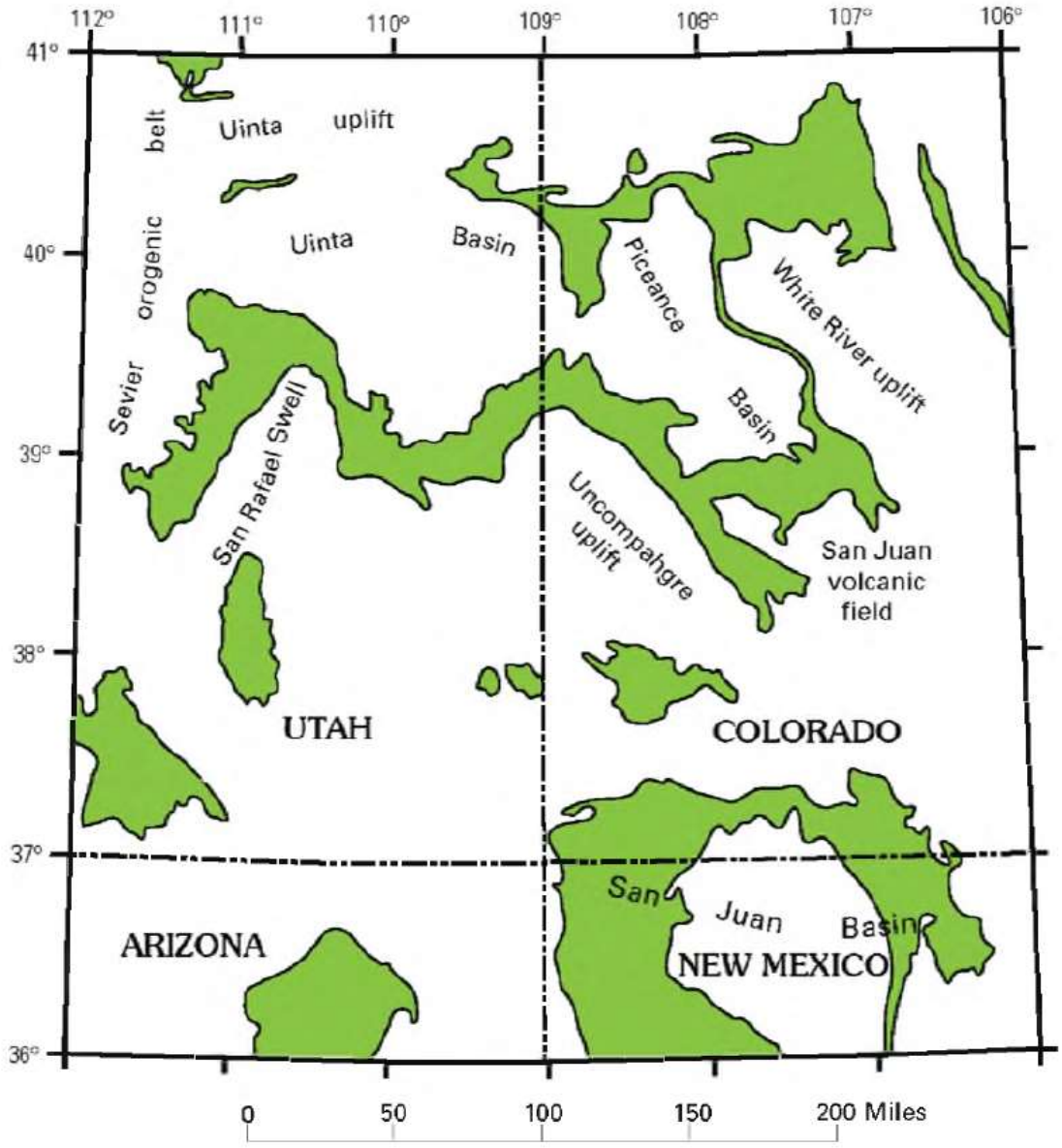

Figure 2: Map Illustrating the Uinta basin region. Green denotes outcrops of Cretaceous rocks. Laramide age structures include the Uinta uplift, the San Rafael Swell, and the Uncompahgre Uplift.

(Modified from Johnson, 2003)

In addition to lake deposits, the Green River formation is also found interfingered in some places with alluvial deposits of the same age associated with the Wasatch Formation (Carroll & Bohacs, 1999). The Eocene lake system in its associated Rocky Mountain basins is show in Figure 3. The Green River formation is also a major source of oil shale. In the Uinta basin alone, there exists approximately 77 billion barrels of oil that can potentially be extracted (Vanden Berg, 2008).

Datasets

In this study, 11 samples from the Green River formation and Mancos Shale were used. The samples used represent a variety of locations and depths in these formations. All samples were taken from the Uinta basin from well cores that have been previously studied. Figure 1 shows were these wells are located in the Uinta basin. The Mancos Shale samples were previously studied in Horton (2012), and the Green River samples in DOE (2011).

Questar Red Wash #8ML-6-9-24

Questar Red Wash #8ML-6-9-24 is a gas well that was drilled by Questar in the Natural Buttes field approximately 25 miles south of Vernal, Utah. This core will be referred to as Questar 8. The well was drilled to a depth of 13,400 ft., and was cored from 9631 ft. to 9746 ft. The Mancos Shale in this well extends from 9000 ft. to the top of the Frontier Sandstone at 11,700 ft. The well was perforated at 32 intervals between 4462 ft. and 9324 ft., with 6 of them being hydraulically fractured. Initially, this well produced 60 barrels of oil per day, 1438 MCF of gas per day, and 1330 barrels of water

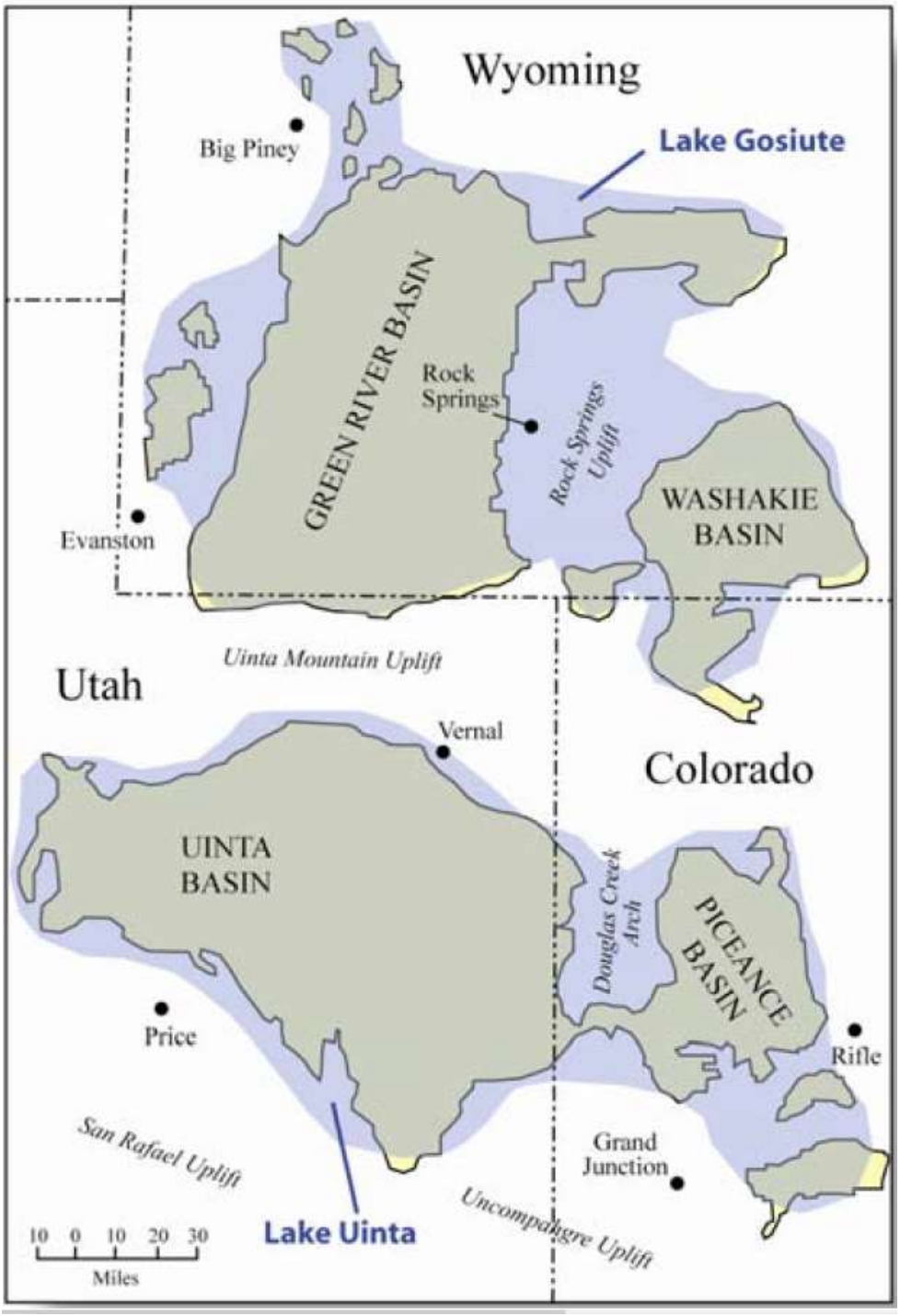

Figure 3: Map of the Eocene Lake system, and associated basins. The Green River formation is the sediment that was deposited in these Lakes.

(Modified from DOE, 2011)

per day (IHS, 2012a). Three samples were used from this well in this study. One was taken from a depth of 9703.4 ft. (referred to as Q8-9703), and one was taken from a depth of 9715.5 feet (referred to as Q8-9715). Q8-9715 exhibited two distinct layers, one being lighter and one being darker. These were treated as two separate samples for this study (Q8-9715-light and Q8-9715-dark).

Questar Glenn Bench #16M-28-8-21

Questar Glenn Bench #16M-28-8-21 is also a gas well in the Natural Buttes field, located near Questar 8. This core will be referred to as Questar 16. This well was drilled to a depth of 16,490 ft. and was cored from 15,145 ft. to 15,263 ft. The Mancos Shale in this well extends from 12,480 ft. to the top of the Dakota Sandstone at 16,040 ft. This well was perforated at 126 different intervals from 10,454 ft. to 16,412 ft., with 15 of these intervals being hydraulically fractured. The well initially produced 2191 MCF of gas per day, and 974 barrels of water per day (IHS, 2012b). Four samples were used from this well in this study. These samples were from depths of 15,160.4 ft. (Q16-15160), 15,172.8 ft. (Q16-15172), 15,223.1 ft. (Q16-15223), and 15,264.1 ft. (Q16-15264).

Pioneer Natural Resources Main Canyon Federal #23-7-15S-23E

This well was drilled by Pioneer Natural Resources approximately 40 miles south of where the Questar wells are located. The well was drilled to a depth of 10,370 ft., with two cored intervals. One interval was from 7480 ft. to 7597 ft., referred to as Pioneer 1, and the second interval was from 6995 ft. to 7135 ft., referred to as Pioneer 2. The Mancos Shale in this well is represented by the interval from 5534 ft. to 8800 ft., at the

top of the Morrison formation. The well was perforated at 5 intervals from 8574 ft. to 9841 ft., with 4 of these intervals being hydraulically fractured. The well initially produced 8 barrels of oil per day, 629 MCF of gas per day, and 73 barrels of water per day (IHS, 2012c). Only one sample was used from the well, from the Pioneer 2 core interval. It was taken from a depth of 7135 ft. and will be referred to as P2-7135.

Green River EX-1 Well

Less information is available for this well than for the Mancos Shale wells. The location of this well is marked on Figure 1. This well was cored from a depth of 1767 ft. to 2969 ft. The Green River formation extends from 1541 ft. to an unspecified depth, beyond the bottom of the cored interval (DOE, 2011). Three samples from this well were used in this study. The depths these samples were taken from is unknown. The samples will be referred to as EX1-013, EX1-036, and EX1-091

Methods

Shales are typically composed of a significant volume fraction of phyllosilicate (clay) minerals, and commonly include quartz, carbonate minerals, and feldspars, although mineralogy can vary widely. Clay minerals display peak broadening during x-ray diffraction due to a number of parameters such as grain size, interlayering, stacking disorders, and microstrain (Wenk et al., 2008a). Sample thickness can also contribute to peak broadening. These factors, along with peak overlaps with other minerals present, make the identification of individual peak positions extremely difficult using conventional methods. A method using hard synchrotron x-ray diffraction was found to

be able to accurately measure the orientation distribution functions (ODF) of phyllosilicate minerals and was first applied to work on slates. Modeling of composition, texture, and microstructure is possible using this method, and can be applied to shales as well (Lonardelli et al., 2007).

Shale samples were prepared by cutting core samples into a square shape with height and width of approximately 3 to 4 cm, and a thickness of approximately 1 cm. Samples were then analyzed using synchrotron x-ray diffraction at beamline 11-1D-C of the Basic Energy Sciences Synchrotron Radiation Center (BESSRC) of the Advanced Photon Source (APS) at Argonne National Laboratory. The experimental setup illustrated in Figure 4 was used. A monochromatic x-ray beam with a wavelength of 0.108040 Å and a beam size diameter of 0.5 mm was used. A Perkin-Elmer flat panel detector with a resolution of 2048x2048 pixels, located approximately 2134 mm from the sample, was used to record diffraction images. Samples were mounted on aluminum rods oriented parallel to the samples' bedding and then attached to a goniometer that rotated around an axis (Figure 4). This axis was defined as the x-axis and the rotation angle was called ω. During exposure, samples were averaged over a -5mm to +5mm scan range along the x-axis with an exposure time of 50 seconds. Additionally, exposures were taken at seven different rotations along ω for each sample, from -45º to +45º at increments of 15º. The rotations and translation about ω and along the x-axis were done to ensure sufficient pole figure coverage and grain statistics. Figure 5 shows a raw diffraction image from sample Q16-15160, at a rotation of 0º. Intensity variations about the Debye rings indicate crystallographic preferred orientation (texture).

The diffraction images were then processed using the Material Analysis Using

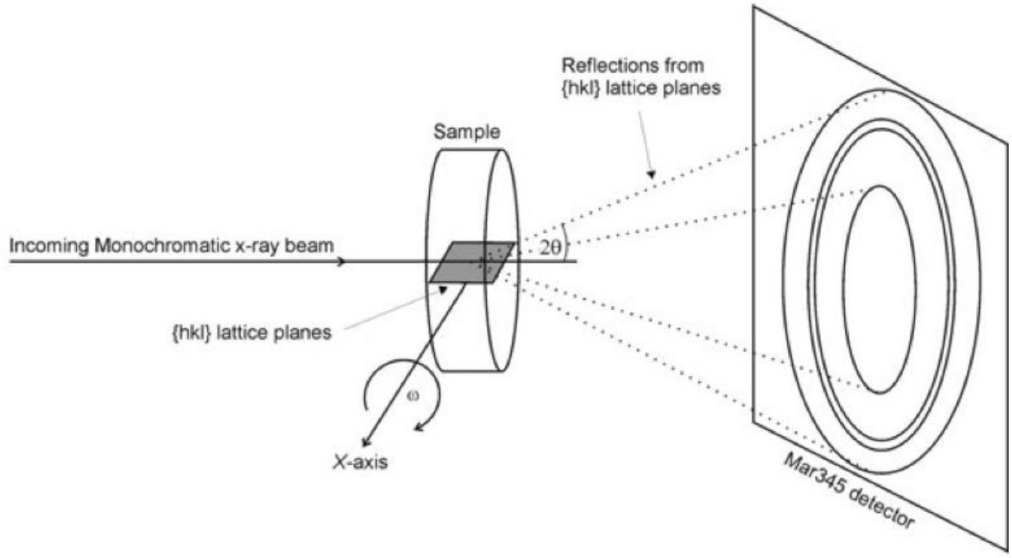

Figure 4: Diagram of the experiment geometry. Samples were translated along the x-axis during each exposure, with 7 exposures taken for each sample, from -45º to +45º at 15º intervals about ω. Also note that a Perkin-Elmer image plate detector was used in place of a Mar345 detector.

(Modified from Kanitpanyacharoen et al., 2011)

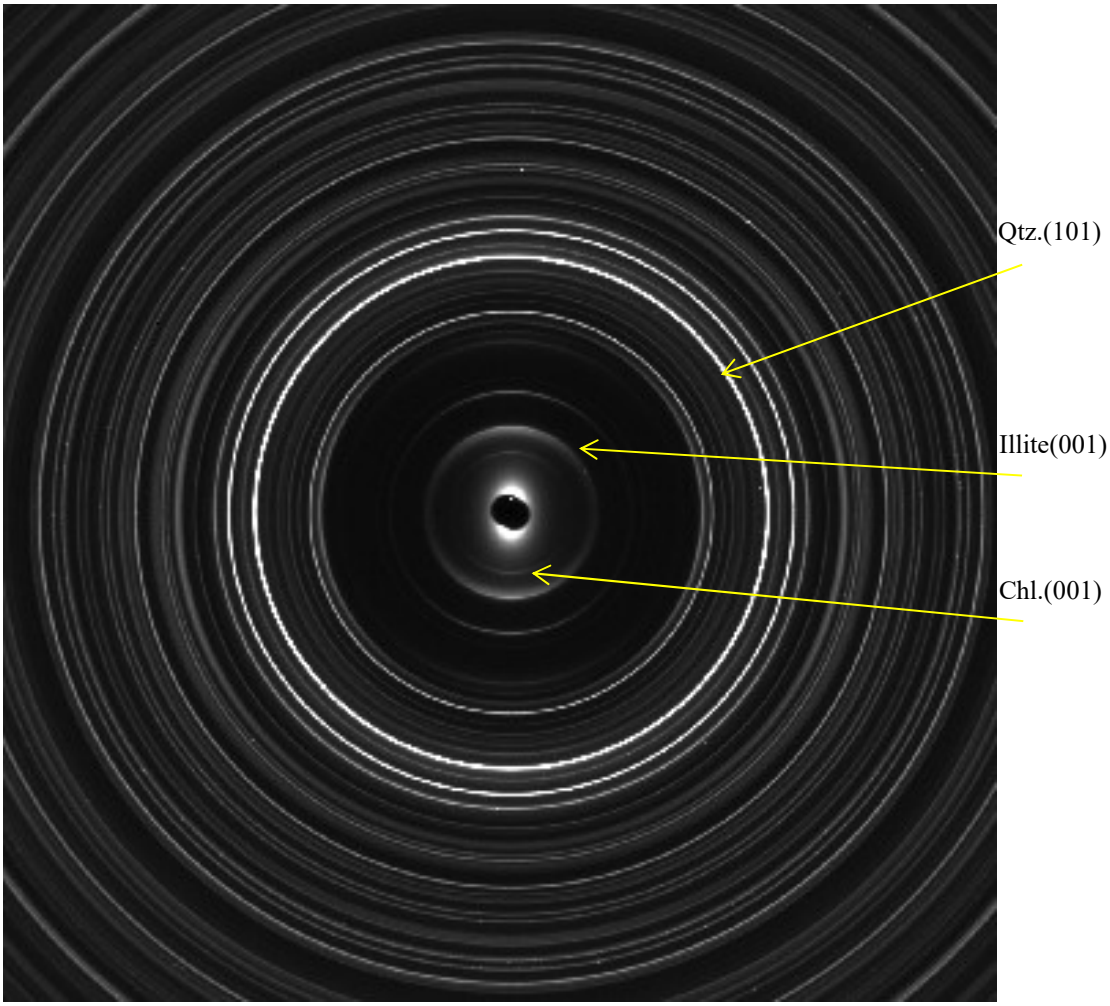

Figure 5: Diffraction image of Q16-15160 at 0º rotation. Intensity variations along Debye rings indicate preferred orientations (texture). Quartz (101, Illite (001), and Chlorite (001) diffraction peaks are denoted.

Diffraction (MAUD) program (Lutterotti, Matthies, Wenk, Schultz, & Richardson, 1997; Wenk et al., 2014). The images were integrated from 0º to 360º azimuth using 10º intervals to produce 36 spectra. A CeO_2 powder standard was used to calibrate the instrument geometry (wavelength, sample to detector distance, beam center, and tilt) before the analysis of the samples. A total of 252 spectra (36 spectra for each of the seven rotations) were used to process each sample. A 2θ range of 0.7º to 3.5º was used for the analysis of each sample. This small 2θ range is used as the d-space of clay mineral is limited, largely due to the high energy of the beam, and also to reduce computation time. MAUD uses a Rietveld algorithm (Rietveld, 1969) that allows for a quantitative texture analysis (Lutterotti et al., 1997). A Rietveld refinement uses a least-squares method to minimize the difference between the collected experiment diffraction data, and a calculated diffraction model. The calculated model is thus created by refining many parameters including crystal unit cell parameters, weight fractions, microstrain, and preferred orientations. This refinement technique is able to successfully resolve overlapping diffraction in peaks that occur in shales (Wenk et al., 2008a). Figure 6 shows the average spectra for both the experimental and computed model for sample Q16-15160.

For the Rietveld refinement, parameters for the crystal structures of each phase are needed. Information for a mineral's symmetry, space group, unit cell parameters, and microstructure are contained within crystallographic information files (CIFs). The CIFs for illite-mica (Gualtieri, 2000), illite-smectite (Plancon, Tsipurski, & Drits, 1985), and chlorite (Joswig, Tagai, Korekawa, & Wenk, 1980) were obtained from the American Mineralogist Open Database. CIFs for other minerals were obtained from the built-in

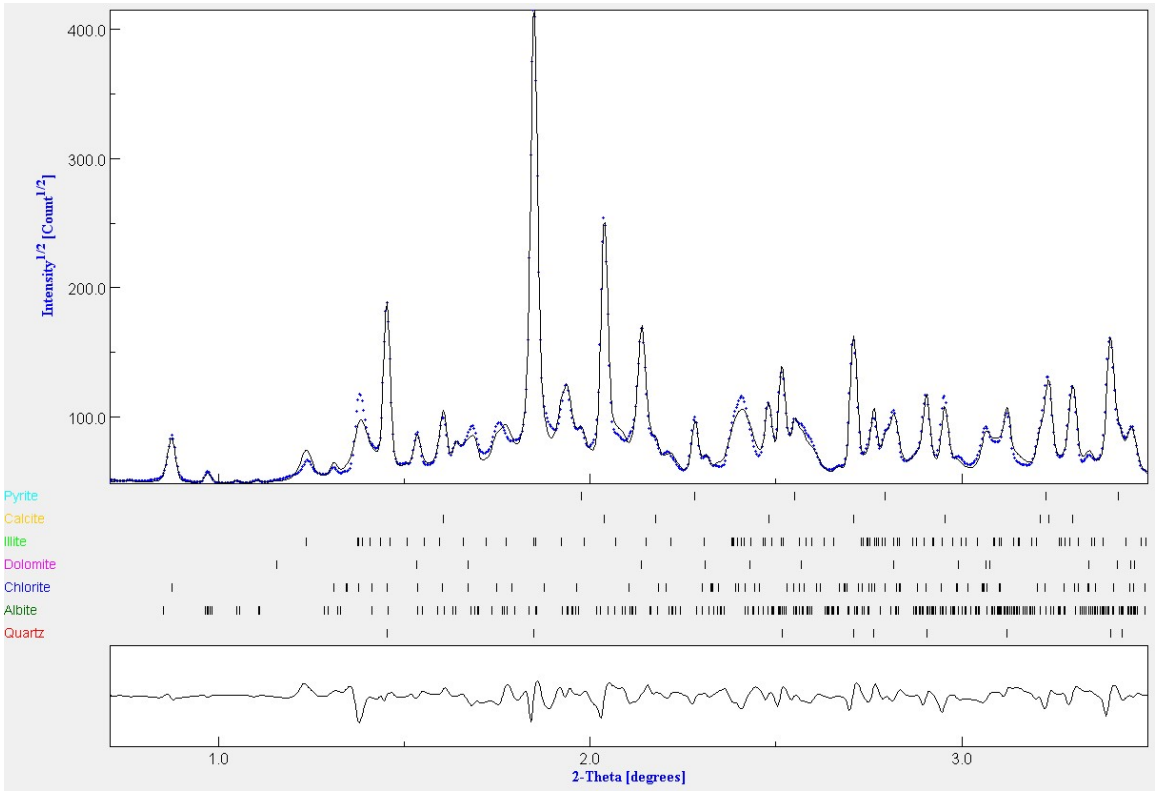

Figure 6. Diffraction profile of sample Q16-15160 over a 2θ of 0.7º to 3.5º using the 0º tilt. Blue dots denote the measure data from the experiment, and the black line is the calculated model. Seven different mineral phases were used to compute the calculated model.

database in MAUD.

Monoclinic minerals are typically described in second setting, where b=[010] is the unique axis and (001) is the cleavage plane. However, for texture calculations in MAUD, first setting must be used, where c=[001] is the unique axis and (100) is the cleavage plane (Matthies & Wenk, 2009). This is a very important distinction that must be made in order for textures to be calculated properly, and can be easily confused if one is not careful. Texture analysis was computed using the EWIMV algorithm. The EWIMV algorithm is similar to the WIMV algorithm (Matthies & Vinel, 1982), but is optimized for incomplete pole figure coverage. A 10º resolution was used, with fiber symmetry imposed to produce an orientation distribution function (ODF) for each mineral phase. Refinements were also done without symmetry imposed to verify that this symmetry was indeed present.

The ODFs were then exported from MAUD into the BEARTEX program (Wenk, Matthies, Donovan, & Chateigner, 1998) for further processing. The ODF defines the probability of the various crystal axes of a mineral to lie within a certain range of orientations with respect to the frame of reference. The ODFs were smoothed in BEARTEX using a 7.5 degree filter and then used to create equal area projection pole figures (Figures 7-28). The smoothed ODFs were then used to calculate the elastic properties for each mineral phase in each sample. The single crystal elastic tensor coefficients (C_{ij}'s) for each mineral phase must be known in order for this to be done. Coefficients for the clay minerals were obtained from Militzer, Wenk, Stackhouse, and Stixrude (2011), and coefficients for quartz, calcite, dolomite, pyrite, and albite were obtained from Bass (1995). The elastic tensor for each mineral phase was calculated by

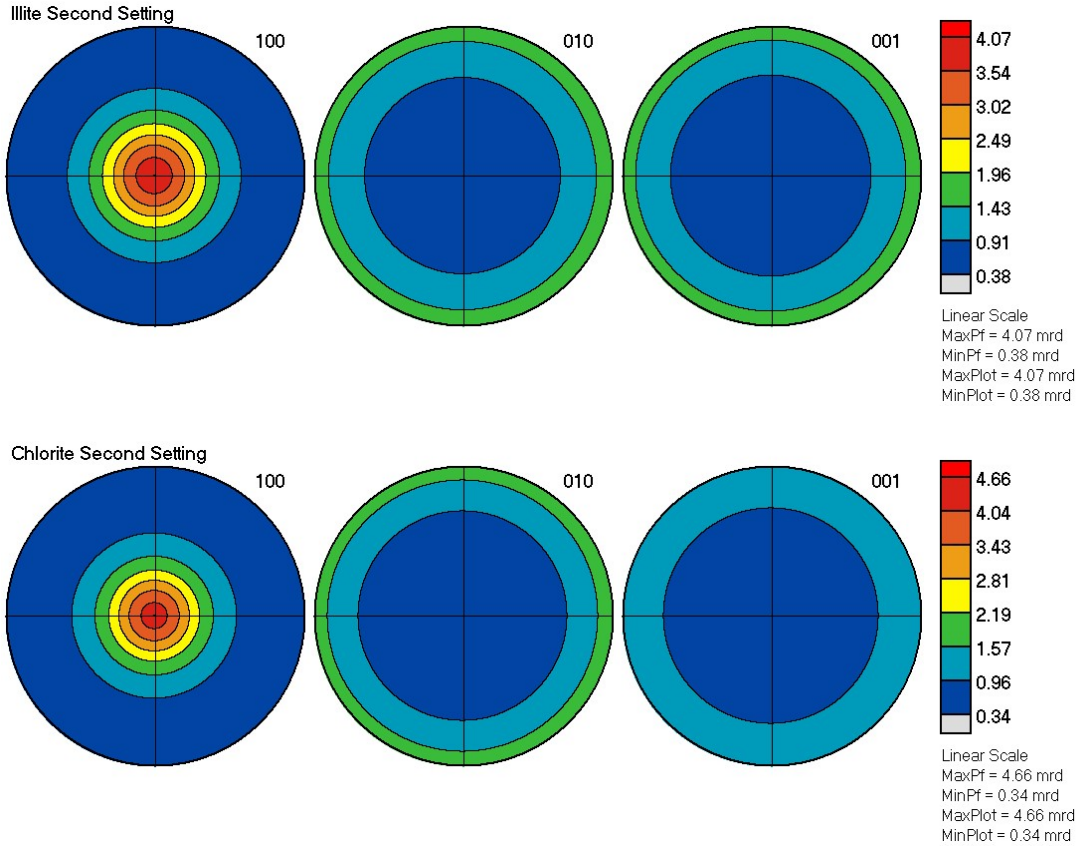

Figure 7. (001), (100), and (010) pole figures for clay phases illite and chlorite in sample Q16_15160. Moderate strength texture is exhibited in clay phases among the studied samples, with a max M.R.D. in clays of around 4 being typical on the (001) basal plane. As noted, monoclinic second setting is used.

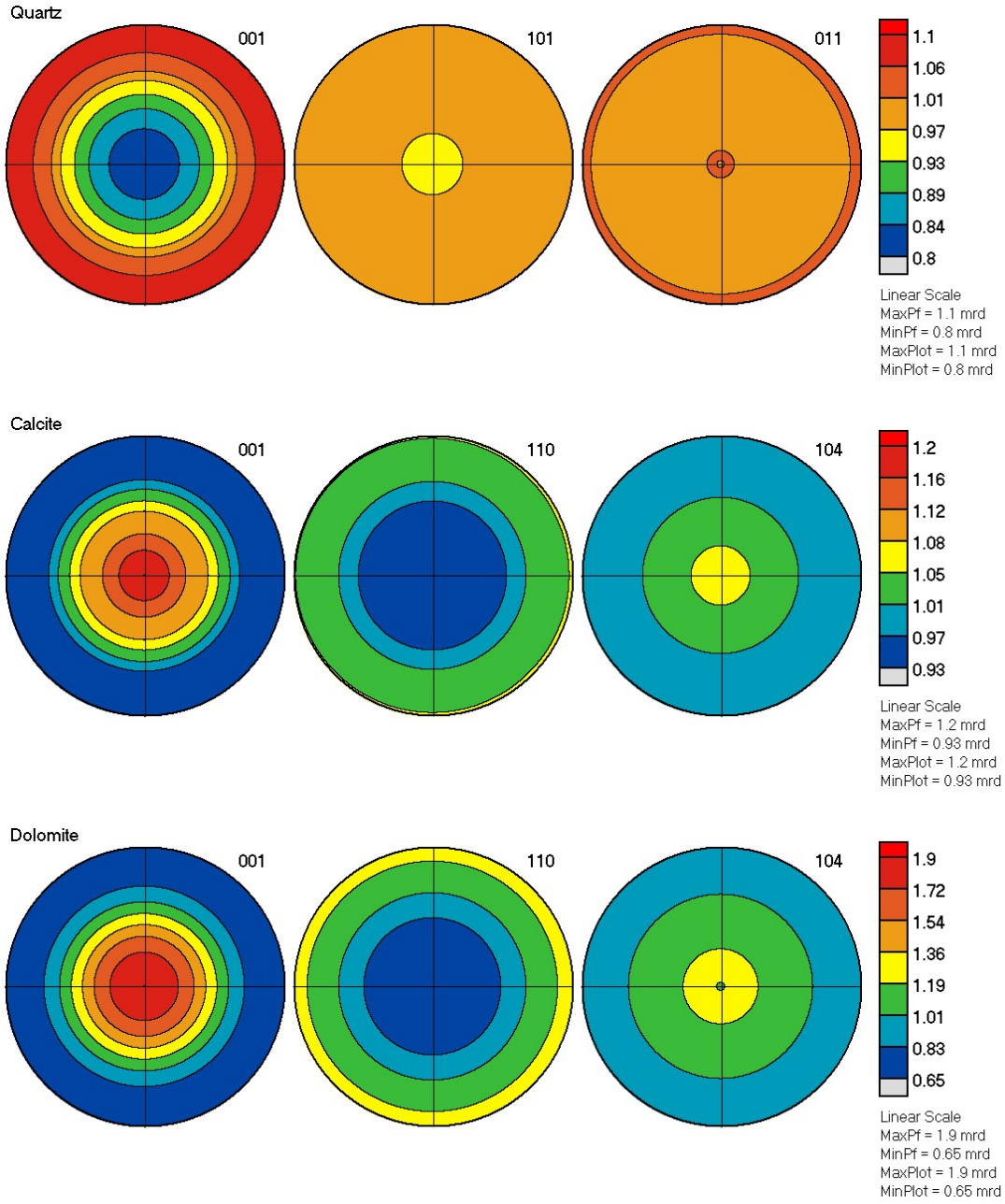

Figure 8. Pole figures for quartz, calcite, and dolomite from sample Q16_15160. Quartz and calcite exhibit almost entirely random distributions, with dolomite displaying a weak (001) texture. With a minor exception for dolomite, these minerals do have much influence on the anisotropy of the sample.

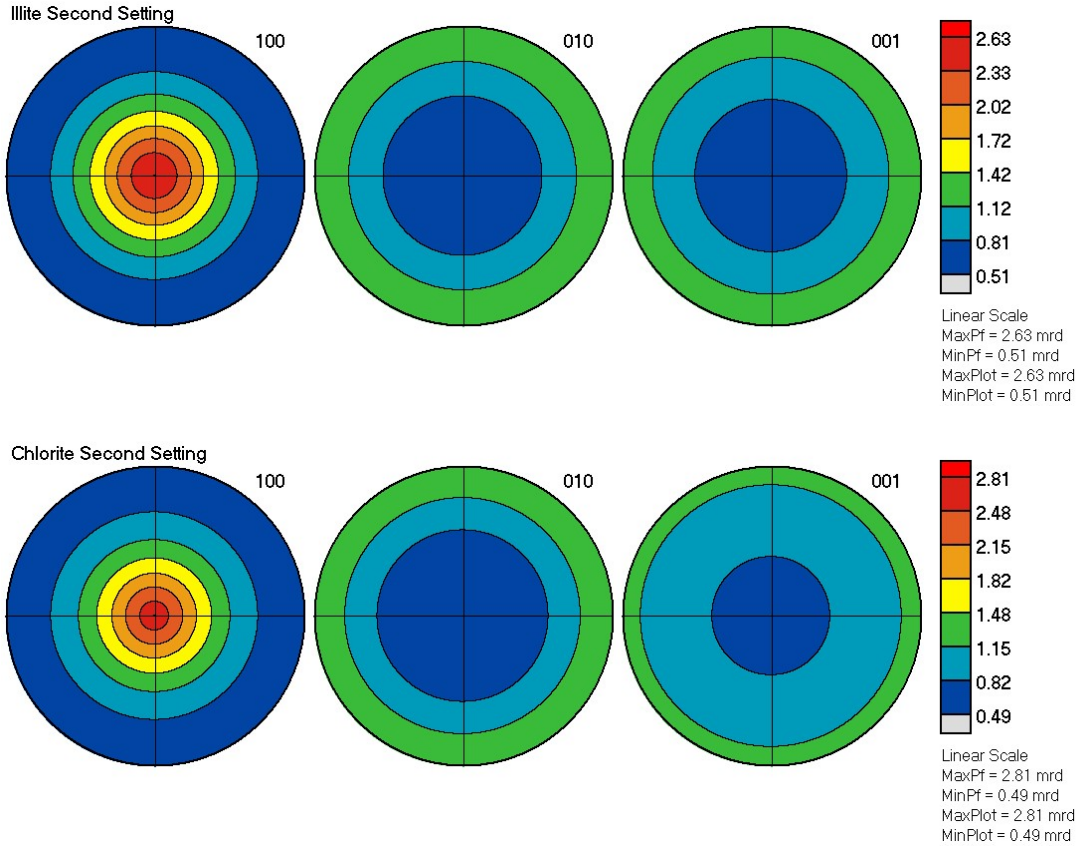

Figure 9. (001), (100), and (010) pole figures for clay phases illite and chlorite in sample Q16_15264.

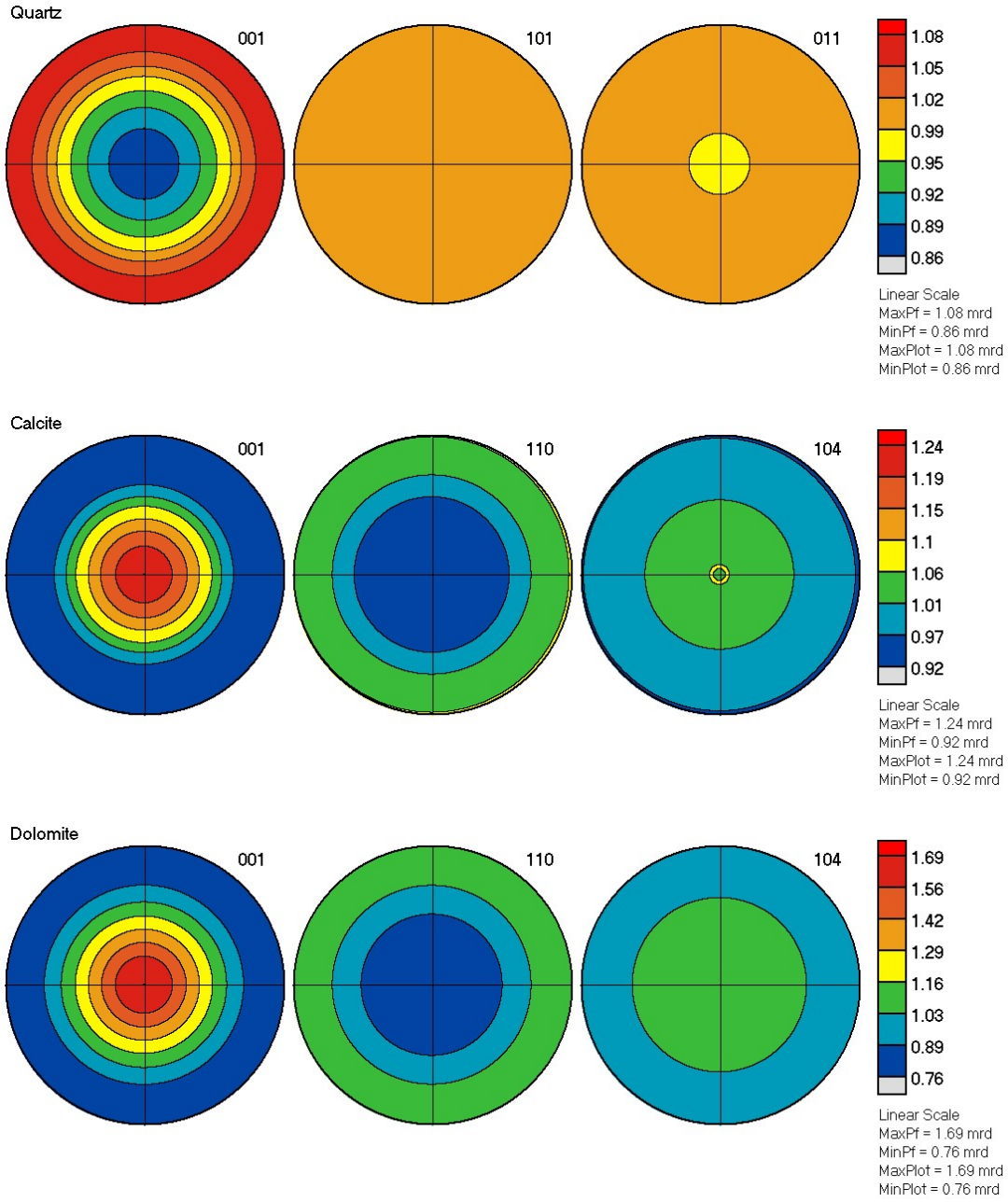

Figure 10. Pole figures for quartz, calcite, and dolomite from sample Q16_15264.

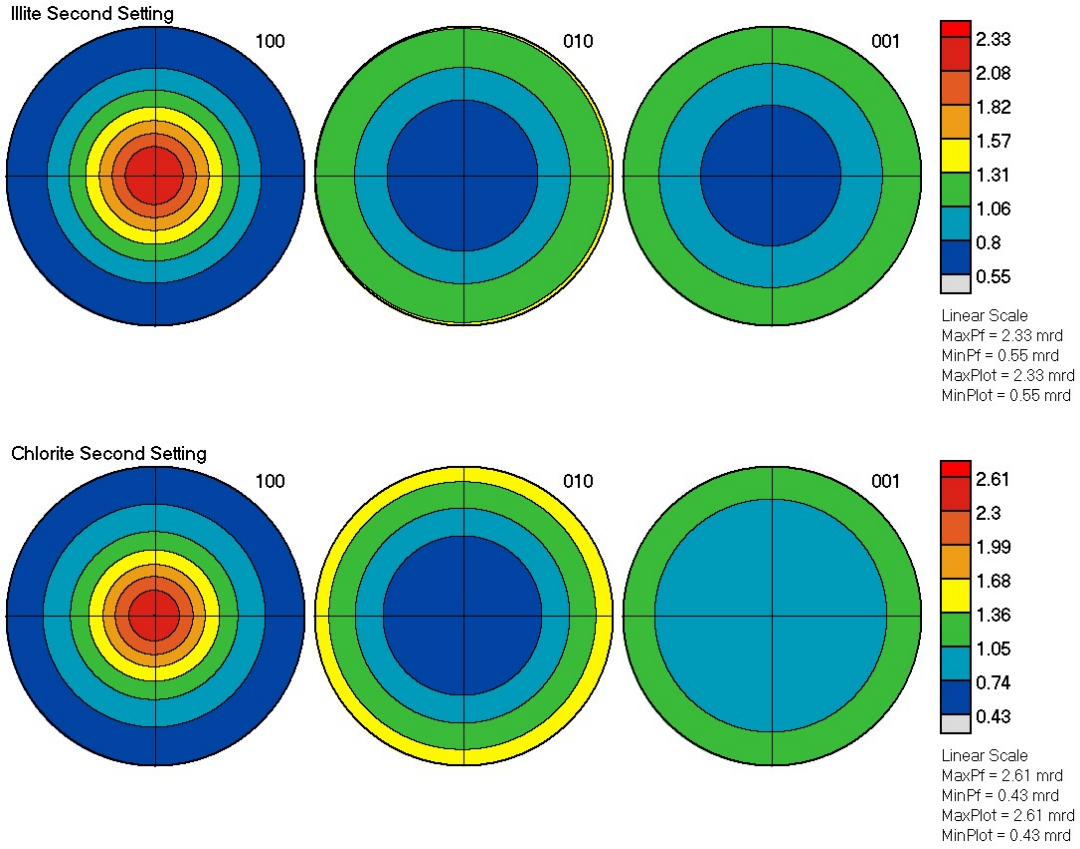

Figure 11. (001), (100), and (010) pole figures for clay phases illite and chlorite in sample Q16_15223.

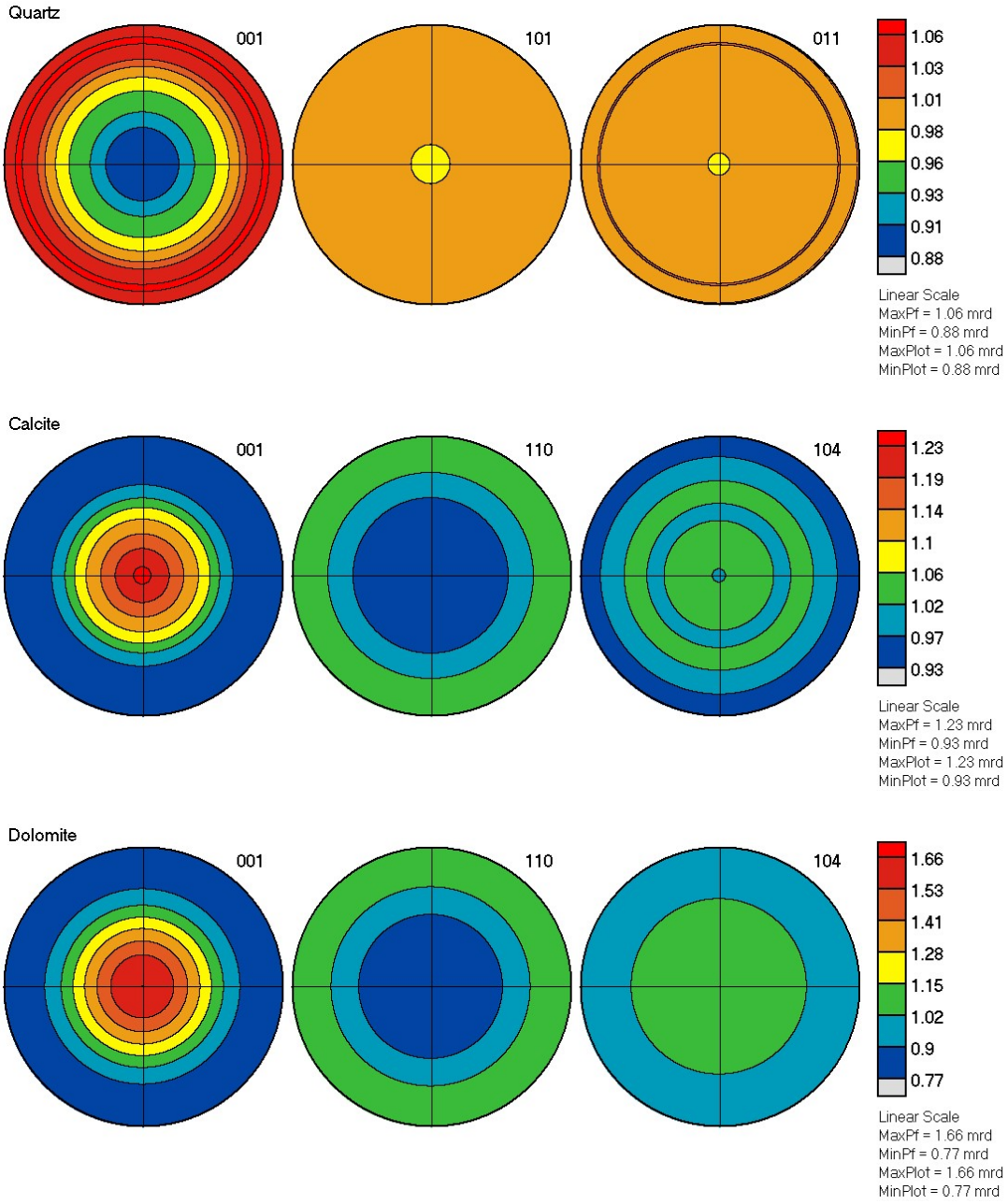

Figure 12. Pole figures for quartz, calcite, and dolomite from sample Q16_15223.

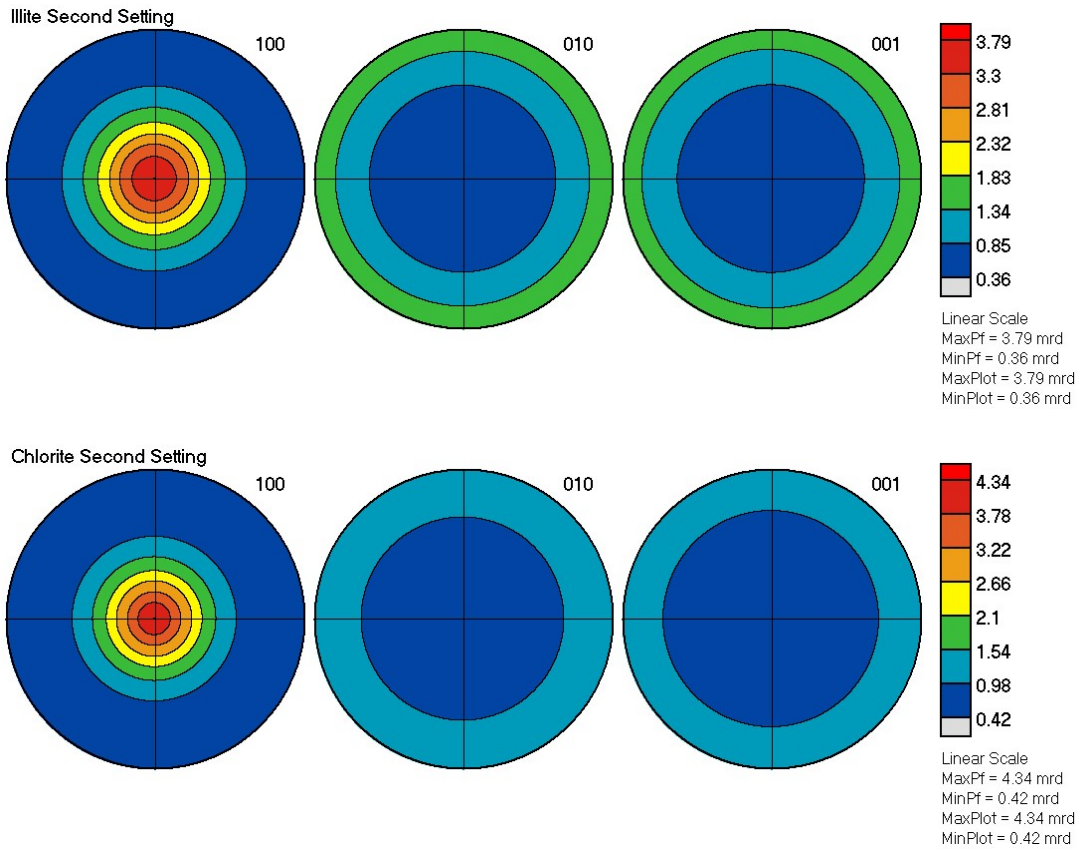

Figure 13. (001), (100), and (010) pole figures for clay phases illite and chlorite in sample Q16_15172.

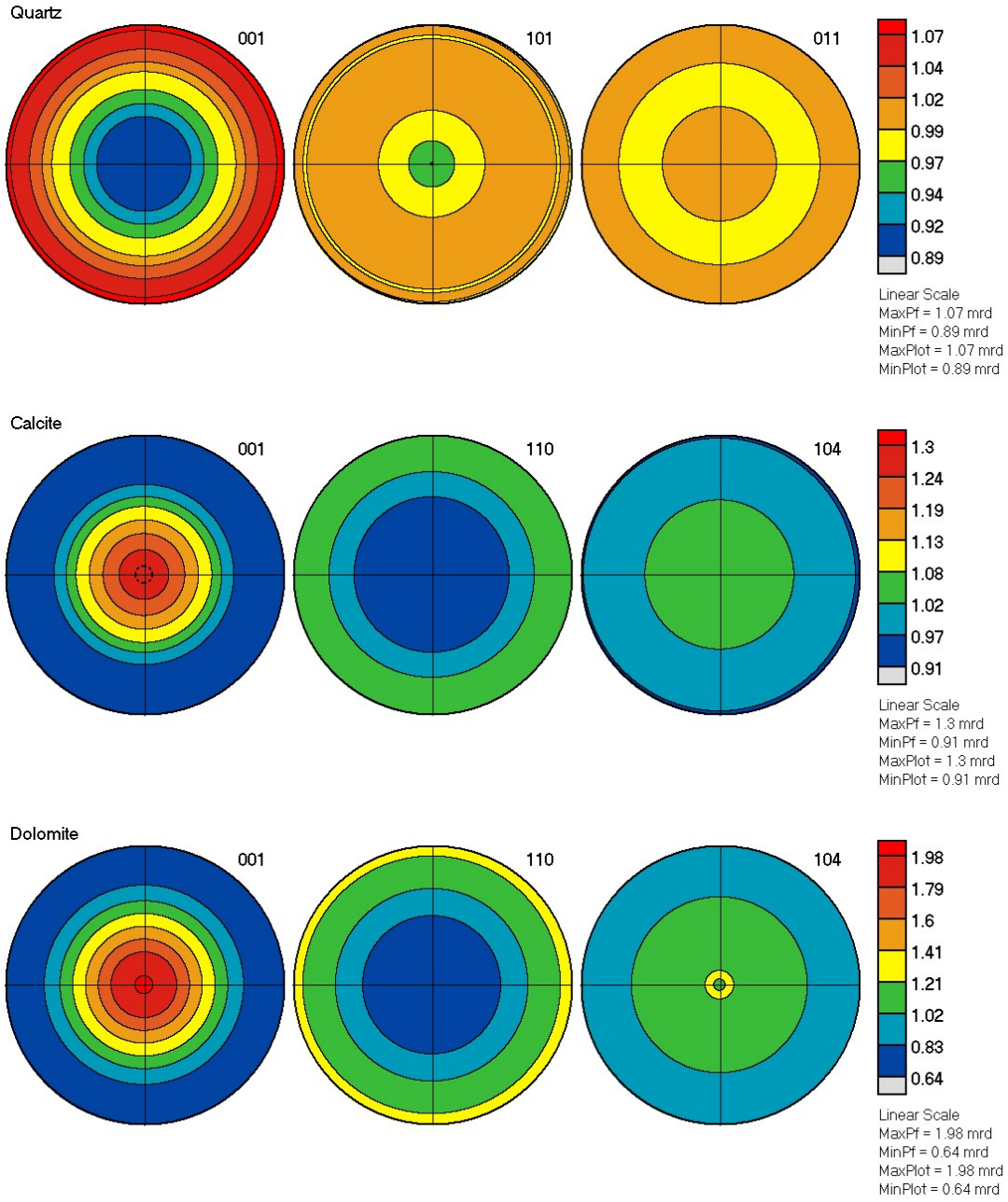

Figure 14. Pole figures for quartz, calcite, and dolomite from sample Q16_15172.

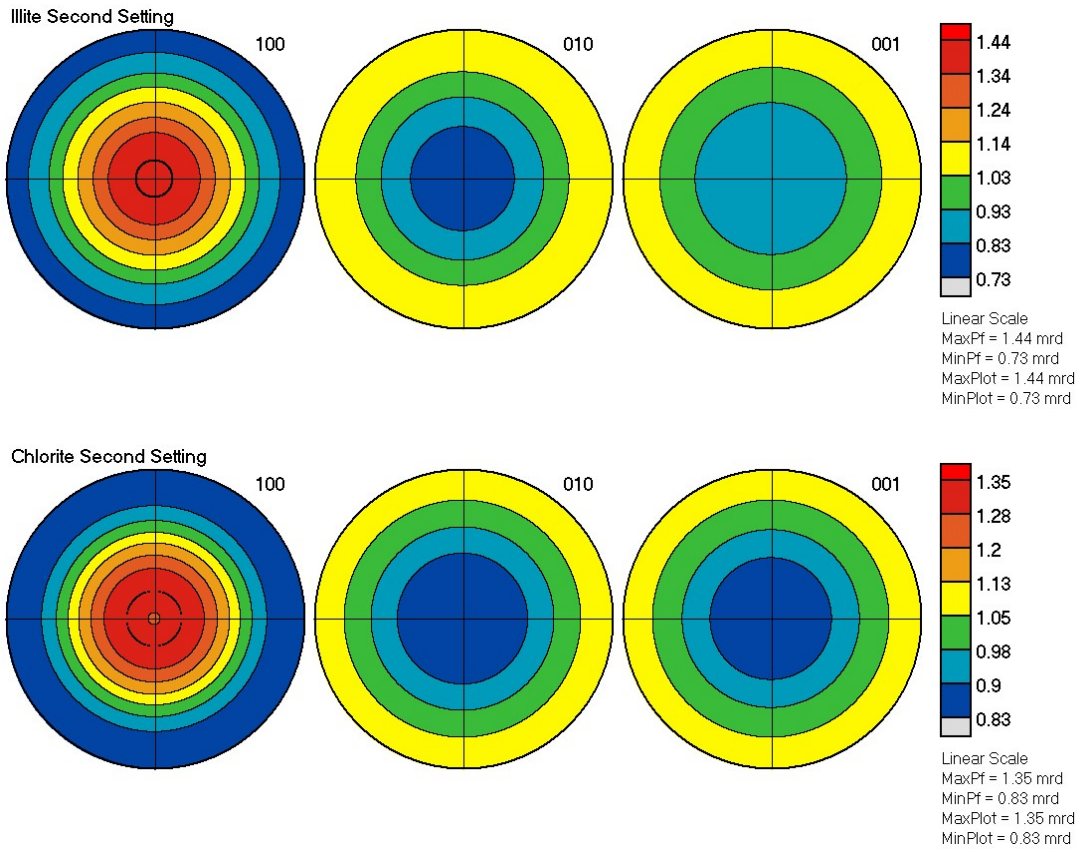

Figure 15. (001), (100), and (010) pole figures for clay phases illite and chlorite in sample Q8_9715_light.

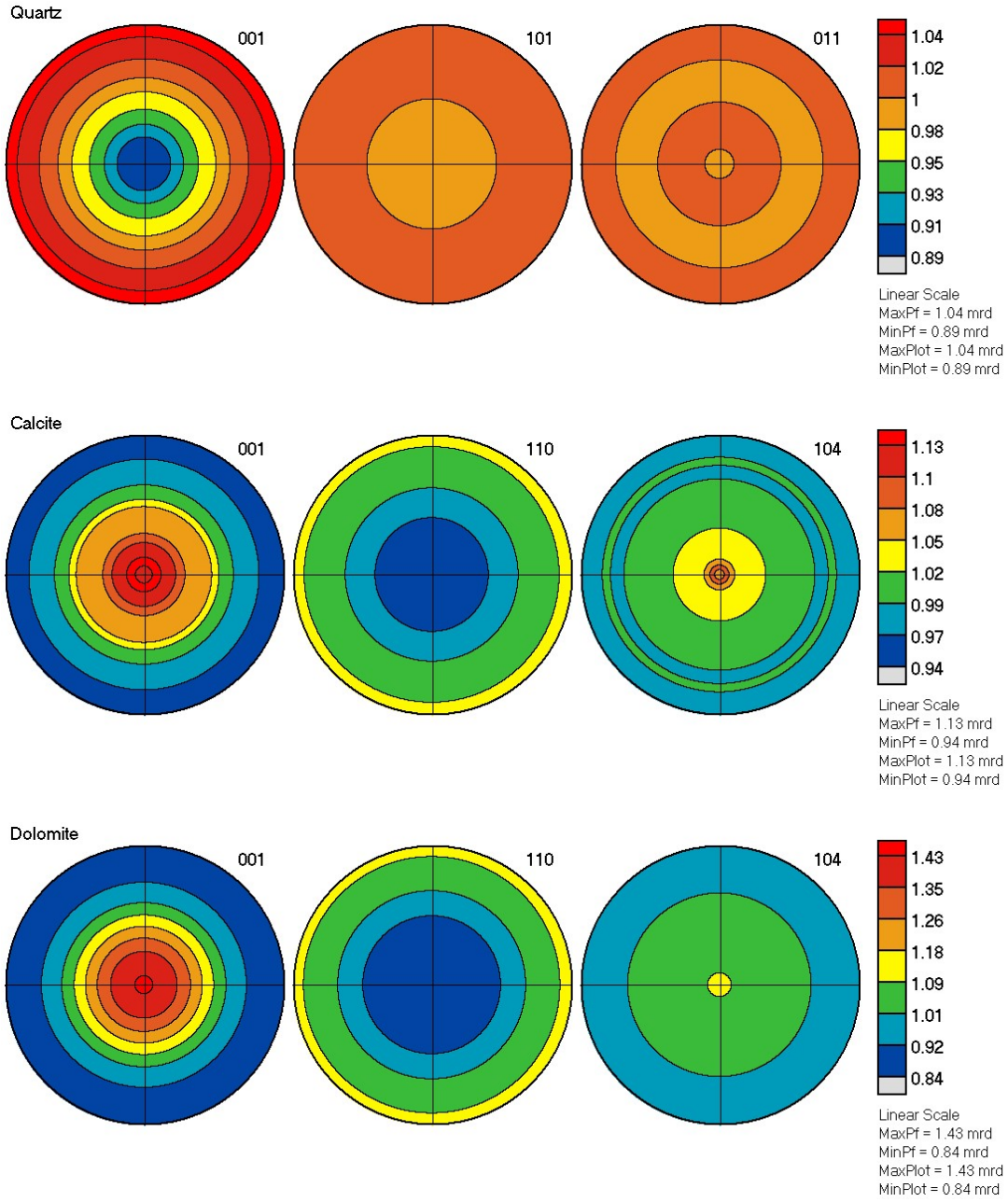

Figure 16. Pole figures for quartz, calcite, and dolomite from sample Q8_9715_light.

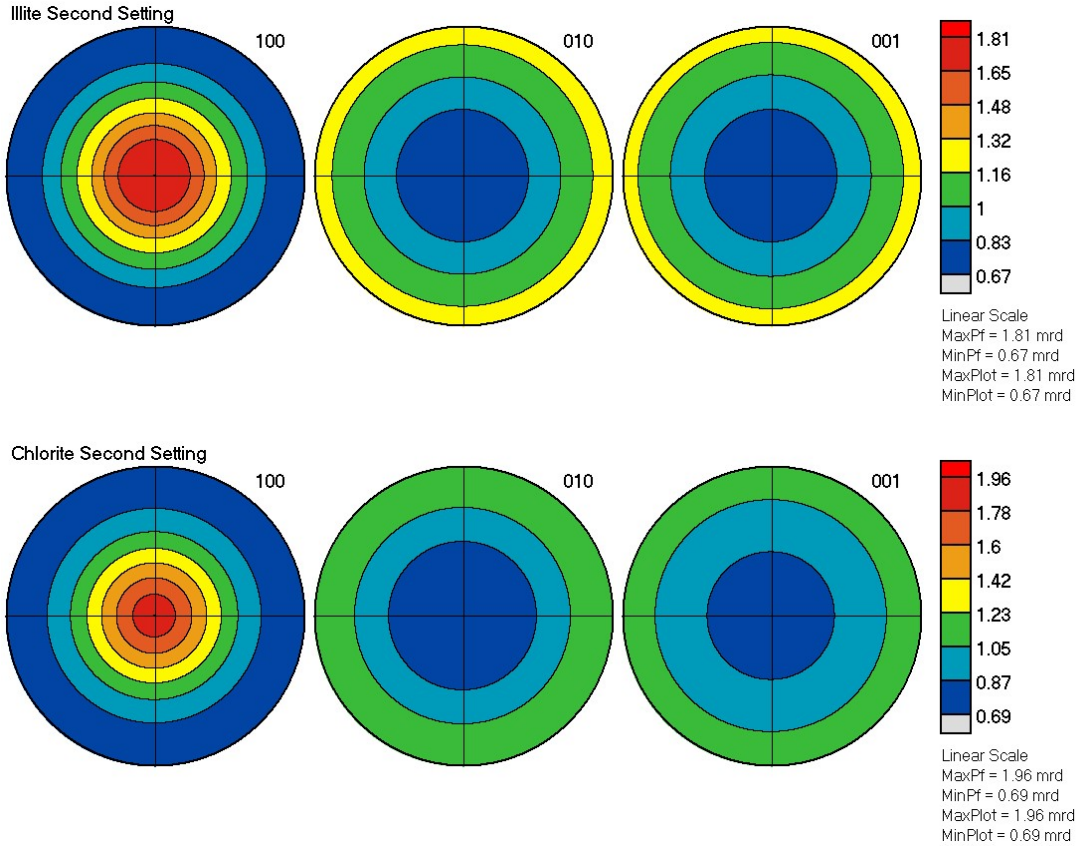

Figure 17. (001), (100), and (010) pole figures for clay phases illite and chlorite in sample Q8_9715_dark.

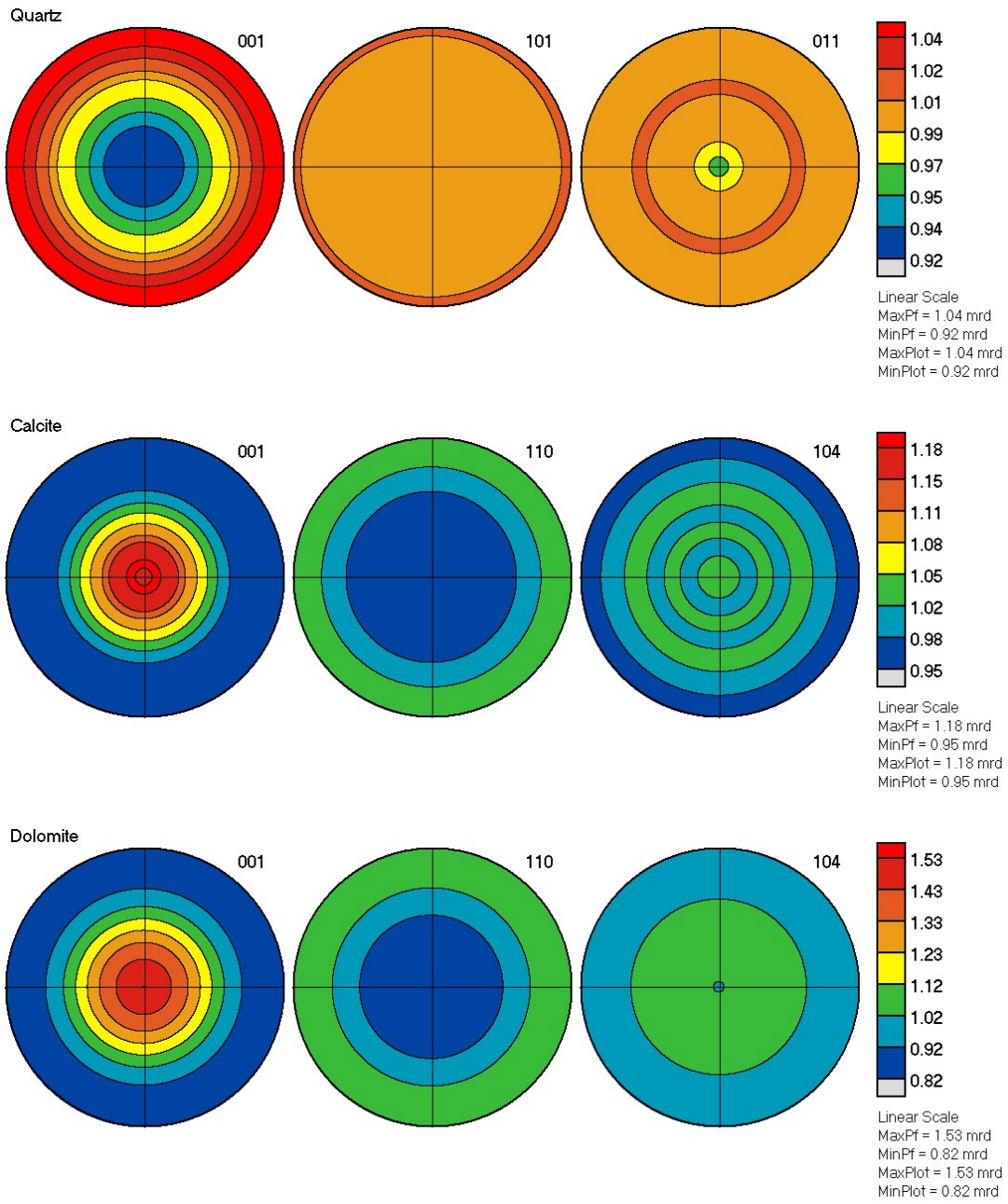

Figure 18. Pole figures for quartz, calcite, and dolomite from sample Q8_9715_dark.

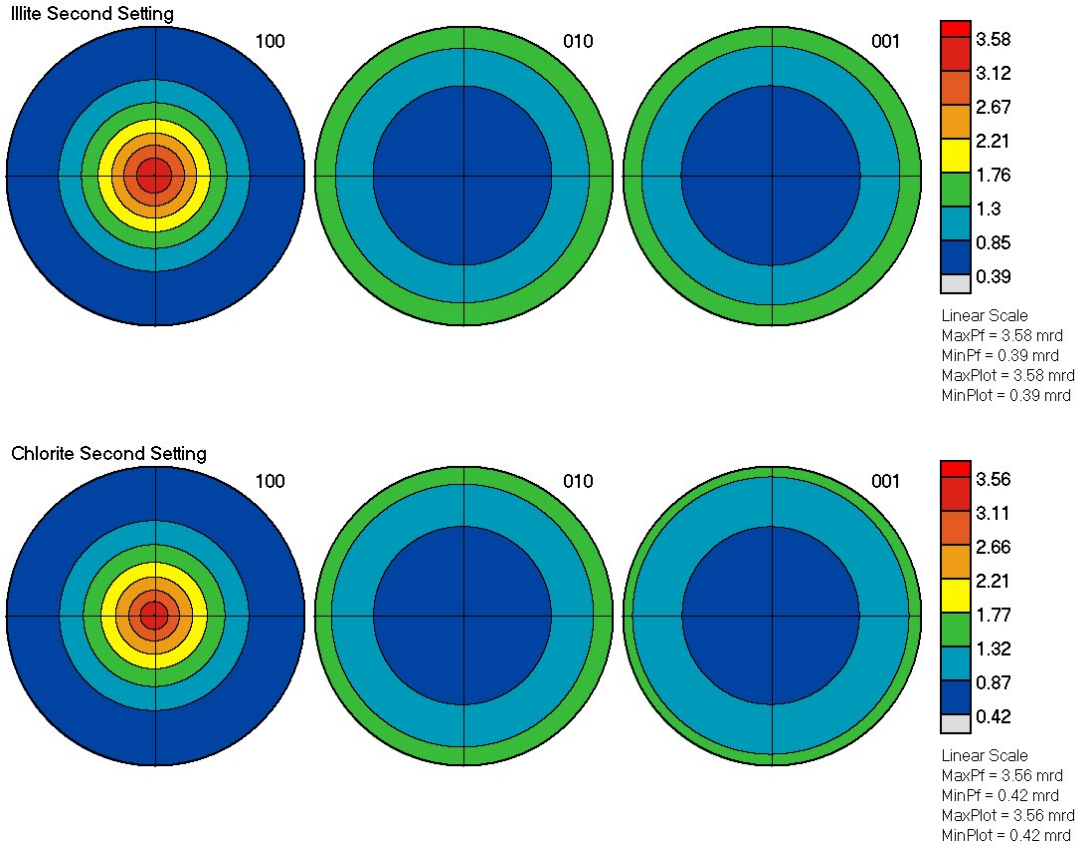

Figure 19. (001), (100), and (010) pole figures for clay phases illite and chlorite in sample Q8_9703.

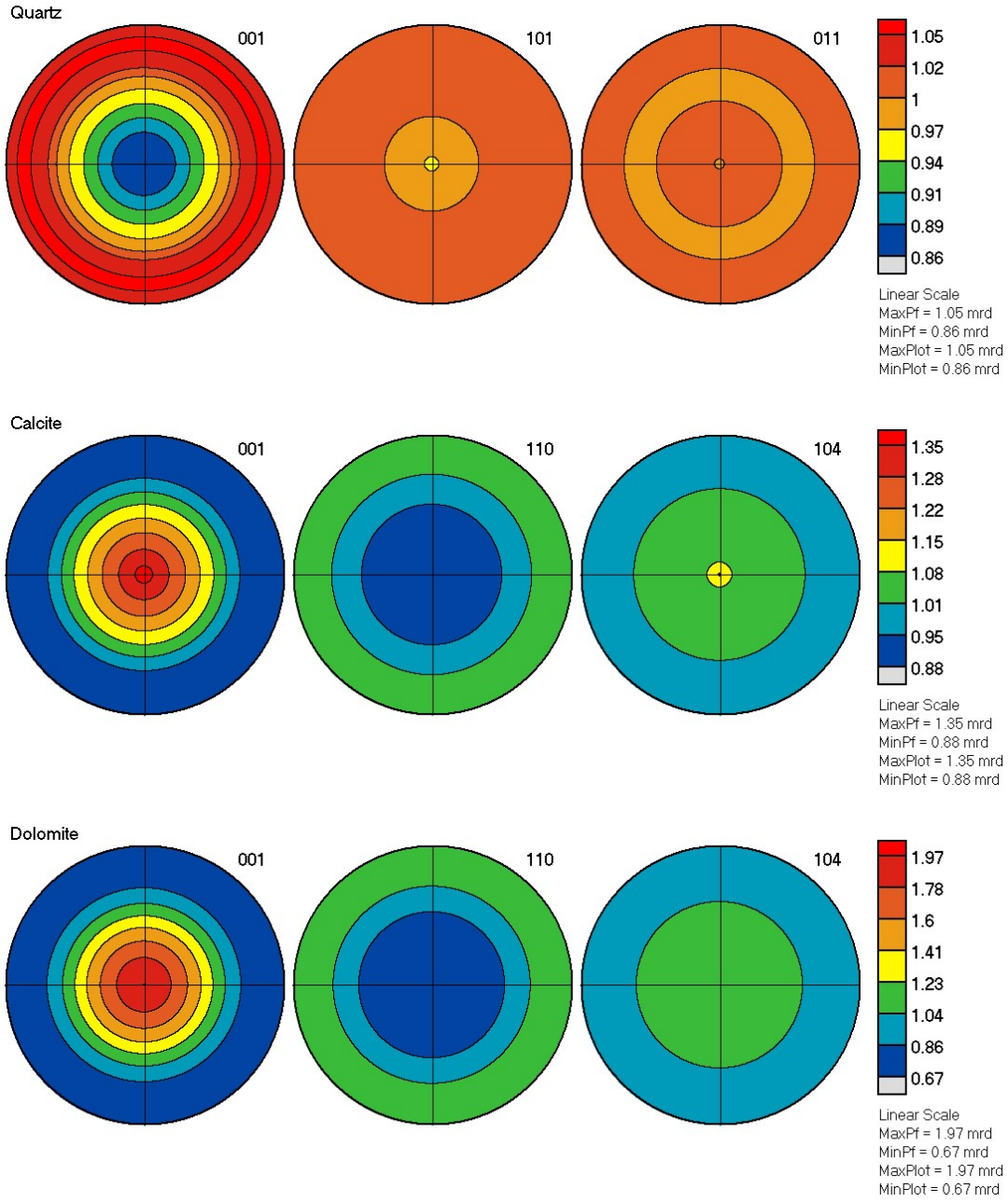

Figure 20. Pole figures for quartz, calcite, and dolomite from sample Q8_9703.

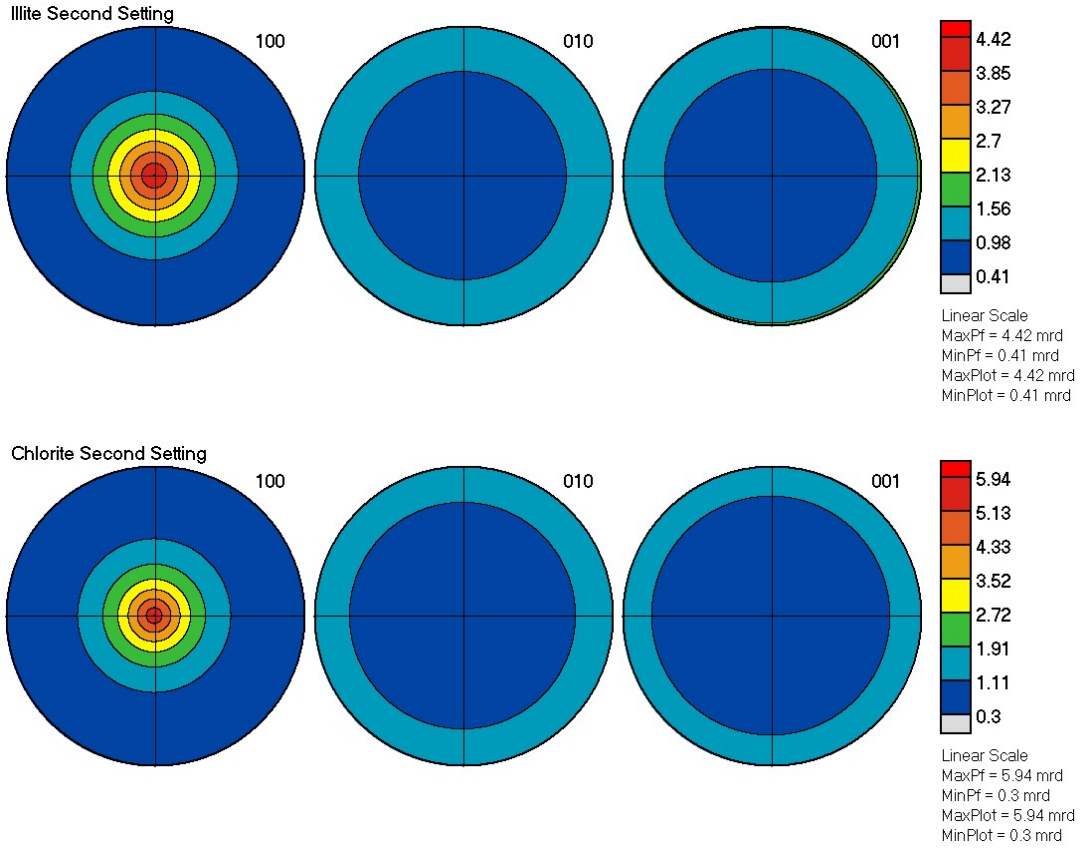

Figure 21. (001), (100), and (010) pole figures for clay phases illite and chlorite in sample P2_7135.

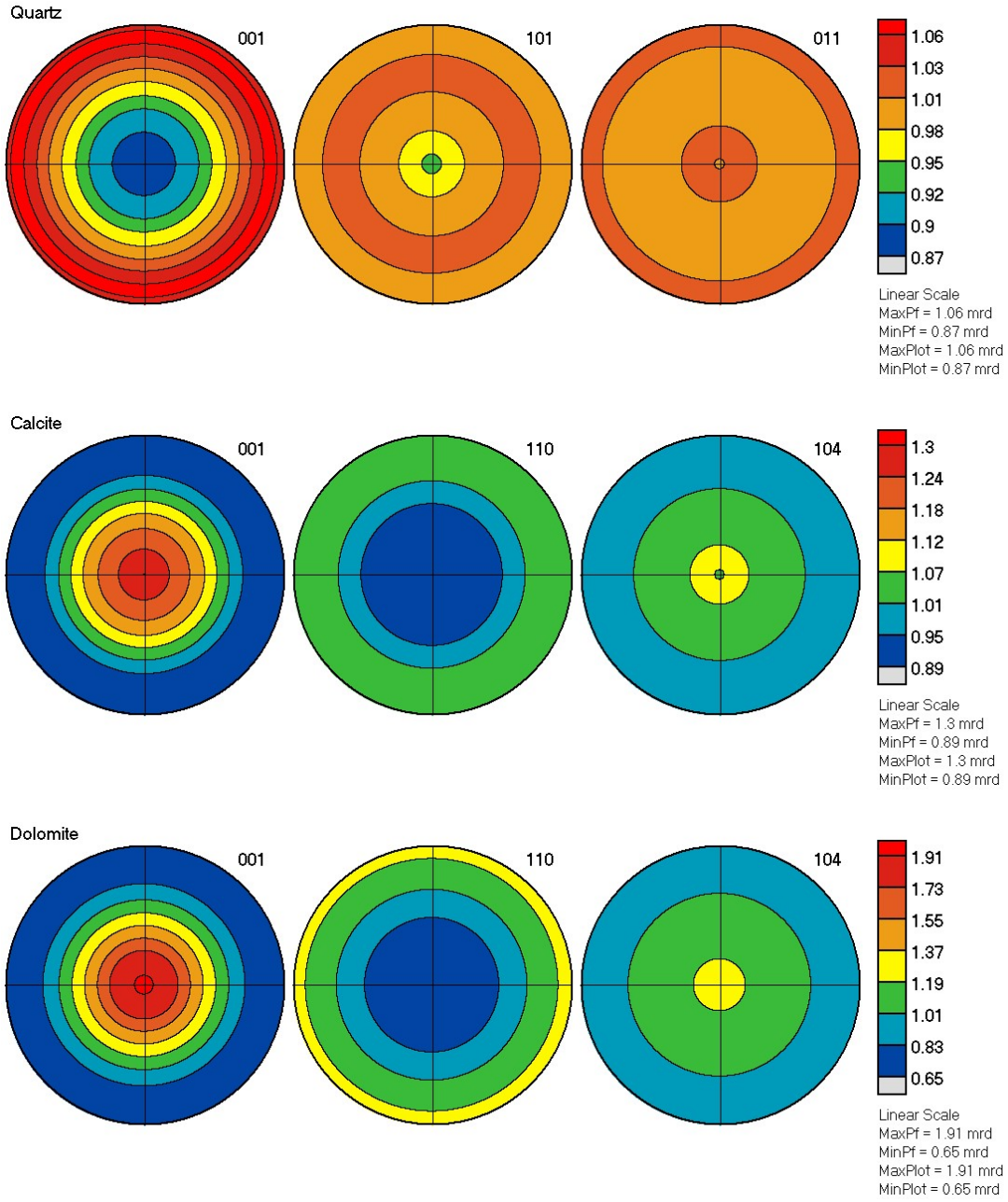

Figure 22. Pole figures for quartz, calcite, and dolomite from sample P2_7135.

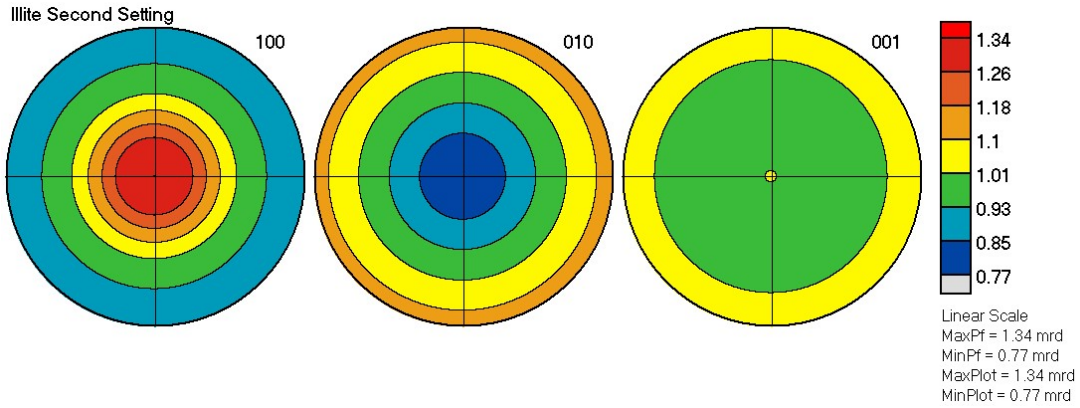

Figure 23. (001), (100), and (010) pole figures for clay phase illite in sample Ex1_091. No chlorite was found in Ex1_091.

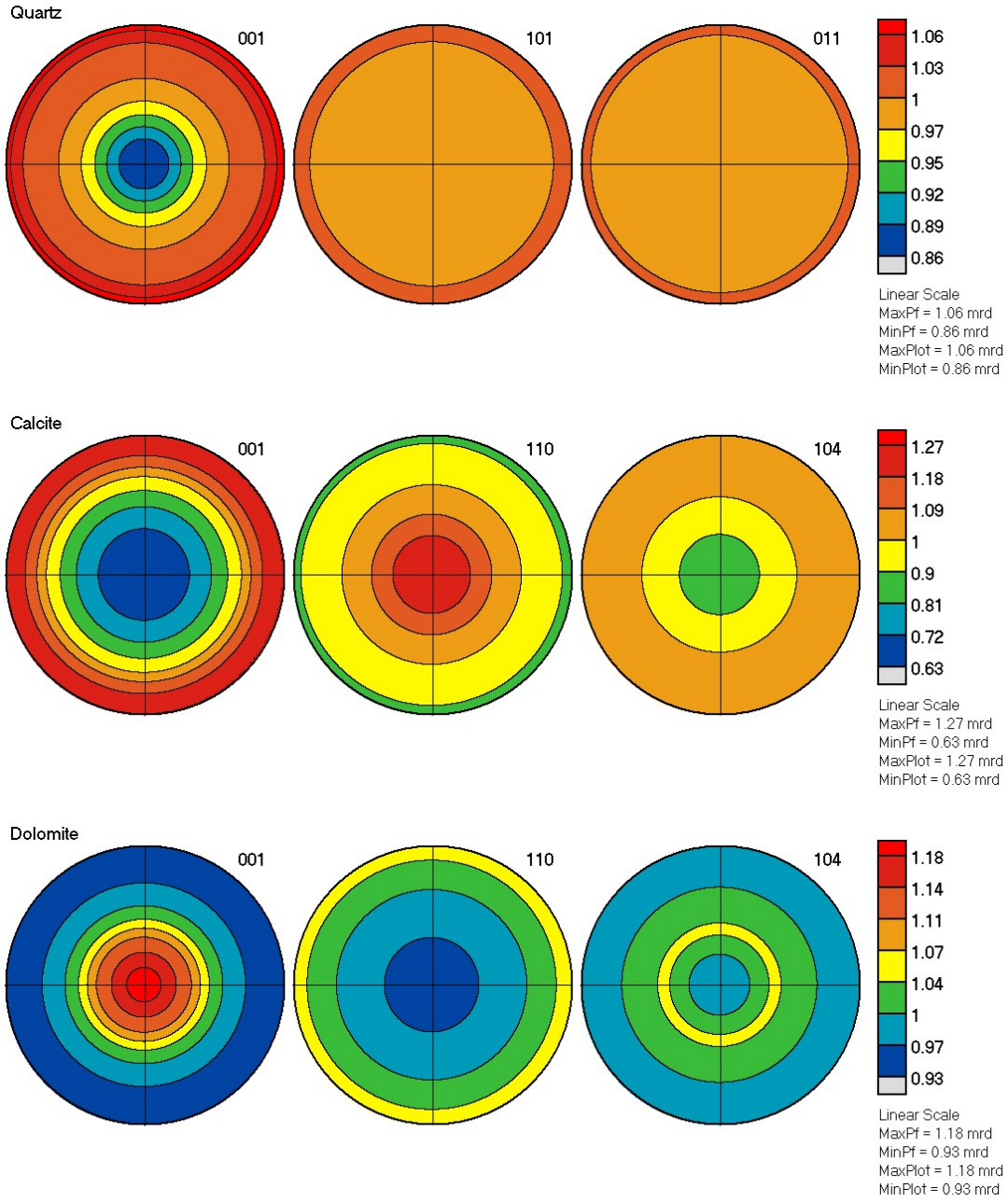

Figure 24. Pole figures for quartz, calcite, and dolomite from sample Ex1_091.

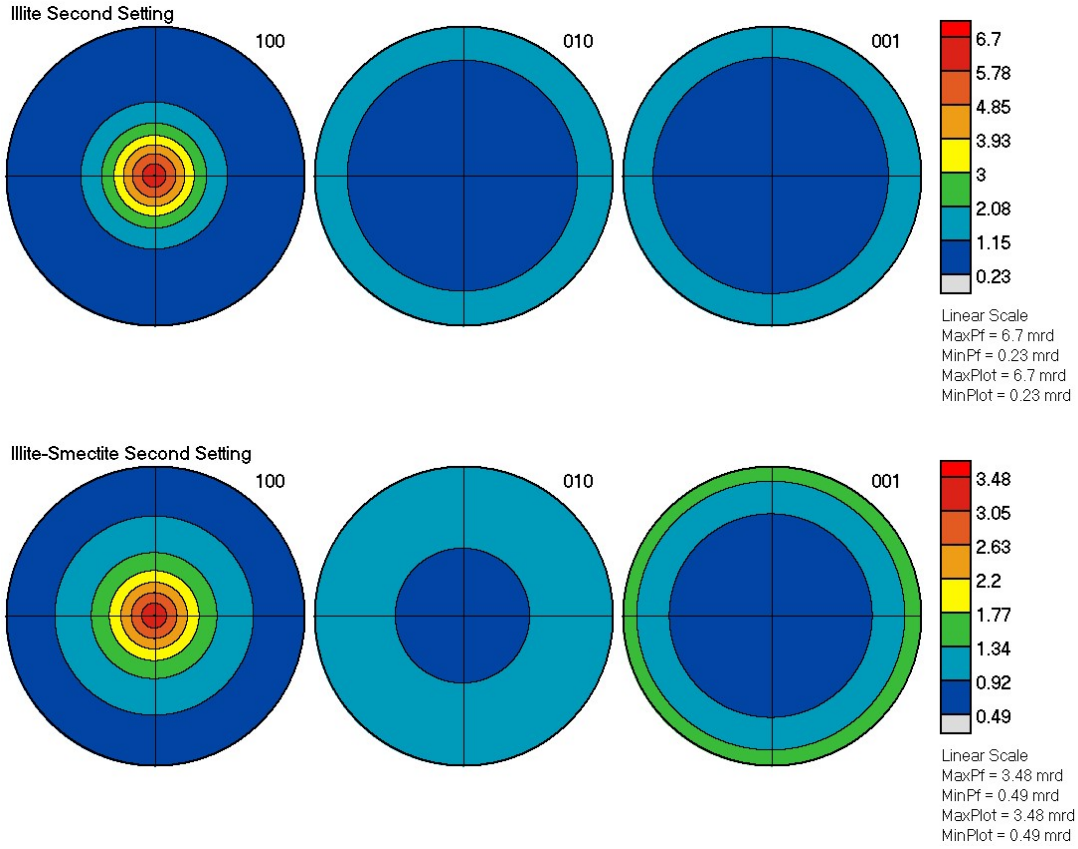

Figure 25. (001), (100), and (010) pole figures for clay phases illite and illite-smectite in sample Ex1_036. No chlorite was found in Ex1_036.

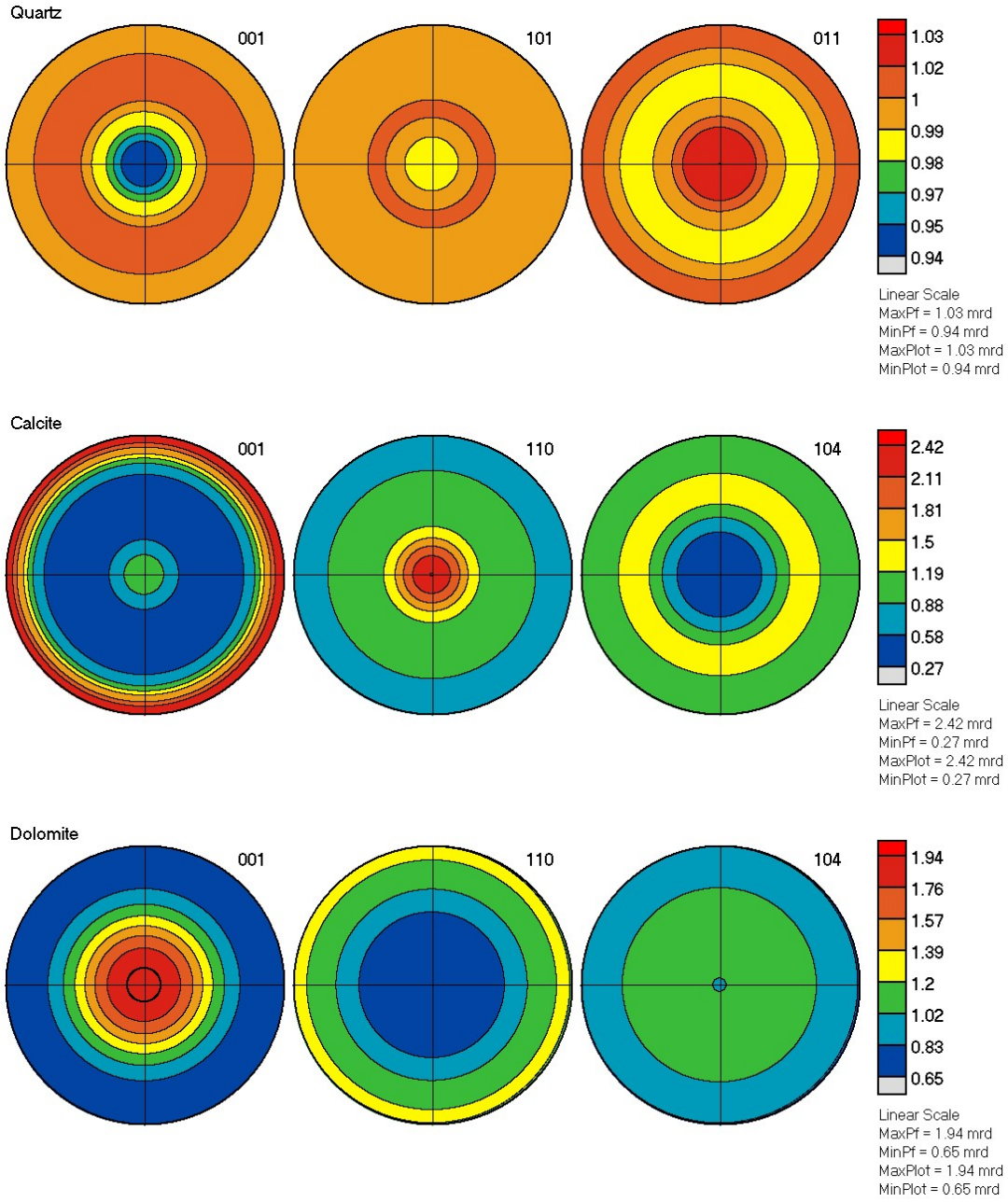

Figure 26. Pole figures for quartz, calcite, and dolomite from sample Ex1_036.

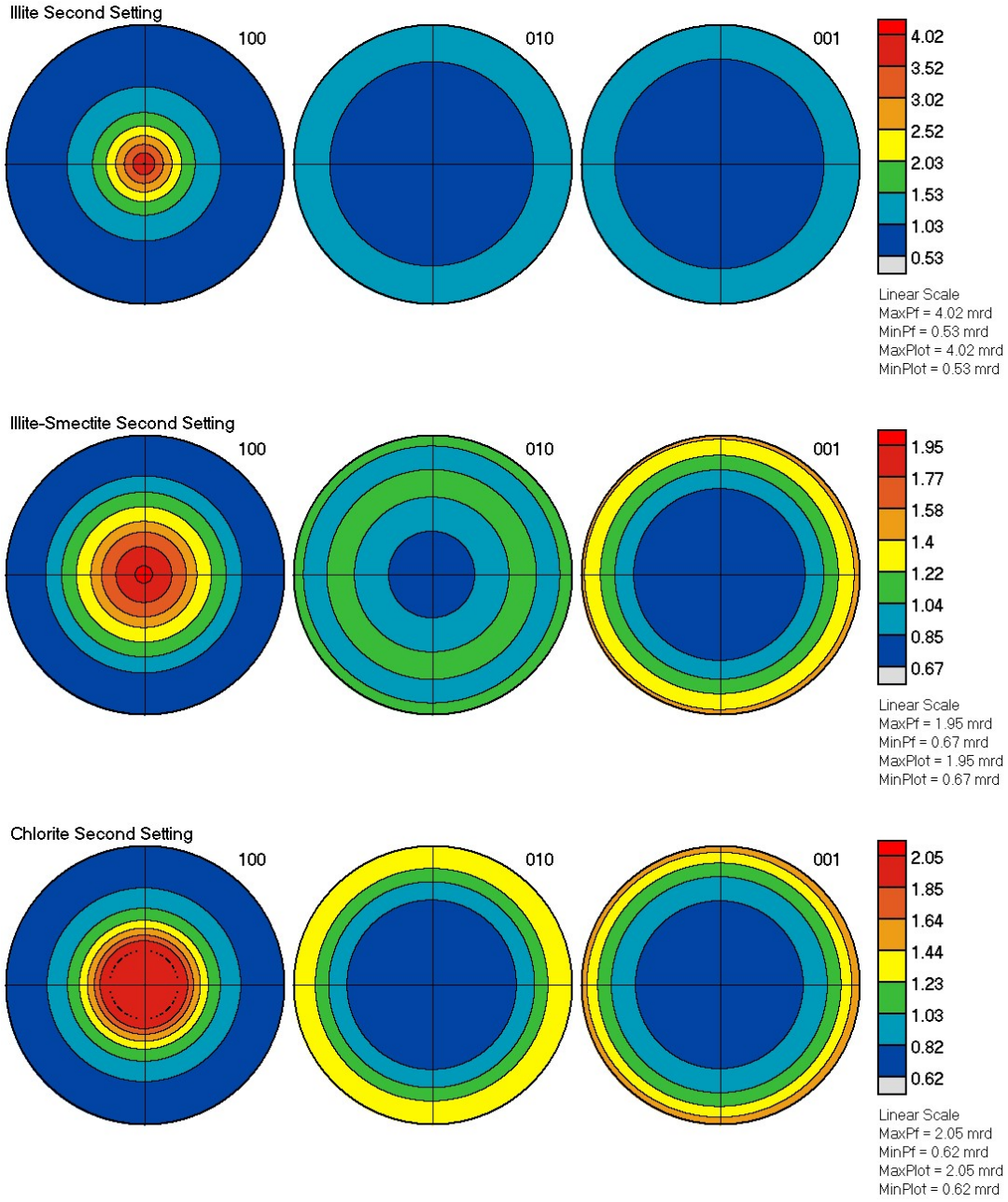

Figure 27. (001), (100), and (010) pole figures for clay phases illite, illite-smectite, and chlorite in sample Ex1_013.

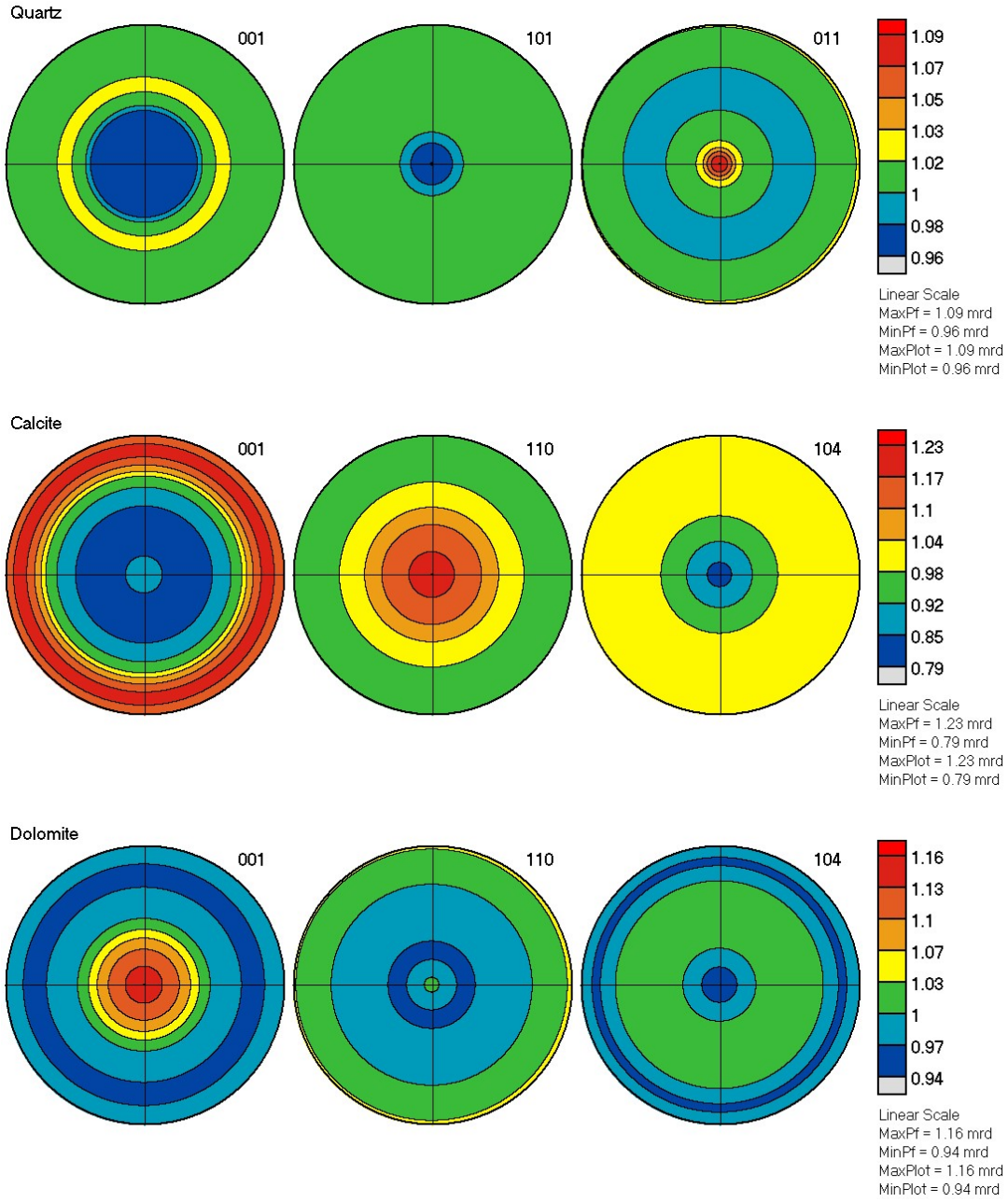

Figure 28. Pole figures for quartz, calcite, and dolomite from sample Ex1_013.

averaging the single crystal properties over the ODF of that particular mineral. The single crystal elastic tensor coefficients that were used for each mineral phase are reported in Table 1.

In order to determine the elastic properties for each shale sample, each mineral tensor was weighted by its volume fraction, and averaged using the Voigt, Reuss, Hill, and Geometric Mean. The Voigt approximation is an average of elastic constants (C_{ij}'s) and assumes an isostrain condition (Voigt, 1928). The Reuss approximation is an average elastic compliance (S_{ij}'s) and assumes an isostress condition (Reuss, 1929). These provide an upper and lower limit, respectively, for each calculation. The Hill averaging method is an arithmetic mean of the Voigt and Reuss averages (Hill, 1963). The Geometric Mean is a method that assumes the average elastic stiffness is equal to the inverse of the average elastic compliances, which is not true for the Voigt and Reuss averages (Matthies & Humbert, 1993). The Geometric Mean is typically very close to the Hill average. BEARTEX was used to calculate P- and S-wave velocities and polarizations, which uses Christoffel equations to solve for these.

Results

Rietveld refinement in MAUD allows for the quantitative extraction of constituent mineral phase proportions in a sample (Table 2). The samples range from a low to moderate amount of clay minerals, with illite being by far the dominant clay phase in every sample. Chlorite appears as a lesser clay phase in most samples and illite-smectite is present in EX1_013 and EX1_036. Clay volume percentages in the samples range from 11% to 35% in the Green River samples, and from 20% to 37% in the Mancos

Table 1: Single crystal stiffness tensor coefficients (C_{ij}'s) in GPa for the mineral phases used in this study. Coefficients for illite, illite-smectite, and chlorite were obtained from Militzer et al., 2011. Coefficients for quartz, calcite, dolomite, albite, and pyrite were obtained from Bass, 1995.

Phase	C_{11}	C_{12}	C_{13}	C_{22}	C_{23}	C_{33}	C_{44}	C_{55}	C_{66}
Illite	60.3	27.2	23.5	180.9	53.4	170	70.5	18.4	23.8
Illite-smectite	27.2	13.2	5.2	153.9	25.1	188.5	55.4	10.4	2.8
Chlorite	180.9	53.4	27.2	170	23.5	60.3	18.4	23.8	70.5
Quartz	87.3	6.6	12	87.3	12	105.8	57.2	57.2	40.4
Calcite	144	53.9	51.1	144	51.1	84	33.5	33.5	45
Dolomite	205	71	57.4	205	57.4	113	39.8	39.8	67
Albite	74	36.4	39.4	131	31	128	17.3	29.6	32
Pyrite	361	33.6	33.6	361	33.6	361	105.2	105.2	105.2

Table 2. Phase proportions obtained through the Rietveld refinement of the samples expressed in volume percentage. The small fraction of aluminum present in EX1_036 and P2_7135 is likely from the x-ray beam clipping the aluminum rod while the diffraction image was being collected.

Sample	Phase	Quartz	Albite	Pyrite	Analcime	Dolomite	Calcite	Chlorite	Illite	Illite-Smectite	Aluminum
	Vol.										
EX1_013	%	11.38	15.71	0.00	11.42	28.15	13.78	0.46	14.22	4.88	0.00
EX1_036		24.31	15.80	0.85	14.00	8.26	2.00	0.00	28.43	6.28	0.07
EX1_091		10.49	19.40	0.00	0.00	40.34	18.45	0.00	11.31	0.00	0.00
Q8_9703		40.79	7.35	0.49	0.00	13.25	4.42	6.97	26.74	0.00	0.00
Q8_9715_dark		48.22	8.07	0.27	0.00	13.92	5.00	6.37	18.15	0.00	0.00
Q8_9715_light		52.00	7.93	0.26	0.00	13.96	6.09	5.09	14.67	0.00	0.00
Q16_15172		33.21	7.11	0.87	0.00	12.72	13.61	4.72	28.19	0.00	0.00
Q16_15223		42.49	6.65	0.80	0.00	11.68	10.46	3.56	24.37	0.00	0.00
Q16_15264		42.19	6.75	1.23	0.00	11.17	10.14	4.53	24.05	0.00	0.00
Q16_15160		34.13	7.21	1.20	0.00	10.81	17.54	4.09	24.33	0.00	0.00
P2_7135		32.29	5.20	1.03	0.00	10.86	12.35	5.86	31.13	0.00	1.28

samples. The three samples taken from the Green River formation are comprised of a relatively small amount of quartz, ranging from 10% to 24%, compared to the Mancos samples, which range from 32% to 52%. Additionally, Green River samples EX1_013 and EX1_091 contain a larger carbonate (dolomite and calcite) fraction, 42% and 58% respectively, than EX1_036 (10%) and the Mancos samples, which range from 18% to 28% carbonates. All Green River samples contain a significantly higher feldspar fraction than Mancos samples, with volume fractions in the Green River ranging from 15% to 19%, and from 5% to 8% in the Mancos. Overall, samples from the Mancos tend to be more dominated by quartz, with moderate amounts of carbonate minerals. A small amount of aluminum is observed in diffraction from two samples, P2_7135 and EX1_036. This is due to the x-ray beam clipping the aluminum rod holding the sample during x-ray exposure.

In addition to phase proportions, unit cell parameters of the constituent phases were refined. The unit cell parameters for mineral phases used in this study are reported in Table 3. Monoclinic clay phases (illite, chlorite, and illite-smectite) were refined. Small variations are notably more common in Green River samples. Unrefined unit cell parameters of non-clay phases fit the data well to begin with, and so were fixed for all samples.

The main purpose of the Rietveld refinement for purposes of this study is to quantify crystallographic preferred orientations of mineral phases in each sample. The resulting pole figures are displayed in Figures 7 through 28. The pole figures are equal area projections of pole distributions for a given Miller index of a lattice plane, show in multiples of random distribution (m.r.d.), where an m.r.d. of 1 represents a random

Table 3. Unit cell parameters of the mineral phases used for sample refinements. Parameters for non-clay minerals were held constant, while those of clay phases were allowed to be refined. Clay phase unit cell parameters did vary slightly, with slightly larger variations seen in Green River samples. Monoclinic phase parameters (illite, chlorite, and illite-smectite) are reported in second setting.

Phase	Sample	a(Å)	b(Å)	c(Å)	α(°)	β(°)	γ(°)
Illite	Q16_15160	5.216	9.013	20.132	90	95.414	90
	Q16_15172	5.217	9.004	20.083	90	95.47	90
	Q16_15223	5.216	9.017	20.119	90	95.52	90
	Q16_15264	5.216	9.014	20.104	90	95.518	90
	Q8_9703	5.211	9.008	20.089	90	95.505	90
	Q8_9715_dark	5.215	9.014	20.115	90	95.413	90
	Q8_9715_light	5.225	9.012	20.144	90	95.313	90
	P2_7135	5.208	9.017	20.089	90	95.611	90
	EX1_013	5.239	9.026	20.102	90	94.376	90
	EX1_036	5.233	8.999	20.052	90	94.973	90
	EX1_091	5.238	9.021	20.112	90	94.964	90
Chlorite	Q16_15160	5.344	9.218	14.258	90	96.182	90
	Q16_15172	5.283	9.32	14.332	90	98.135	90
	Q16_15223	5.341	9.209	14.258	90	96.225	90
	Q16_15264	5.326	9.21	14.246	90	96.082	90
	Q8_9703	5.282	9.289	14.349	90	98.487	90
	Q8_9715_dark	5.282	9.27	14.349	90	98.67	90
	Q8_9715_light	5.248	9.164	14.401	90	98.738	90
	P2_7135	5.352	9.17	14.281	90	96.632	90
	EX1_013	5.303	9.236	14.359	90	98.863	90
	EX1_036	5.097	9.964	14.48	90	98.113	90
Ill.-Smec.	EX1_013	5.416	9.18	10.865	90	99.083	90
	EX1_036	5.466	9.199	10.791	90	99.219	90
Calcite		4.992	4.992	17.076	90	90	120
Dolomite		4.819	4.819	16.077	90	90	120
Quartz		4.937	4.937	5.433	90	90	120
Albite		8.154	12.802	7.158	94.129	116.606	87.809
Pyrite		5.442	5.442	5.442	90	90	90
Analcime		13.699	13.699	13.699	90	90	90

distribution. Pole figures are shown for illite and chlorite in second setting, where (001) is the basal cleavage plane. The relatively strong texture of 4.1 m.r.d. for illite and 4.7 m.r.d. for chlorite seen on the (001) pole figure (Figure 7) for these two phases indicates a strong preference for minerals to be stacked along this plane. The maximum m.r.d. for the (001) illite pole figures of the samples in this study ranges from 1.3 to 6.7. Both the high and low m.r.d. values are represented by Green River formation samples. Mancos Shale samples have maximum m.r.d. ranges from 1.4 to 4.4. Quartz and calcite display an almost completely random pole distribution, with dolomite displaying a weak texture on (001). These vary slightly with each sample, with calcite sometimes displaying a slightly stronger texture, or dolomite displaying a weaker one. Quartz, and the other minerals that are not shown, exhibit a near random texture in all samples.

Since a fiber (axial) symmetry for texture was imposed upon each constituent phase in MAUD, the resulting polyphase aggregate can be treated as having axial symmetry. This reduces the elastic tensor from 21 to 5 independent components, where $C_{11}=C_{22}$, $C_{12}=C_{11}-2C_{66}$, $C_{13}=C_{23}$, C_{33}, and $C_{44}=C_{55}$ are the independent components with all others being zero (Nye, 1956). The polyphase elastic tensors for each of the four averaging schemes (Voigt, Reuss, Hill, and Geometric) for each sample are reported in Table 4.

Table 5 shows the calculated P- and S-wave velocities for each averaging scheme, along with calculated anisotropy and total clay volume % for each sample. Anisotropy is expressed as a percentage and was calculated by Anisotropy = 200*(Vmax-Vmin)/(Vmax+Vmin). As can be seen in the table, the Voigt (iso-strain) average is the upper limit for calculated velocities and the Reuss (iso-stress) average is the lower limit. The Hill average, and the geometric mean calculation result in similar values. The

Table 4. Polycrystal elastic tensor coefficients (C_{ij}'s) for each sample in this study. Values were calculated for the Voigt, Reuss, and Hill averages and geometric mean for each sample, assuming axial symmetry. Values are given in GPa.

	Q16_15160				Q16_15172				Q16_15223			
	Voigt	Reuss	Hill	Geo.	Voigt	Reuss	Hill	Geo.	Voigt	Reuss	Hill	Geo
C_{11}	120.34	90.37	105.36	106.08	123.2	91.1	107.15	107.97	118.38	90.24	104.31	104.48
C_{13}	28.51	26.59	27.55	28.63	28.58	26.17	27.37	28.46	25.79	24.04	24.91	25.91
C_{33}	104.8	83.17	93.99	92.71	105.48	83.12	94.3	92.83	108.72	85.69	97.2	96.02
C_{44}	41.3	29.46	35.4	34.44	42.15	29.83	35.99	34.95	43.62	31.72	37.67	36.81
C_{66}	45.18	31.48	38.33	38.02	46.5	32.01	39.25	38.97	45.91	32.89	39.4	38.91
	Q16_15264				Q8_9703				P2-7135			
	Voigt	Reuss	Hill	Geo.	Voigt	Reuss	Hill	Geo.	Voigt	Reuss	Hill	Geo
C_{11}	119.41	91.17	105.29	105.57	120.56	89.55	105.06	105.7	123.67	92.4	108.04	108.77
C_{13}	25.82	24.03	24.92	25.92	25.32	22.95	24.14	25.15	28.12	26.01	27.06	28.11
C_{33}	108.89	86.23	97.56	96.39	104.45	82.09	93.27	91.83	107.17	84.9	96.03	94.61
C_{44}	43.85	32.05	37.95	37.09	42.99	30.89	36.94	35.96	42.86	30.67	36.76	35.76
C_{66}	46.37	33.34	39.85	39.41	46.91	32.89	39.9	39.58	46.99	32.74	39.87	39.56
	Q8_9715_dark				Q8_9715_light				EX1_013			
	Voigt	Reuss	Hill	Geo.	Voigt	Reuss	Hill	Geo.	Voigt	Reuss	Hill	Geo
C_{11}	116.82	91.82	104.316	104.44	115.81	93.32	104.57	104.57	150.91	123.01	136.96	137.49
C_{13}	24.83	23.54	24.18	25.14	24.34	23.74	24.04	24.93	43.32	41.48	42.4	43.65
C_{33}	110.52	88.57	99.55	98.82	111.95	91.12	101.54	101.04	144.39	120.59	132.49	132.03
C_{44}	44.3	33.2	38.75	38.07	44.75	34.21	39.48	38.89	51.78	39.85	45.82	45.09
C_{66}	45.76	33.97	39.86	39.4	45.61	34.69	40.15	39.68	53.38	40.56	46.97	46.54
	EX1_036				EX1_091							
	Voigt	Reuss	Hill	Geo.	Voigt	Reuss	Hill	Geo.				
C_{11}	147.86	114.22	131.04	132.26	133.67	108.01	120.84	121.38				
C_{13}	29.96	27.2	28.58	29.48	46.78	45.25	46.02	47.48				
C_{33}	126.67	106.18	116.42	114.76	132.46	107.52	119.99	120.32				
C_{44}	52.23	40.36	46.29	45.16	43.06	31.17	37.12	36.59				
C_{66}	57.73	42.91	50.32	50.26	43.35	31.36	37.35	36.88				

Table 5. P- and S-wave velocities calculated using the four averaging methods for each sample, along with calculate P and S anisotropy. Total clay volume percent and Thomsen parameters ε, γ, and δ are also shown.

Sample	Clay (vol%)	Averaging Model	V_s min(km/s)	V_p min(km/s)	V_p max(km/s)	P-Ani. (%)	ε	γ	δ
Q16_15160	28.42	Voigt	3.98	6.34	6.79	6.85	0.074	0.047	0.063
		Reuss	3.36	5.65	5.89	4.16	0.043	0.034	0.029
		Hill	3.68	6.01	6.36	5.66	0.060	0.041	0.048
		Geometric	3.63	5.97	6.38	6.64	0.072	0.052	0.054
Q16_15172	32.92	Voigt	4.02	6.36	6.88	7.85	0.084	0.052	0.074
		Reuss	3.38	5.65	5.91	4.50	0.048	0.037	0.033
		Hill	3.72	6.02	6.41	6.28	0.068	0.045	0.056
		Geometric	3.66	5.97	6.44	7.57	0.082	0.058	0.062
Q16_15223	27.93	Voigt	4.09	6.46	6.74	4.24	0.044	0.026	0.041
		Reuss	3.49	5.74	5.89	2.58	0.027	0.018	0.021
		Hill	3.8	6.11	6.33	3.54	0.037	0.023	0.032
		Geometric	3.76	6.07	6.33	4.19	0.044	0.029	0.038
Q16_15264	28.58	Voigt	4.1	6.47	6.77	4.53	0.048	0.029	0.044
		Reuss	3.51	5.75	5.92	2.91	0.029	0.020	0.022
		Hill	3.82	6.12	6.36	3.85	0.040	0.025	0.034
		Geometric	3.77	6.08	6.37	4.66	0.048	0.052	0.040
Q8_9703	33.71	Voigt	4.06	6.33	6.8	7.16	0.077	0.046	0.069
		Reuss	3.44	5.61	5.86	4.36	0.045	0.032	0.033
		Hill	3.76	5.98	6.35	6.00	0.063	0.040	0.053
		Geometric	3.71	5.94	6.37	6.99	0.076	0.050	0.060
P2-7135	36.99	Voigt	4.05	6.42	6.89	7.06	0.077	0.048	0.065
		Reuss	3.43	5.71	5.96	4.28	0.044	0.034	0.030
		Hill	3.76	6.07	6.44	5.92	0.063	0.042	0.049
		Geometric	3.7	6.03	6.46	6.89	0.075	0.053	0.055
Q8_9715_dark	24.52	Voigt	4.12	6.51	6.7	2.88	0.029	0.016	0.027
		Reuss	3.57	5.83	5.94	1.87	0.018	0.012	0.016
		Hill	3.86	6.18	6.33	2.40	0.024	0.014	0.022
		Geometric	3.82	6.16	6.33	2.72	0.028	0.017	0.025
Q8_9715_light	19.76	Voigt	4.14	6.56	6.67	1.66	0.017	0.010	0.017
		Reuss	3.62	5.92	5.99	1.18	0.012	0.007	0.012
		Hill	3.89	6.24	6.34	1.59	0.015	0.008	0.015
		Geometric	3.86	6.23	6.34	1.75	0.017	0.010	0.017
EX1_013	19.56	Voigt	4.46	7.45	7.61	2.12	0.023	0.015	0.017
		Reuss	3.91	6.81	6.87	0.88	0.010	0.009	0.005
		Hill	4.19	7.31	7.52	2.83	0.017	0.013	0.012
		Geometric	4.16	7.12	7.27	2.08	0.021	0.016	0.014
EX1-036	34.71	Voigt	4.48	6.97	7.54	7.86	0.084	0.053	0.064
		Reuss	3.94	6.39	6.62	3.54	0.038	0.032	0.017
		Hill	4.21	6.69	7.09	5.81	0.063	0.044	0.042
		Geometric	4.16	6.64	7.13	7.12	0.076	0.056	0.046
EX1-091	11.31	Voigt	4.06	7.13	7.17	0.56	0.005	0.003	0.003
		Reuss	3.46	6.43	6.44	0.16	0.002	0.003	0.001
		Hill	3.77	6.79	6.81	0.29	0.004	0.003	0.002
		Geometric	3.75	6.8	6.83	0.44	0.004	0.004	0.003

geometric mean is the most physically satisfying of these averages as it achieves stress and strain compatibility. As such, it will be the primary average to be discussed. In the samples studied, P-anisotropy ranges from 0.4% in EX1_091 to 7.6% in Q16_15172. As clay minerals display the strongest texture and are the most anisotropic, they contribute the most to the bulk anisotropy of a sample. Carbonate minerals also display a weak texture in some samples, and are secondary contributors to sample anisotropy. Quartz, pyrite, and albite have a negligible effect. It is important to keep in mind that anisotropy values calculated here are only calculated based on the mineralogy and texture of each sample, and thus only account for intrinsic anisotropy. Factors such as porosity, fractures, and any fluids present are not accounted for in this calculation.

Table 5 also contains calculated Thomsen's parameters. Thomsen's parameters are a way to represent the anisotropic properties of a material that has an assumed axial symmetry about the bedding plane (Thomsen, 1986). These parameters are calculated using the previously determined C_{ij}'s of the bulk sample and are defined as follows.

$\varepsilon = (C_{11}-C_{33})/(2*C_{33})$

$\gamma = (C_{66}-C_{44})/(2*C_{44})$

$\delta = ((C_{13}+C_{44})^2-(C_{33}-C_{44})^2)/(2*C_{33}*(C_{33}-C_{44}))$

The ε parameter is a measure of P-wave anisotropy, while the γ parameter is a measure of S-wave anisotropy. The δ parameter is related to vertical P-wave velocities. The Thomsen parameters calculated for Green River samples in this study are ε = 0.002-0.076, γ = 0.003-0.056, and δ = 0.002-0.046. In the Mancos, they are ε = 0.017-0.082, γ = 0.01-0.058, and δ = 0.015-0.062.

Figures 29, 30, and 31 show plots of clay, silt, and carbonate volume fractions and P-

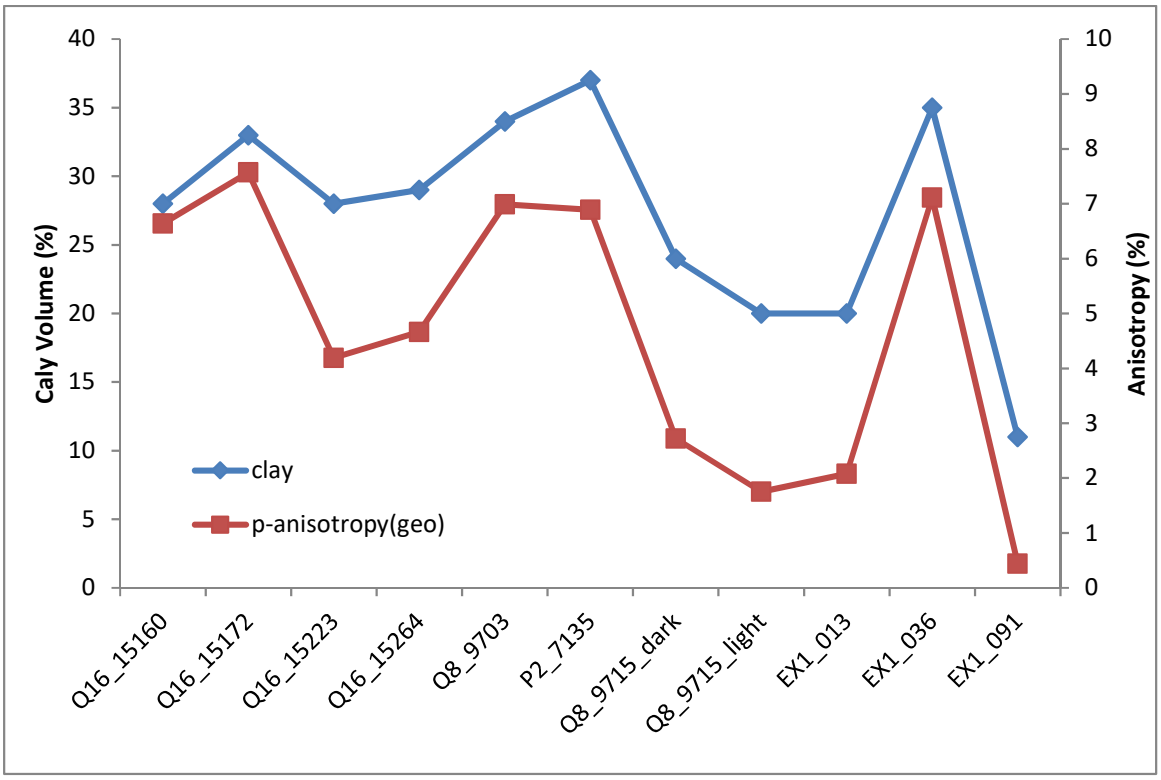

Figure 29. Plots of P-anisotropy (calculated from the geometric mean) and clay volume percentage for each sample. As can be seen, there is a strong correlation between the two, making the clay percent a good indicator of anisotropy.

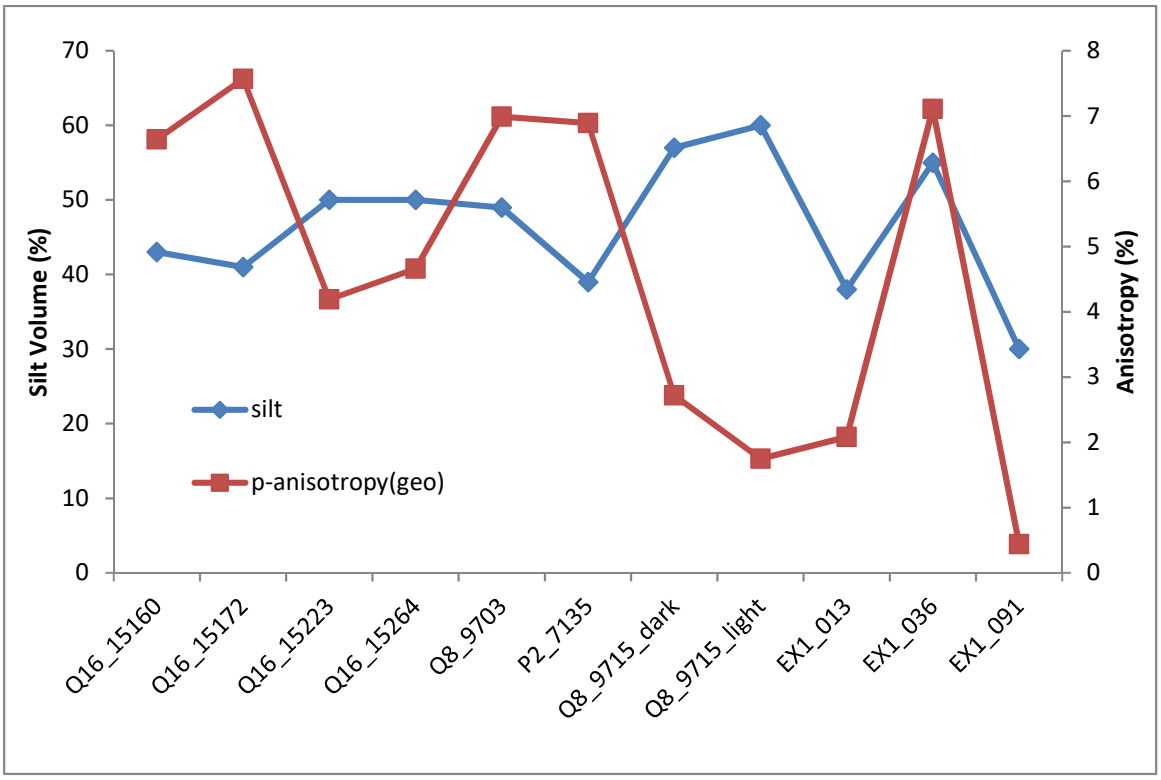

Figure 30. Plots silt volume percentage and P-anisotropy (calculated from the geometric mean) for the samples. As quartz and feldspars have little texture, they have little control over bulk anisotropy.

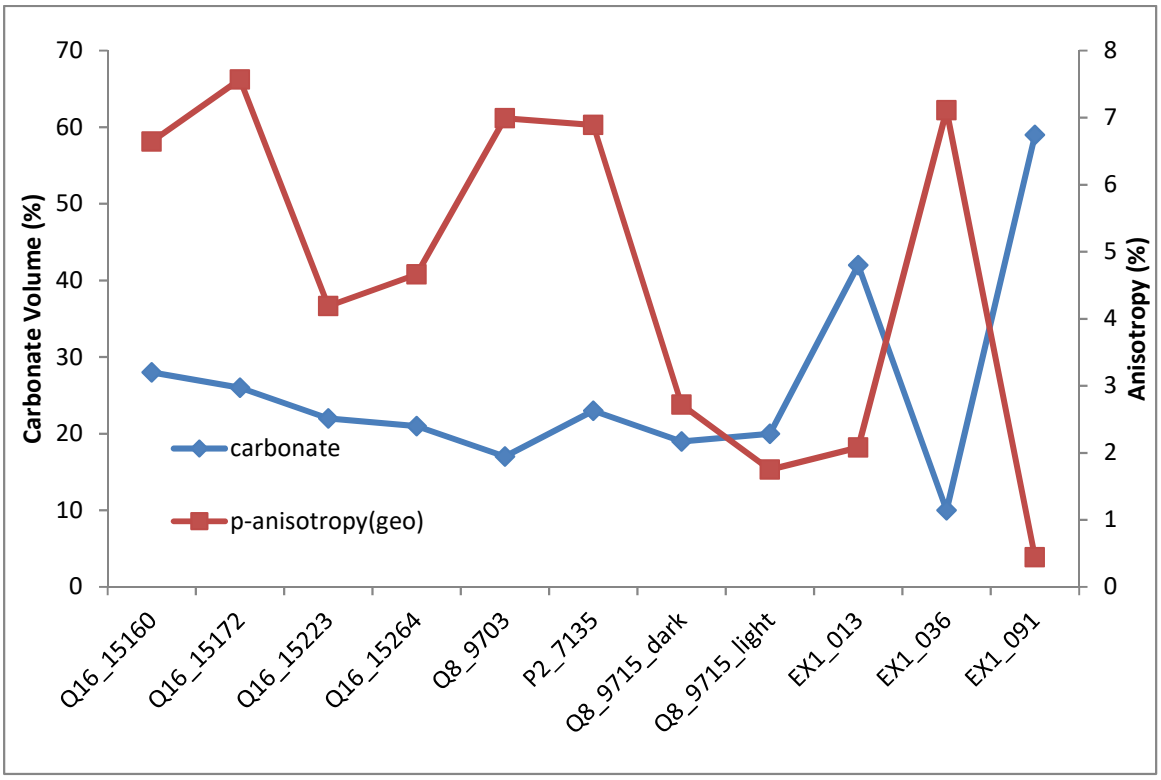

Figure 31. Plots of carbonate volume percentage and P-anisotropy (calculated from the geometric mean) for studied samples. Similar to silt, the carbonate fraction appears to have little control over the bulk anisotropy.

anisotropy for each sample. There is a clear correlation between the clay volume fraction and the anisotropy calculated for each sample. A higher clay fraction correlates to greater anisotropy. No such correlation exists between silt or carbonate fraction and anisotropy. Additionally, Figure 32 shows that there is a strong correlation between the amount of clay in a sample, and the texture strength of the clay minerals. A larger clay volume fraction correlates to stronger textures in the clay phases. Since the depth from which the Mancos Shale samples were obtained is known, this is plotted next to P-anisotropy in Figure 33**.** Sample depth may have a weak correlation to P-anisotropy, with deeper samples displaying higher anisotropy. However, this correlation is much less significant compared to the correlation between clay volume and anisotropy.

Discussion

The m.r.d. ranges for illite can be compared to similar previous studies of various shale formations around the world. The Kimmeridge Shale in the North Sea ranges from 2-6 m.r.d (Wenk, Kanitpanyacharoen, & Voltolini, 2010), and the Qusaiba Shale in Saudi Arabia ranges from 2.4 to 6.8 m.r.d. (Kanitpanyacharoen et al., 2011). Similarly, Central European shales have clay m.r.d. ranges from 2-9 m.r.d. (Wenk et al., 2008a, 2008b.), shales from Nigeria have a range from 2-5 m.r.d. (Lonardelli et al., 2007), shales from the Bakken formation, Montana have a range from 2-10 m.r.d. (Easley, 2014), and shales from Silver Hill, Montana have a maximum clay m.r.d. of around 10 (Wenk, Franz, Nihei, & Nakagawa, 2007). The samples from the Green River and Mancos Shale studied here do exhibit similar maximum clay texture strength (1.3-6.7 m.r.d.) to these other shales; however, they are at the lower end of the spectrum. This is due to the samples in this

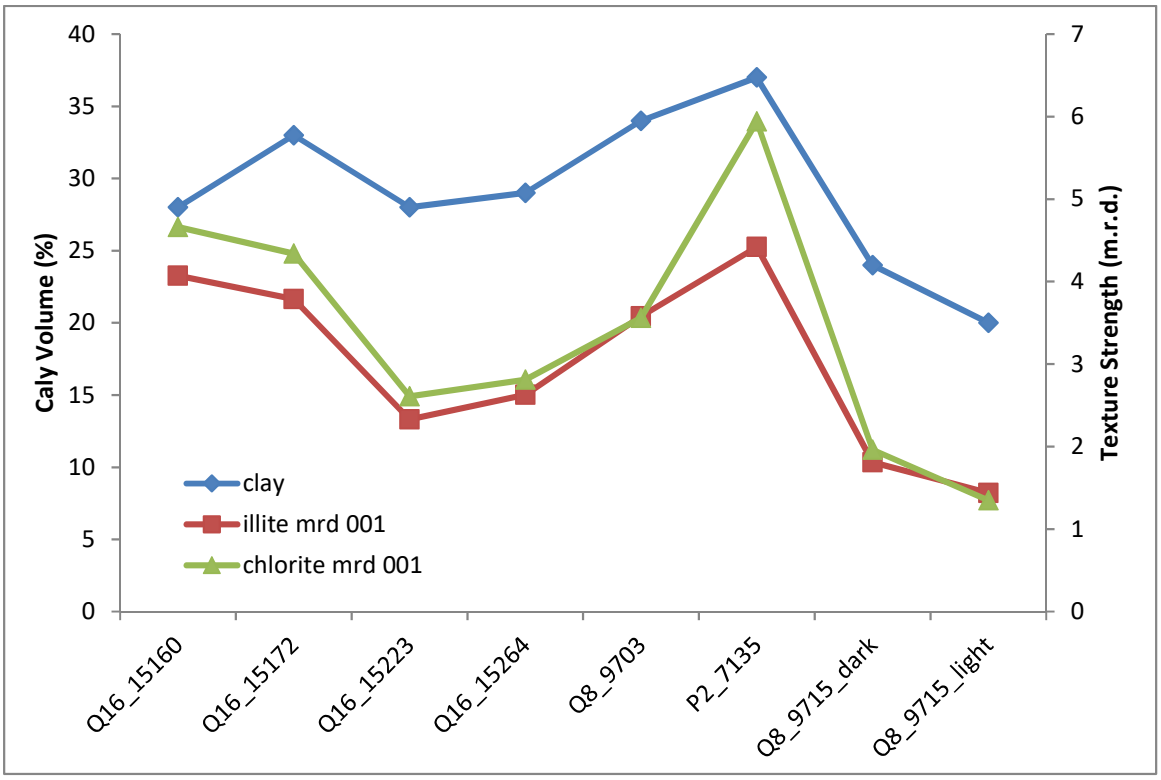

Figure 32. Plots of clay volume fraction and maximum m.r.d. for the (001) pole figures for illite and chlorite. A strong correlation can be seen between the amount of clay in a sample, and the texture strength. Note EX1 samples are not shown as they contain very little or no chlorite.

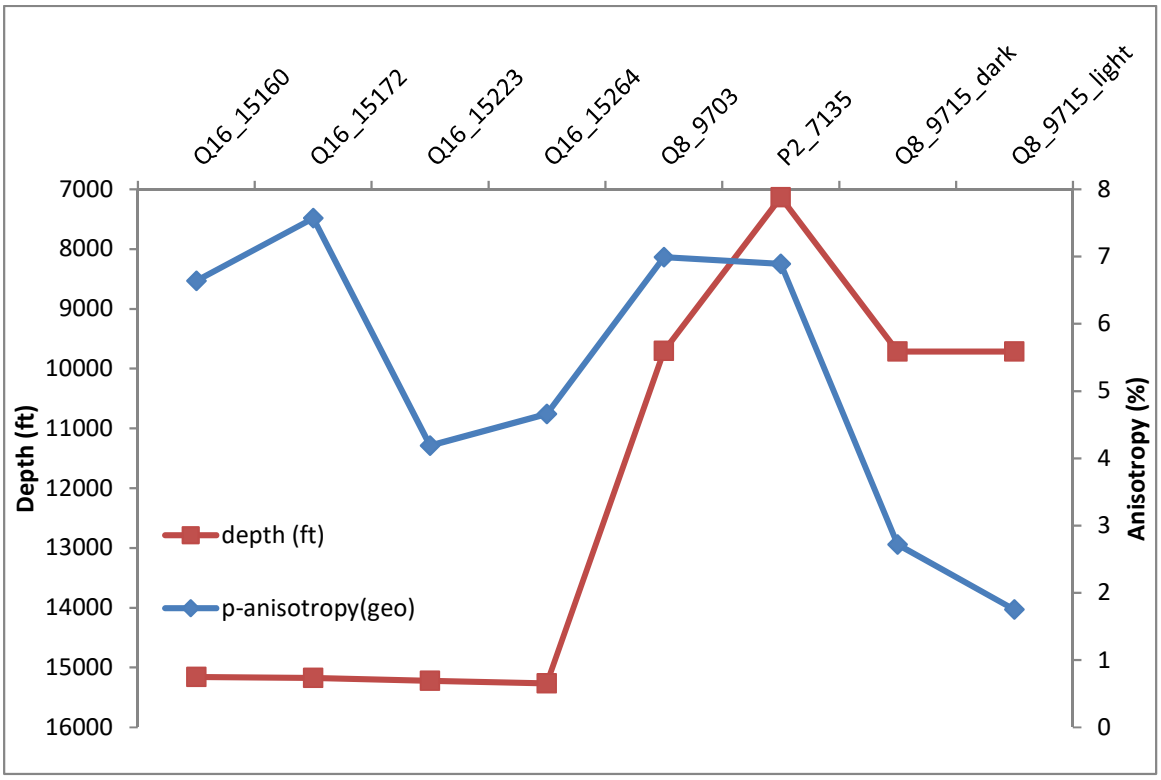

Figure 33. Plots sample depth and P-anisotropy (calculated from the geometric mean) for Mancos Shale samples. There may be a weak correlation between sample depth and anisotropy in some cases, but it is much smaller than the correlation between anisotropy and clay content. EX1 samples are not shown, as no depth data are available for them.

study having relatively low clay fractions (11-35% in the Green River and 20-37% in the Mancos) compared to other studies.

The P-wave anisotropies calculated using the geometric mean in this study range from 0.4% to 7.1% in the Green River samples, and from 1.7% to 7.6% in the Mancos samples. Again, clay volume fraction is strongly associated with a higher anisotropy. This is consistent with anisotropies calculated in other studies, though lower. The Mont Terri Shale anisotropy was calculated to be about 20% (Wenk et al. 2008a), the Qusaiba Shale were found to have a range from 9.1 to 14.3% (Kanitpanyacharoen et al., 2011), North Sea shales were calculated to have an anisotropy of about 12% (Valcke, 2006), and Nigerian shales have an anisotropy calculated at about 10% (Lonardelli et al., 2007) Bakken Shale samples have calculated anisotropy range of 1.4% to 16.5% (Easley, 2014) which is the most similar to the range seen in this study. The small amount of clay in the Green River and Mancos Shale samples is most likely the largest factor in the lower anisotropy (Hornby, 1994).

It should be noted that the kaolinite clay phase was observed in many of the shales studied around the world (Kanitpanyacharoen et al., 2011; Lonardelli et al., 2007; Wenk et al., 2008a, 2008b) and in many cases comprises a significant portion of the clay present in these shales. However, kaolinite is not present in the Green River or Mancos samples in this study. Kaolinite is also not observed in shale samples from the Bakken formation (Easley, 2014), where it is suggested that this may indicate a farther distance from the sediment source. This is consistent with the depositional environment of the Mancos samples (Horton, 2012); however, it is unclear if this is the case for the Green River samples.

The Thomsen parameters calculated for Green River samples in this study are ε = 0.002-0.076, γ = 0.003-0.056, and δ = 0.002-0.046. In the Mancos, they are ε = 0.017-0.082, γ = 0.01-0.058, and δ = 0.015-0.062. These compare to ε = 0.08-0.33, γ = 0.11-0.53, and δ = -0.05-0.23 in shale samples from the North Sea, Africa, and the Gulf Coast (Wang, 2002), ε = 0.10-0.16, γ = 0.07-0.12, and δ = 0.08-0.10 in the Qusaiba Shale in Saudi Arabia (Kanitpanyacharoen et al., 2011), and ε = 0.03-0.07, γ = 0.01-0.10, and δ = -0.03-0.03 in Nigerian shales (Lonardelli et al., 2007). The Thomsen parameters again show that the Green River and Mancos Shale samples studied not only have a lower degree of P-wave anisotropy, but also lower S-wave anisotropy than all of the samples in these other studies.

Texture strength can be used to estimate the compaction strain. A method exists to estimate compaction strain (ε_c) by using maximum pole density of a phase (Oertel & Curtis, 1972). The ε_c using this method is defined as $\varepsilon_c = \rho_{max}^{-1/2}-1$, where ρ_{max} is the maximum pole density. This is based on an earlier method known as the March model, which assumes that randomly oriented rigid plates in a viscous matrix will develop a preferred orientation when the aggregate is strained (March, 1932). The compaction strain was calculated for the Green River and Mancos Shale samples using the (001) maximum pole density for the constituent clay phases, and is reported in Table 6. In the Green River samples, ε_c = -0.14 to -0.61. In the Mancos Shale samples, ε_c = -0.14 to -0.52. These compare to calculated ε_c = -0.36 to -0.61 in the Qusaiba Shale in Saudi Arabia (Kanitpanyacharoen et al., 2011). In addition to this, Voltolini et al. (2009) found that samples with large clay fractions (75-100% clay by weight) have ε_c = -0.35 to -0.51 in samples that had undergone a 5 MPa compression, and ε_c = -0.48 to -0.65 in samples

Table 6. Compaction strain (ε_c) calculated using the maximum pole density (ρ_{max}) from the (001) pole figure for clay phases in Green River and Mancos samples.

	Illite		Illite-Smectite		Chlorite	
sample	ρ_{max}	ε_c	ρ_{max}	ε_c	ρ_{max}	ε_c
Q16_15160	4.07	-0.50	-	-	4.66	-0.54
Q16_15172	3.79	-0.49	-	-	4.34	-0.52
Q16_15223	2.33	-0.34	-	-	2.61	-0.38
Q16_15264	2.63	-0.38	-	-	2.81	-0.40
Q8_9703	3.58	-0.47	-	-	3.56	-0.47
P2_7135	4.42	-0.52	-	-	5.94	-0.59
Q8_9715_dark	1.81	-0.26	-	-	1.96	-0.29
Q8_9715_light	1.44	-0.17	-	-	1.35	-0.14
EX1_013	4.02	-0.50	1.95	-0.28	2.05	-0.30
EX1_036	6.70	-0.61	3.48	-0.46	2.49	-0.37
EX1_091	1.34	-0.14	-	-	-	-

that had undergone a 50 MPa compression. The compaction strain calculated for the Green River and Mancos Shale samples overlaps these ranges to a significant degree, indicating an extensive compaction history. As the Mancos Shale is a much older formation than the Green River (Cretaceous vs. Eocene), and the samples used in this study come from a much greater depth than the Green River samples, the calculated compaction strains may not be representative of their compaction history. Instead, it is likely that a sample's maximum pole density is imprinted early on in diagenetic history.

Figure 34 shows a plot of P-wave anisotropy versus clay volume fraction for the Green River and Mancos samples used in this study, along with samples from the Qusaiba Shale (Kanitpanyacharoen et al., 2011), and the Bakken Shale (Easley, 2014). From this plot, a strong linear correlation between these two parameters is observed. A best-fit linear approximation has an equation of P-anisotropy = 0.2413*clay volume fraction – 1.7044, with an R^2 value of 0.8995. In a previous study, Allan et al. (2015) found that extrinsic factors, predominantly microcracks and fractures in the shale, accounted for at most 30% of the anisotropy in shales under low confining pressures. For shale in-situ at depth, this will likely be much less as fractures largely close under higher pressures. Thus, since intrinsic anisotropy is the dominant source of anisotropy, the simple linear equation put forth here can be used to estimate P-wave anisotropy fairly closely if the total clay content of a sample is known. Note that absolute velocity values are too fast compared to observed velocities as there is no porosity, fluids, or organic material accounted for in these models. This could potentially provide a relatively easy method to constrain velocity models in a seismic survey. As more shale units around the world are studied for texture and anisotropy, this relationship can be further refined.

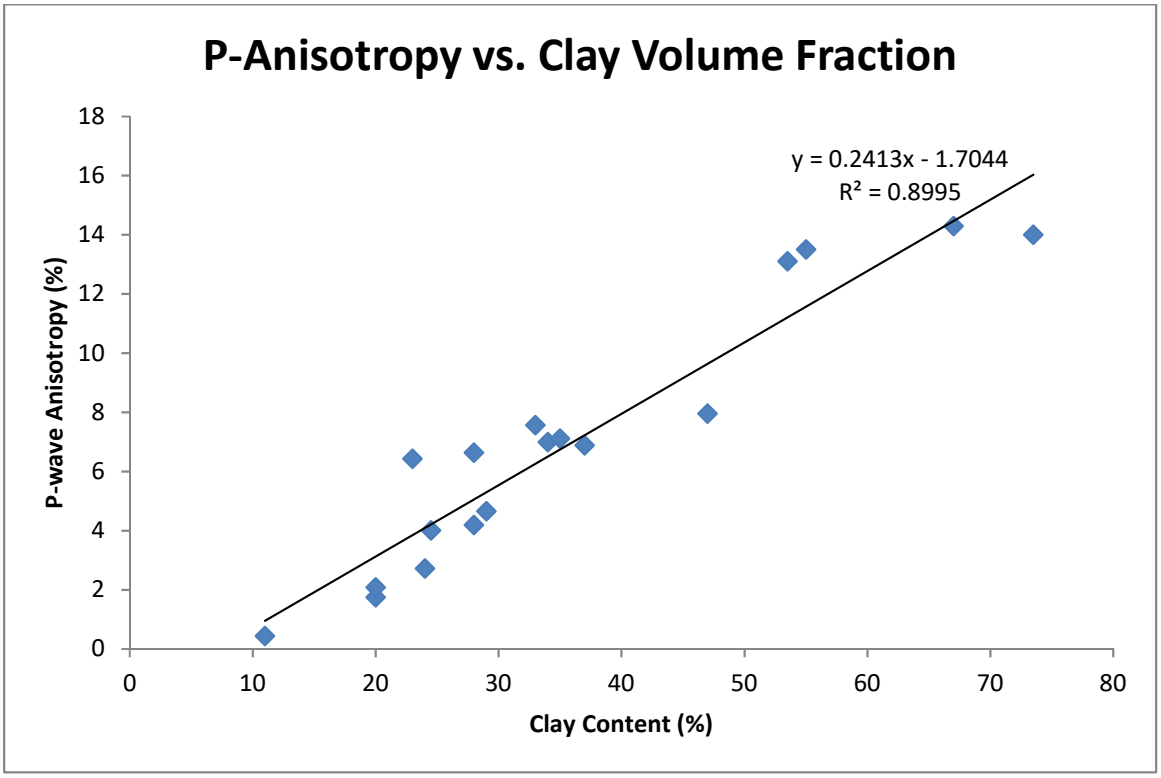

Figure 34. Plot of P-wave anisotropy vs. clay content for all Green River and Mancos Shale samples in this study, along with samples from the Qusaiba Shale (Kanitpanyacharoen et al., 2011) and the Bakken Shale (Easley, 2014). A strong linear relation (R^2 of 0.8995) exists with an equation of P-anisotropy = 0.2413*clay volume fraction – 1.7044.

Conclusion

Eleven shale samples taken from various cores in the Mancos and Green River formations were studied using synchrotron x-ray diffraction. Textures were quantified for the minerals present in these samples, with special attention paid to clay minerals. Clay minerals illite, illite-smectite, and chlorite were strongly textured and are the major contributors to the intrinsic anisotropy that was calculated for each sample. Calculated intrinsic anisotropy in the Mancos and Green River samples was compared to other samples studied from around the world. A plot of P-wave anisotropy versus clay volume fraction was created using data from the Green River and Mancos Shale samples, along with previously studied samples from the Qusaiba and Bakken shales, and reveals a strong linear correlation. A simple linear equation was fit to the data, and can be used to approximate P-wave anisotropy based on a sample's clay volume fraction.

CHAPTER 2

DEFORMATION AND TRANSFORMATION TEXTURES IN NEIGHBORITE ($NaMgF_3$) PEROVSKITE AND POST-PEROVSKITE ANALOGS

Introduction

The D" region of the lower mantle occurs just above the core mantle boundary. This region is seismically complex compared to the majority of the lower mantle, and is characterized by seismic discontinuities, topographical variations, lateral heterogeneity, anisotropy, and ultra-low velocity zones (Garnero & McNamara, 2008; Helmberger, Lay, Ni, & Gumis, 2005; Houser, 2007; Lay & Garnero, 2007; Wookey & Dobson, 2008; Wookey & Kendall, 2007). Some studies of the D" region have revealed large seismic anomalies with high S-wave velocities around the Pacific, surrounding two low velocity regions beneath the central Pacific and southern Africa (Garnero & McNamara, 2008; Houser, 2007; Lay & Garnero, 2007; Masters, Laske, Bolton, & Dziewonski, 2000; Panning & Romanowicz, 2004; Panning & Romanowicz, 2006; Wookey & Dobson, 2008). It has been suggested that these low velocity regions may be "superplumes" of hot material rising from the core mantle boundary due to mantle convection (Burke & Torsvik, 2004; McNamara & Zhong, 2005). D" anisotropy is very complex, but for the most part, horizontal S-wave velocity (V_{SH}) is greater than vertical S-wave velocity (V_{SV}) in the high velocity regions (Panning & Romanowicz, 2004; Panning & Romanowicz,

2006; Wookey & Kendall, 2007). In low velocity regions, anisotropy is more varied with both $V_{SH}>V_{SV}$ and $V_{SV}>V_{SH}$ being seen as well as smaller regions that are relatively isotropic (Panning & Romanowicz, 2004; Panning & Romanowicz, 2006; Wookey & Kendall, 2007).

The D" is the boundary between the solid mantle and the liquid outer core; it is a region between two rather extreme viscosities. As a boundary layer, it can be expected to play an important role in controlling the thermal structure and evolution of the Earth (Tackley, 2000). Numerical modeling and laboratory experiments seem to indicate that deformation is enhanced near boundary layers and large strain deformation is expected to occur in the D" region, particularly in subducted slabs (Loubet, Ribe, & Gamblin, 2009; McNamara, Van Keken, & Karato, 2002; McNamara, Van Keken, & Karato, 2003). In addition to this, it has been suggested based on experimentation and theoretical evidence that the D" layer could be a weaker region than the overlying mantle and so could be expected to localize deformation (Ammann, Brodholt, Wookey, & Dobson, 2010; Hunt et al., 2009). It is thus likely that seismic anisotropies observed in the D" are due to deformation-induced texture, or preferred orientations, of its constituent minerals (Karato, 1998; Loubet et al., 2009; McNamara et al., 2002; McNamara et al., 2003; Wookey & Kendall, 2007).

A phase transition discovered in $MgSiO_3$ from a perovskite (Pv) to a post-perovskite (pPv) structure at conditions very close to those of the core mantle boundary sheds new light on the D" layer (Murakami, Hirose, Kawamura, Sata, & Ohishi, 2004; Oganov & Ono, 2004; Shim, Duffy, Jeanloz, & Shen, 2004). The phase transformation from Pv to pPv can be expected to result in a few percent increase in S-wave velocities with a very

small change in P-wave velocities, which seems to be consistent with global observations (Loubet et al., 2009; Tsuchiya, Tsuchiya, Umemoto, & Wentzcovitch, 2004; Wookey, Stackhouse, Kendall, Brodholt, & Price, 2005). This does not seem to hold true in all regions. In some places, the velocity increase predicted from mineral physics is not large enough to match observed velocities (Lay & Garnero, 2007). It has been suggested that texturing of pPv may be needed to reconcile seismic velocities with the presence of pPv in these regions (Hirose, 2007; Lay & Garnero, 2007). The thickness of the Pv to pPv transformation also remains a question. Studies have shown the top of the D" to be rather sharp, with the layer occurring over a thickness of less than 30 km (Lay, 2008). However, estimates for the coexistence of the Pv and pPv phases for a range of plausible chemical compositions seems to predict larger thicknesses closer to 90 km (Akber-Knutson, Steinle-Neumann, & Asimow, 2005; Catalli, Shim, & Prakapenka, 2009; Ohta, Hirose, Sata, & Ohishi, 2006; Tateno, Hirose, Sata, & Ohishi, 2005). Texturing of pPv could again be the reason for the sharpening of this boundary (Ammann et al., 2010; Murakami, Hirose, Sata, & Ohishi, 2005).

Although texturing of pPv is critical to fully understanding the D" (Cottaar, McNamara, Romanowicz, & Wenk, 2014; Nowacki, Walker, Wookey, & Kendall, 2013; Wenk, Cottaar, Tome, McNamara, & Romanowicz, 2011), data on texture development in post-perovskite are limited. Early studies proposed that slip should occur off the (010) plane, based on the layered structure of pPv (Iitaka, Hirose, Kawamura, & Murakami, 2004; Murakami et al., 2004; Oganov & Ono, 2004;). However, Oganov, Martonak, Laio, Raiteri, and Parrinello (2005) predicted slip on $\{110\}\langle 1\bar{1}0\rangle$ using first-principles metadynamics and energetics of stacking faults. Early room temperature diamond anvil

cell experiments on $MgGeO_3$ pPv and $MgSiO_3$ pPv using radial diffraction found textures with (100) planes at high angles to compression, which was interpreted as a result of slip on {110} and (100) (Merkel et al., 2006; Merkel et al., 2007). This was consistent with Oganov et al. (2005). These works were in conflict with other first-principles calculations, which modeled dislocation cores based on the Peierls-Nabarro model. These found (010)[001] to be the dominant slip system in $MgSiO_3$ pPv (Carrez, Ferre, & Cordier, 2007a,b). This work was expanded by Metsue, Carrez, Mainprice, and Cordier (2009) to include $CaIrO_3$ and $MgGeO_3$ pPv. This study suggested that for $CaIrO_3$ pPv, (010)[001] slip should be the easiest slip system while (001)[100] should be the easiest for $MgGeO_3$ pPv.

$CaIrO_3$ has been experimentally the most studied for deformation mechanisms of the pPv structured compounds (Miyagi et al., 2008; Miyajima, Ohgushi, Ichihara, & Yagi, 2006; Miyajima & Walte, 2009; Niwa et al., 2007; Walte, Heidelbach, Miyajima, & Frost, 2007; Walte et al., 2009; Yamazaki, Yoshino, Ohfuji, Ando, & Yonedu, 2006). This is mostly due to its ease of study, as it is stable in the pPv structure at ambient conditions (Rodi & Babel, 1965). Transmission electron microscopy (TEM) was use to study dislocation microstructures generated during the synthesis of $CaIrO_3$ pPv and Burgers vectors b = [100] with some $b = \langle u0w \rangle$ were found, and it was suggested that (010) was the most likely slip plane in $CaIrO_3$ pPv (Miyajima et al., 2006). Yamazaki et al. (2006) performed high-temperature shear experiments on $CaIrO_3$ pPv and used scanning electron microscopy (SEM) and electron back-scatter diffraction (EBSD) on recovered samples to find (010)[100] slip on the basis of fabric observations. EBSD and TEM experiments on samples recovered from high-temperature coaxial shortening and

simple shear experiments in the D-DIA multi-anvil press to a higher pressure of 3 GPa seem to provide further support for this conclusion (Walte et al., 2007). Room-temperature DAC experiments on $CaIrO_3$ pPv to 6 GPa obtained textures consistent with (010) slip, seeming to show that the dominant slip system in $CaIrO_3$ pPv is the same at room temperature as it is at higher temperatures (Niwa et al., 2007). Miyagi et al. (2008) expanded on these studies further by performing radial diffraction texture measurements on $CaIrO_3$ pPv deformed in the D-DIA at a range of pressure-temperature conditions up to 6 GPa and 1300 K and at varying strain rates and found that texture and dominant slip systems did not change with temperature, pressure, or strain rate. Polycrystal plasticity modeling using the Visco Plastic Self-Consistent (VPSC) model (Lebensohn & Tome, 1994) showed that experimental textures could be explained by slip on (010)[100] with some slip on (010)⟨101⟩, but that (010)[001] slip generated textures incompatible with the experiments (Miyagi et al., 200).

The evidence that slip on (010)[100] is the dominant system in $CaIrO_3$ seems to be quite robust based on the large number of independent and consistent experimental results (Miyagi et al., 2008; Miyajima et al., 2006; Miyajima & Walte, 2009; Niwa et al., 2007; Walte et al., 2007; Walte et al., 2009; Yamazaki et al., 2006). However, it is unclear as to why different textures are observed in $MgGeO_3$ pPv and $MgSiO_3$ pPv (Merkel et al., 2006; Merkel et al., 2007). Yamazaki et al. (2006) proposed that differences in slip systems observed for high temperature deformation of $CaIrO_3$ pPv and room-temperature DAC experiments on $MgGeO_3$ pPv and $MgSiO_3$ pPv (Merkel et al., 2006; Merkel et al., 2007) were because of a change in dominant slip systems at high temperatures in the pPv structure. However, it has been shown that $CaIrO_3$ pPv has the

same textures at room temperature and high temperature (Miyagi et al., 2008; Niwa et al., 2007).

It is also possible that some of the DAC experiments could be recording transformation textures (Okada, Yagi, Niwa, & Kikegawa, 2010; Santillian, Shim, Shen, & Prakapenka, 2006; Walte et al., 2007; Walte et al., 2009;). Walte et al. (2009) did experiments transforming $CaIrO_3$ Pv to pPv. Here it was observed that after transformation from Pv, the pPv phase exhibited a texture of (100) planes almost normal to the compression directions, which was consistent with the DAC results on $MgGeO_3$ pPv and $MgSiO_3$ pPv (Merkel et al., 2006; Merkel et al., 2007). After deformation, this changed to (010) planes at high angles to compression indicating activity of slip on (010). It was then concluded that results of Merkel et al. (2006) and Merkel et al. (2007) recorded transformation textures and that deformation should then occur on (010) (Walte et al., 2009). It is important to keep in mind that in the experiments of Merkel et al. (2006) and Merkel et al. (2007), the synthesis of pPv was accomplished directly from the enstatite phase, bypassing the Pv phase completely.

Okada et al. (2010) performed room-temperature DAC experiments on $MgGeO_3$ pPv using both radial and axial diffraction. When transforming the Pv phase to pPv, it was observed that just after transformation, (001) planes were oriented at high angles to the compression axis, which was different from the transformation textures observed in $CaIrO_3$ pPv by Walte et al. (2009). In addition to this, axial diffraction measurements were also performed on $MgGeO_3$ pPv synthesized from enstatite, and it was found that (100) and {110} planes aligned at high angles to compression just after transformation, which is consistent with Merkel et al. (2006) and Merkel et al. (2007). After further

compression, changes in the axial diffraction patterns seem to suggest that (001) planes become aligned normal to compression (Okada et al., 2010). It is important to note that inference of textures from axial diffraction measurements is unreliable. Axial diffraction is only able to provide information on lattice planes oriented at very low angles to compression and contains no direct information on lattice planes in other orientations.

Miyagi, Kanitpanyacharoen, Stackhouse, Militzer, and Wenk (2011) performed DAC experiments on $MgGeO_3$ pPv, synthesizing $MgGeO_3$ pPv from both an enstatite phase, and a Pv phase. When synthesized from an enstatite phase, it was found that $MgGeO_3$ pPv had a transformation texture of (100) planes at high angles to compression, shifting to (001) upon deformation, with a dominant slip system of (001)[100]. The (100) texture observed initially is consistent with that of Merkel et al. (2006) and Merkel et al. (2007), providing further evidence that that is a transformation texture. The slip on the (001) plane in $MgGeO_3$ is consistent with Okada et al. (2010). When synthesized from a (001) pretextured Pv phase, $MgGeO_3$ pPv shows a (001) transformation texture, indicating that (001) Pv becomes (001) in the pPv structure. The (001) texture in pPv did not change with further deformation. Dobsen et al. (2013) studied transformation textures in $NaNiF_3$ Pv and pPv using TEM-microscopy on samples recovered from mutli-anvil experiments. This study found that [001] directions were preserved between the two structures and (010) Pv was approximately parallel to (110) pPv. Texture inheritance in $MgGeO_3$ and $NaNiF_3$ is in contrast to $CaIrO_3$ pPv transformed from the Pv phase. When a sample of $CaIrO_3$ Pv was transformed to pPv, a (100) texture was observed; however, since the Pv sample was randomly oriented, an orientation relation between the Pv and pPv phases was ruled out (Walte et al., 2009).

Another explanation for differences between the observed textures in $CaIrO_3$, $MgGeO_3$, and $MgSiO_3$ pPv is that $CaIrO_3$ pPv may have different deformation behavior than $MgGeO_3$ and $MgSiO_3$ pPv (Miyagi et al., 2008). $CaIrO_3$ pPv has very different structural parameters than $MgSiO_3$ pPv, which could account for this. The bond lengths, bond angles, and octahedral distortions of $MgGeO_3$ pPv are much closer to those of $MgSiO_3$ than $CaIrO_3$ pPv (Kubo et al., 2008). Raman spectroscopy measurements have also indicated that bonding in $CaIrO_3$ pPv is different from other pPv structured compounds (Hustoft, Shim, Kubo, & Nishiyama, 2008). Also, first-principles computations find $CaIrO_3$ pPv to have elastic properties and an electronic structure that are inconsistent with $MgSiO_3$ pPv (Tsuchiya & Tsuchiya, 2007).

There are still other pPv structured compounds to be studied that can aid in the understanding of texture development and slip systems. In particular, $NaXF_3$ compounds are structurally closer to $MgSiO_3$ pPv than $MgGeO_3$ and $CaIrO_3$ (Dobsen et al., 2013; Kubo et al., 2008). Here, a new radial diffraction experiment was performed $NaMgF_3$ pPv compound synthesized from the Pv structured neighborite phase.

Experimental Procedure

Experiments were performed at HP-CAT, beamline 16 ID-B of the Advanced Photon Source at Argonne National Laboratory. A modified Mao-Bell type cell with large openings for radial diffraction was used. Diamond anvils with 200 μm culets were mounted in the cell. The boron gasket had a precompressed thickness of 50 μm, with a 50 μm sample chamber. A finely ground $NaMgF_3$ sample was mixed with 5 wt% Pt powder, which acts as a pressure calibrant. A radial diffraction geometry, where the x-

ray beam is orthogonal to the compression axis, was used. Diffraction images were collected using a MarCCD detector, with an 8-second exposure time. The x-ray wavelength was 0.619921 Å and the beam size was 10 μm x 10 μm. A CeO_2 standard was used to calibrate sample to detector distance, beam center, instrument broadening, and detector tilt. After an initial compression to 37 Gpa, the phase transformation to pPv was induced at approximately 1400 K using single-sided laser heating. Pressure was then increased incrementally to a maximum of 66 GPa at room temperature. Pressures were calculated using the equation of state for platinum from Fei et al. (2007).

Data Analysis

Diffraction images were initially processed using Fit2d (Hammersley, 1997). Images were integrated over 5^0 arcs into 72 discrete spectra (Figure 35). Spectra that contained the beam stop and diamond spots were removed. The images were then analyzed using the MAUD software, which implements the Rietveld method (Lutterotti et al., 1997). Backgrounds were interpolated using 10 manually selected points on each image between diffraction peaks. A Q-space range of 2.25 to 3.87 $Å^{-1}$ was used. Images were refined for crystal lattice parameters, crystallite size, lattice strain, and preferred orientation. Popa line broadening with an isotropic size-strain model was used for the refinement of crystallite size (Popa & Balzar, 2002). The moment pole stress model was used to refine lattice strains and calculate stress (Matthies & Humbert, 1993; Matthies, Priesmeyer, & Daymond, 2001). A bulk path geometric mean, which is between the Voigt and Reuss models, was used for the micromechanical model (Matthies et al., 2001). Texture analysis (preferred orientations) was done using the E-WIMV algorithm to generate an

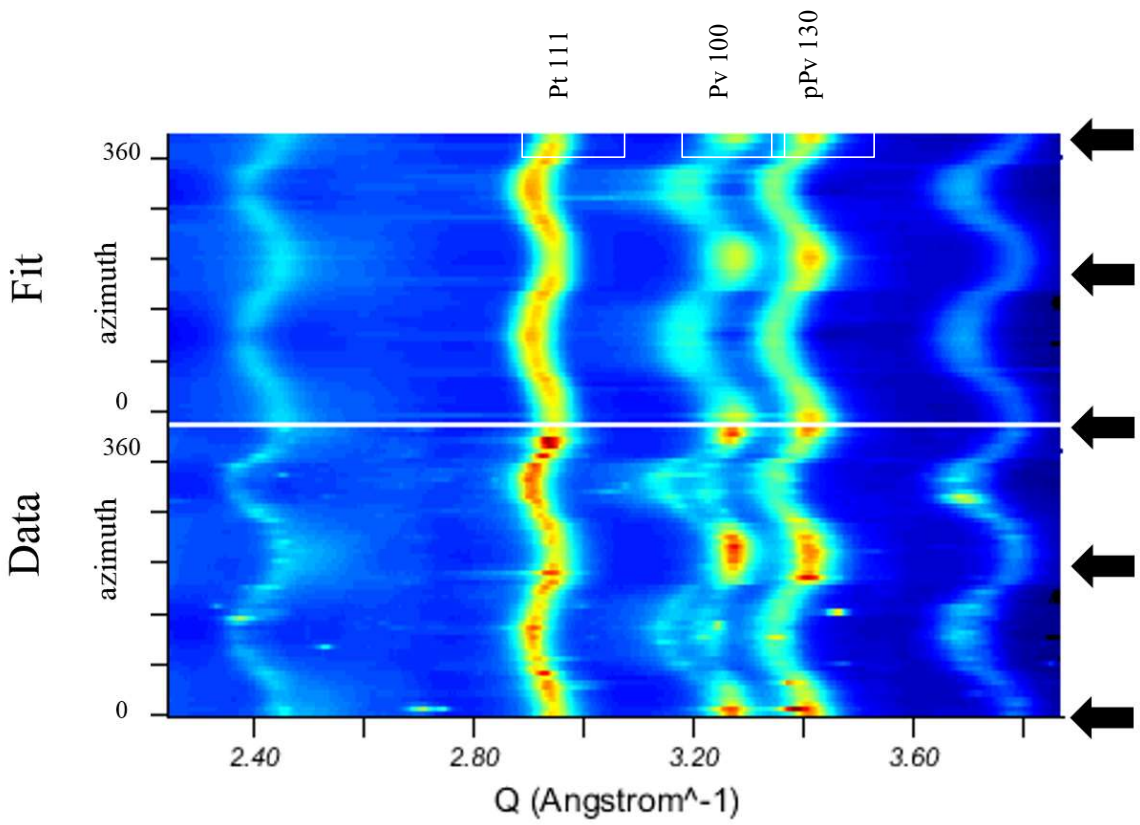

Figure 35. Diffraction image of $NaMgF_3$ pPv at 66 GPa, integrated into 72 spectra (bottom), as well as the Rietveld refinement model fit (top). The 111 platinum peak has been labeled, along with the pPv 130 peak, and the Pv 100 peak from residual Pv that did not convert to pPv. Again, texture can be seen as intensity variations along diffraction peaks. Stress can also be seen, and calculated, from the variation of the peak position along the azimuth.

orientation distribution function (O.D.F.) (Matthies & Vinel, 1982). A 15^0 resolution was used, and cylindrical symmetry was imposed about the compression axis. The O.D.F. was then exported and smoothed in BEARTEX. Axial compression textures can be represented using an inverse pole figure of the compression direction. Pole densities are displayed in multiples of random distribution (m.r.d.), where an m.r.d. of 1 represents a random distribution.

Results

Table 7 shows refinement results for unit cell lattice parameters, crystallite size, microstrain, and inverse pole figure maximums. Under compression, microstrain increases and unit cell parameters and crystallite size decrease. The crystallite size obtained through these refinements represents an average of the size throughout the sample. A qualitative sense of the distribution of crystallite size can be seen in the diffraction image in Figure 35; a spotty image means larger grains are present, whereas a smoother image points to smaller grain sizes. For this experiment, there is a fairly spotty pattern, indicating the presence of larger grains. This will also make texture extraction less reliable and results should only be viewed as semiquantitative.

Texture Results

Inverse pole figures for the Pv phase prior to conversion, the pPv phase just after conversion, and at higher pressure are shown in Figure 36. The Pv phase exhibits a very strong (100) texture at 37 GPa, prior to conversion to pPv, with a m m.r.d. of 6.4. Just after the sample is heated and is converted to the pPv phase, a (130) texture is seen with a

Table 7. Unit cell parameters, crystallite size, microstrain, and inverse pole figure maximum for $NaMgF_3$ pPv at 37, 50, 59, and 66 GPa. Cell parameters and crystallite size decrease with pressure. Likewise, microstrain increases with pressure. The maximum m.r.d. (multiples of random distribution) value of the inverse pole figure increases as well. As can be seen in Figure 36, this maximum occurs with a (130) texture.

Pressure (Gpa)	Unit Cell Parameters (Å)			Crystallite Size (Å)	Microstrain	IPF Max (m.r.d.)
	a	b	c			
37 GPa	2.7973	8.7640	6.9330	188.5	0.00139	2.37
50 Gpa	2.7479	8.5948	6.8210	102.2	0.00214	3.21
59 Gpa	2.7281	8.4822	6.7955	100.1	0.00218	3.26
66 GPa	2.7259	8.3052	6.7371	76.7	0.00229	3.43

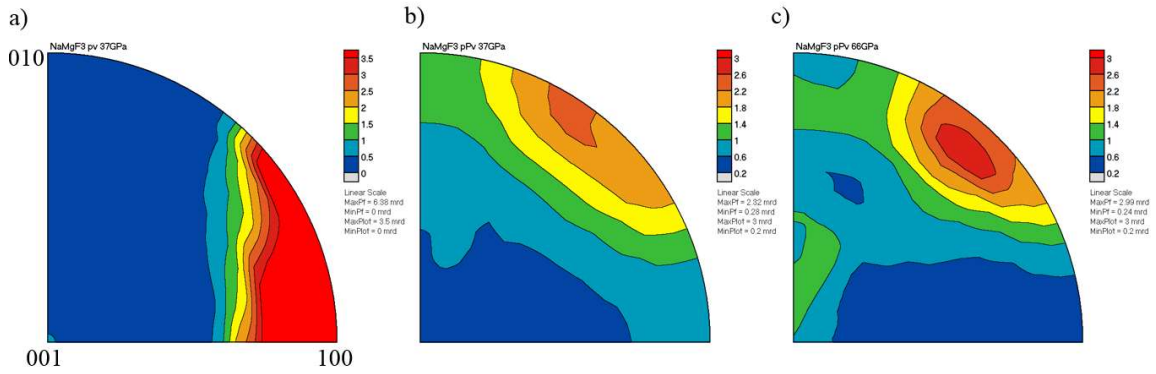

Figure 36. Inverse pole figures for a) $NaMgF_3$ Pv at 37 GPa, prior to conversion b) $NaMgF_3$ pPv at 37 GPa, just after conversion, and c) $NaMgF_3$ pPv at 66 GPa upon further compression. In a), a strong (100) texture can be seen. Immediately upon conversion, in b), this becomes a (130) transformation texture in the pPv phase. This (130) texture appears as if it is beginning to shift towards an (001) texture upon compression to 66 GPa in c).

maximum of 2.4 m.r.d. Upon compression to 66 GPa, a shoulder develops at (001).

Discussion

The strong (100) texture seen in the $NaMgF_3$ Pv phase develops immediately upon the closure of the DAC, and remains until conversion to pPv. Miyagi and Wenk (2016) performed visco-plastic self-consistent (VPSC) modelling to show that an (001) texturecan develop due to twinning {110}<1-10>, and/or slip on (100). Kaercher et al. (2016) studied deformation of $NaMgF_3$ Pv in the D-DIA over a range of temperature and pressure conditions, and concluded that the (100) texture results from slip on (100) planes. The transformation texture for the Pv to pPv transition, or (100) texture to (130) in pPv, is consistent with theoretical work done by Tsuchiya et al. (2004), and Oganov et al. (2005), as well as experimental work on $MgGeO_3$ Pv to pPv (Miyagi et al., 2011) and on $NaNiF_3$ Pv to pPv (Dobson et al., 2013).

Visco-plastic self-consistent (VPSC) modeling was used to simulate the effects of different dominant slips systems in the $NaMgF_3$ pPv phase. The results of these simulations can be seen in Figure 37. These simulations used the transformation texture in Figure 36b as a starting point for the simulation. Each simulation consisted of 30 steps, each step being an increase of strain by 1%. Modeling took into account 2000 individual grains of equal size and shape. The closest match appears to be a dominant slip system of (001)[100]. This is consistent with DAC deformations experiments on $MgGeO_3$ pPv (Miyagi et al., 2011) and $MgSiO_3$ (Miyagi et al., 2010), which found dominant slip on (001). This is in contrast to $CaIrO_3$, which conclusively deforms on (010) planes (Miyagi et al., 2008F; Miyajima et al., 2006; Miyajima & Walte, 2009; Niwa et al., 2007; Walte

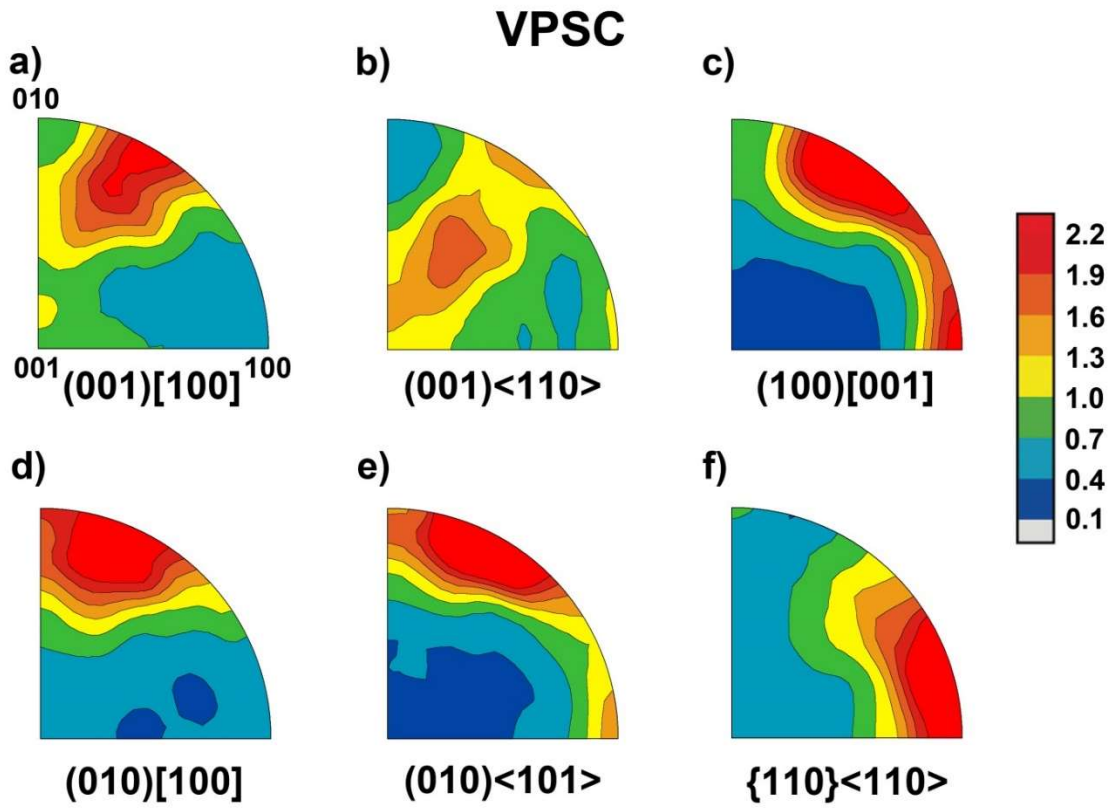

Figure 37. Results of VPSC modelling for dominant slip systems of a) (001)[100], b) (001)<110>, c) (100)[001], d) (010)[100], e) (010)<101>, and f) {110}<110>. From Figure 36, it appears as if the texture seen in $NaMgF_3$ pPv at 66GPa most closely resembles the results of a), suggesting a (001)[100] slip system as the easiest slip system.

et al., 2007; Walte et al., 2009; Yamazaki et al., 2006). Thus it appears that, of all the pPv structured compounds studied, all slip on (001) except for $CaIrO_3$. Simulations of anisotropy development in the D" show that (001) slip in pPv will produce shear waves splitting of $V_{sh} > V_{sv}$ (Cottaar et al., 2014; Wenk et al., 2011) consistent with shear wave splitting observations in the circum-Pacific region.

Conclusion

A new experiment was performed on the neighborite ($NaMgF_3$) Pv and pPv analogs. A phase transformation to the post-perovskite structure was induced at a pressure of 37 GPa by heating the sample. Pressure was increased incrementally up to 66 GPa. The strong (100) texture seen in the $NaMgF_3$ Pv phase is transformed to a (130) texture in the pPv phase. Indicating that (100) Pv planes become (130) planes in the pPv phase. This is consistent with transformation relationships proposed for $MgGeO_3$ (Miyagi et al., 2011) and $NaNiF_3$ (Dobsen et al., 2013), but is in contrast to $CaIrO_3$ (Walte et al., 2009). Under further compression, a shoulder develops towards (001). VPSC simulations show that the (001)[100] slip system most closely matches the observed results. Slip on (001) matches results of all pPv structured materials, except for $CaIrO_3$, which slips on (010). Slip on (001) in the D" layer would result in shear wave splitting of $V_{sh} > V_{sv,}$ which matches seismic observations in the circum-Pacific region.

REFERENCES

Akber-Knutson, S., Steinle-Neumann, G., & Asimow, P. (2005). Effect of Al on the sharpness of the MgSiO3 perovskite to post-perovskite phase transition. *Geophysical Reseach Letters, 32*(14), L14303. doi:10.1029/2005GL023192

Allan, A. M., Kanitpanyacharoen, W., & Vanorio, T. (2015). A multiscale methodology for the analysis of velocity anisotropy in organic-rich shale. *Geophysics, 80*(4), C73-C88. doi:10.1190/geo2014-0192.1

Ammann, M., Brodholt, J., Wookey, J., & Dobson, D. (2010). First-principles constraints on diffusion in lower-mantle minerals and a weak D" layer. *Nature, 465*(7297), 462-465. doi:10.1038/nature09052

Bass, J. D. (1995). *Elasticity of minerals, glasses and melts in mineral physics and crystallography: A handbook of phsyical constants.* Washington, DC: American Geophysical Union.

Burke, K., & Torsvik, T. (2004). Derivation of Large Igneous Provinces of the past 200 million years from long-term heterogeneities in the deep mantle. *Earth and Planetary Science Letters, 227*(3), 531-538. doi:10.1016/j.epsl.2004.09.015

Carrez, P., Ferre, D., & Cordier, P. (2007a). Peierls-Nabarro model for dislocations in MgSiO3 post-perovskite calculated at 120GPa from first principles. *Philosophical Magazine, 87*(22), 3229-3247. doi:10.1080/14786430701268914

Carrez, P., Ferre, D., & Cordier, P. (2007b). Implications for plastic flow in the deep mantle from modelling dislocations in MgSiO3 minerals. *Nature, 446*(7131), 68-70. doi:10.1038/nature05593

Carroll, A., & Bohacs, K. M. (1999). Stratigraphic classification of ancient lakes: Balancing tectonic and climatic controls. *Geology, 27*(2), 99-102.

Catalli, K., Shim, S., & Prakapenka, V. (2009). Thickness and Clapeyron slope of the post-perovskite boundary. *Nature, 462*(7274), 782-785. doi:10.1038/nature08598

Cottaar, S., Li, M., McNamara, A. K., Romanowicz, B., & Wenk, H.-R. (2014). Synthetic seismic anisotropy models within a slab impinging on the core-mantle boundary. *Geophysical Journal International, 199*(1), 164-177. doi:10.1093/gji/ggu24

Council, G. P. (2009). *Modern Shale Gas Development in the United States: A Primer.* U.S. Department of Energy.

Cross, C. W., & Purington, C. W. (1899). Description of the Telluride Quadrangle, Colorado. *U.S. Geological Survey Atlas, Folio, 57*(19).

DeCelles, P. G. (1994). Late Cretaceous-Paleocene synorogenic sedimentation and kinematic history of the Sevier thrust belt, northeast Utah and southwest Wyoming. *Geological Society of America Bulletin, 106*(1), 23-56.

DeCelles, P. G., & Giles, K. A. (1996). Foreland basin systems. *Basin Research, 8*(2), 105-123.

Dickinson, W. R., Klute, M. A., Hayes, M. J., Janecke, S. U., Lundin, E. R., McKittrick, M. A., & Olivares, M. D. (1988). Paleogeographic and paleotectonic setting of Laramide sedimentary basins in the central Rocky Mountain region. *Geological Society of America Bulletin, 100*(7), 1023-1039.

Dobson, D., Miyajima, N., Nestola, F., Alvaro, M., Casati, N., Liebske, C., . . . Walker, A. (2013). Strong inheritance of texture between perovskite and post-perovskite in the D" layer. *Nature Geoscience, 6*(7), 575-578. doi:10.1038/ngeo1844

DOE. (2011). *Topical Report: Core-Based Integrated Sedimentologic, Stratigraphic, and Geochemical Analysis of the Oil Shale Bearing Green River Formation, Uinta Basin, Utah.* United States Department of Energy.

Easley, E. J. (2014). *A fracture and texture analysis of the Bakken formation* (Master's thesis). Retrieved from Montana State University Scholarworks theses and dissertation database. (Catalog Key: 2719495).

Fei, Y., Ricolleua, A., Frank, M., Mibe, K., Shen, G., & Prakapenka, V. (2007). Toward an internally consistent pressure scale. *Procedings of the National Academy of Science of the United States of America, 104*(22), 9182-9186.

Garnero, E., & McNamara, A. (2008). Structure and dynamics of Earth's lower mantle. *Science, 320*(5876), 626-628. doi:10.1126/science.1148028

Gualtieri, A. F. (200). Accuracy of XRPD QPA using the combined Rietvled-RIR method. *Journal of Applied Crystallography, 33*(2), 267-278.

Hammersley, A. (1997). FIT2D: An indroduction and overview. *ESRF Internal Report*, ESRF97HA02T.

Helmberger, D., Lay, T., Ni, S., & Gumis, M. (2005). Deep mantle structure and the postperovskite phase transition. *Proceedings of the National Academy of Sciences of the United States of America, 102*(48), 17257-17263.

Hill, R. (1963). Elastic properties of reinforced solids: Some theoretical principles. *Journal of the Mechanics and Physics of Solids, 11*(5), 357-372.

Hirose, K. (2007). Discovery of post-perovskite phase transition and the nature of the D" layer. In K. Hirose, D. Yuen, T. Lay, & J. P. Brodholt (Eds.), *Post-perovskite, the last mantle phase transition* (pp. 19-35). Washington, DC: American Geophysical Union.

Hornby, B. E. (1994). *The elastic properties of shales* (Doctoral Dissertation). Retrieved from ProQuest disserations and theses database. (UMI No. U065608).

Horton, B. (2012). *Variability of the Mancos Shale: Developing preliminary depositional and sequence stratigraphic models of a developing shale gas play* (Master's thesis). Retrieved from ProQuest disserations and theses database. (UMI No. 1516621).

Houser, C. (2007). Constraints on the presence of absence of post-perovskite in the lowermost mantle from long-period seismology. In K. Hirose, D. Yuen, T. Lay, & J. P. Brodholt (Eds.), *Post-perovskite, the last mantle phase transition* (pp. 191-216). Washington, DC: American Geophysical Union.

Hunt, S., Weidner, D., Li, L., Wang, L., Walte, N., & Brodholt, J. (2009). Weakening of calcium iridate during its transformation from perovskite to post-perovskite. *Nature Geoscience, 2*(11), 794-797. doi:10.1038/ngeo663

Hustoft, J., Shim, S., Kubo, A., & Nishiyama, N. (2008). Raman spectroscopy of CaIrO3 postperovskite up to 30GPa. *American Mineralogist, 93*(10), 1654-1658.

IHS, I. (2012a). Questar Red Wash #8ML-6-9-24. *PI/Dwights PLUS on CD Well Summary Report Retrieved January 24, 2012*.

IHS, I. (2012b). Questar Glenn Bench #16M-28-8-21. *PI/Dwights PLUS on CD Well Summary Report Retrieved January 24, 2012*.

IHS, I. (2012c). Pioneer Main Canyon Federal #23-7-15S-23E. *PI/Dwights PLUS on CD Well Summary Report Retrieved January 24, 2012*.

Iitaka, T., Hirose, K., Kawamura, K., & Murakami, M. (2004). The elasticity of the MgSiO3 post-perovskite phase in the Earth's lowermost mantle. *Nature, 430*(6998), 442-445.

Johnson, R. C. (2003). *Depositional framework of the Upper Cretaceous Mancos Shale and the lower part of the Upper Cretaceous Mesaverde Group, Western Colorado and Eastern Utah.* Denver: U.S. Geological Survey, Information Services.

Jones, L. E., & Wang, H. F. (1981). Ultrasonic velocities in Cretaceous shales from the Williston Basin. *Geophysics, 46*(3), 288-297.

Joswig, W., Tagai, T., Korekawa, M., & Wenk, H.-R. (1980). Die Bestimmung der Al/Si-Verteilung mittels Neutronenbeugung in einen Plagioklas An66. *Zeitschrift fuer Kristallographie, 151*, 77-89.

Kaercher, P., Miyagi, L., Kanitpanyacharoen, W., Zepeda-Alarcon, E., Wang, Y., Parkinson, D., . . . Wenk, H.-R. (2016). Two-phase deformation of lower mantle mineral analogs. *Earth and PLanetary Science Letters, 456*, 134-145. doi:10.1016/j.epsl.2016.09.030

Kanitpanyacharoen, W., Wenk, H.-R., Kets, F., Lehr, C., & Wirth, R. (2011). Texture and anisotropy analysis of Qusaiba shales. *Geophysical Prospecting, 59*(3), 536-556. doi:10.1111/j.1365-2478.2010.00942.x

Karato, S. (1998). Seismic anisotropy in the deep mantle, boundary layers and the geometry of mantle convection. *Pure and Applied Geophysics, 151*(2-4), 565-587.

Kauffman, E. G. (1977). Geological and biological overview; Western Interior Cretaceous basin. *The Mountain Geologist, 149*, 75-99.

Kennedy, A. D. (2011). *Geologic predictors of the hydrocarbon extraction potential of the Mancos Shale* (Master's thesis). Retrieved from ProQuest disserations and theses database. (UMI No. 1502996).

Kubo, A., Kiefer, B., Shim, S., Shen, G., Prakapenka, V., & Duffy, T. (2008). Rietveld structure refinement of MgGeO3 post-perovskite phase to 1Mbar. *American Mineralogist, 93*(7), 965-976.

Lay, T. (2008). Sharpness of the D" discontinuity beneath the Cocos Plate: Implications for the perovskite to post-perovskite phase transition. *Geophysical Research Letters, 35*(3), L03304. doi:10.1029/2007GL032465

Lay, T., & Gamero, E. (2007). Reconciling the post-perovskite phase with seismological observations of lowermost mantle structure. In K. Hirose, D. Yuen, T. Lay, & J. P. Brodholt (Eds.), *Post-Perovskite, The last mantle phase transition* (pp. 29-154). Washington, DC: American Geophysical Union.

Lebensohn, R., & Tome, C. (1994). A self-consistent viscoplastic model: Prediction of rolling textures of anisotropic polycrystals. *Materials Science and Engineering, 175*(1-2), 71-82.

Livaccari, R. F. (1991). Role of crustal thickening and extensional collapse in the tectonic evolution of the Sevier-Laramide Orogeny, Western United States. *Geology, 19*(11), 1104-1107.

Londardelli, I., Wenk, H.-R., & Ren, Y. (2007). Preferred orientation and elastic anisotropy in shales. *Geophysics, 72*(2), D33-D40. doi:10.1190/1.2435966

Loubet, N., Ribe, N., & Gamblin, Y. (2009). Deformation modes of subducted lithosphere at the core-mantle boundary: An experimental investigaion. *Geochemistry, Geophysics, Geosystems, 10*(10), 10004.

Lutterotti, L., Matthies, S., Wenk, H., Schultz, A., & Richardson, J. (1997). Combined texture and structure analysis of deformed limestone from time-of-flight neutron diffraction spectra. *Journal of Applied Physics, 81*(2), 594. doi:10.1063/1.364220

March, A. (1932). Mathematische Theorie der Regelung nach der Korngestalt bei affiner Deformation. *Zeitschrift fuer Kristallographie, 81*, 285-297.

Masters, G., Laske, G., Bolton, H., & Dziewonski, A. (2000). The relative behavior of shear velocity, bulk sound speed, and compressional velocity in the mantle: Implications for chemical and thermal structure. In S. I. Karato, A. M. Forte, R. C. Liebermann, G. Masters, & L. Stixrude (Eds.), *Earth's deep interior: Mineral physics and tomography from the atomic to global scale* (pp. 63-87). Washington, DC: American Geophysical Union.

Matthies, S., & Humbert, M. (1993). The realization of the concept of a geometric mean for calculating physical constants of polycrystalline materials. *Physica Status Solidi B, 177*(2), K47-K50.

Matthies, S., & Vinel, G. W. (1982). On the reproduction of the orientation distribution function of textured samples from reduced pole figures using the concept of conditional ghost correction. *Physica Status Solidi B, 112*(2), K111-K114.

Matthies, S., & Wenk, H.-R. (2009). Transformations for monoclinic crystal symmetry in texture analysis. *Journal of Applied Crystallography, 42*(4), 564-571. doi:10.1107/S0021889809018172

Matthies, S., Priesmeyer, H., & Daymond, M. (2001). On the diffractive determination of single-crystal elastic constants using polycrstalline samples. *Journal of Applied Crystallography, 34*(5), 585-601. doi:10.1107/S0021889801010482

McNamara, A., & Zhong, S. (2005). Thermochemical structures beneath Africa and the Pacific Ocean. *Nature, 437*(7062), 1136-1139. doi:10.1038/nature04066

McNamara, A., Van Keken, P., & Karato, S. (2002). Development of anisotropic structure in the Earth's lower mantle by solid-state convection. *Nature, 416*(6878), 310-314.

McNamara, A., Van Keken, P., & Karato, S. (2003). Development of finite strain in the convecting lower mantle and its implications for seismic anisotropy. *Journal of Geophysical Research, 108*(B5), 2230.

Merkel, S., Kubo, A., Miyagi, L., Speziale, S., Duffy, T., & Mao, H. (2006). Plastic deformation of MgGeO3 post-perovskite at lower mantle pressures. *Science, 311*(5761), 644-646. doi:10.1126/science.1121808

Merkel, S., McNamara, A., Kubo, A., Speziale, S., Miyagi, L., & Meng, Y. (2007). Deformation of (Mg,Fe)SiO3 post-perovskite and D" anisotropy. *Science, 316*(5832), 1729-1732. doi:10.1126/science.1140609

Metsue, A., Carrez, P., Mainprice, D., & Cordier, P. (2009). Numerical modelling of dislocations and deformation mechanisms in CaIrO3 and MgGeO3 post-perovskites-Comparison with mgSiO3 post-perovskite. *Physics of the Earth and Planetary Interiors, 174*(1), 165-173. doi:10.1016/j.pepi.2008.04.003

Militzer, B., Wenk, H.-R., Stackhouse, S., & Stixrude, L. (2011). Elastic properties of illite-smectite and kaolinite based on first principles and their significance for the anisotropy of shales. *American Mineralogist, 96*(1), 125-137. doi:10.2138/am.2011.3558

Miyagi, L., & Wenk, H.-R. (2016). Texture development and slip systems in bridgmanite and bridgmanite + ferropericlase aggregates. *Physics and Chemistry of Minerals, 43*(8), 597-613. doi:10.1007/s00269-016-0820-y

Miyagi, L., Kanitpanyacharoen, W., Stackhouse, S., Militzer, B., & Wenk, H. (2011). The enigma of post-perovskite anisotropy: Deformation versus transformation textures. *Physics and Chemistry of Minerals, 38*(9), 665-678. doi:10.1007/s00269-011-0439-y

Miyagi, L., Nishiyama, N., Wang, Y., Kubo, A., West, D., & Cava, R. (2008). Deformation and texture development in CaIrO3 post-perovskite phase up to 6GPa and 1300K. *Earth and Planetary Science Letters, 268*(3), 515-525. doi:10.1016/j.epsl.2008.02.005

Miyajima, N., & Walte, N. (2009). Burgers vector determination in deformed perovskite and post-perovskite of CaIrO3 using thickness fringes in weak-beam dark-field images. *Ultramicroscopy, 109*(6), 683-692. doi:10.1016/j.ultramic.2009.01.010

Miyajima, N., Ohgushi, K., Ichihara, m., & Yagi, T. (2006). Crystal morphology and dislocation microstructures of CaIrO3: A TEM study of an analogue of the MgSiO3 post-perovskite phase. *Geophysical Research Letters, 33*(12), L12302. doi:10.1029/2005GL025001

Murakami, M., Hirose, K., Kawamura, K., Sata, N., & Ohishi, Y. (2004). Post-perovskite Phase transition in MgSiO3. *Science, 304*(5672), 855-858. doi:10.1126/science.1095932

Murakami, M., Hirose, K., Sata, N., & Ohishi, Y. (2005). Post perovskite phase transition and mineral chemistry in the pyrolitic lowermost mantle. *Geophysical Research Letters, 32*(3), L03304. doi:10.1029/2004GL021956

Niwa, K., Yagi, t., Ohgushi, K., Merkel, S., Miyajima, N., & Kikegawa, T. (2007). Lattice preferred orientation in CaIrO3 perovskite and post-perovskite formed by plasitc deformation under pressure. *Physics and Chemistry of Minerals, 34*(9), 679-686.

Nowacki, A., Walker, A., Wookey, J., & Kendall, J. (2013). Evaluating post-perovskite as a cause of D" anisotropy in regions of palaeosubduction. *Geophysical Journal International, 192*(3), 1085-1090. doi:10.1093/gji/ggs068

Nye, J. F. (1956). *The physical properties of crystals.* Oxford, UK: Clarendon Press.

Oganov, A., & Ono, S. (2004). Theoretical and experimental evidence for a post-perovskite phase of MgSiO3 in Earth's D" layer. *Nature, 430*(6998), 445-448. doi:10.1038/nature02701

Oganov, A., Martonak, R., Laio, A., Raiteri, P., & Parrinello, M. (2005). Anisotropy of Earth's D" layer and stacking faults in the MgSiO3 post-perovskite phase. *Nature, 438*(7071), 1142-1144. doi:10.1038/nature04439

Ohta, K., Hirose, K., Sata, N., & Ohishi, Y. (2006). The sharpness and compositional effects on post-perovskite phase transition. *Geochimica Et Cosmochimica Acta, 70*(18), A454.

Okada, T., Yagi, T., Niwa, K., & Kikegawa, T. (2010). Lattice-preffered orientations in post-perovskite-type MgGeO3 formed by transforamtions from different pre-phases. *Physics of the Earth and Planetary Interiors, 180*(3), 195-202. doi:10.1016/j.pepi.2009.08.002

Panning, M., & Romanowicz, B. (2004). Inferences on flow at the base of Earth's mantle based on seismic anisotropy. *Science, 303*(5656), 351-353. doi:10.1126/science.1091524

Panning, M., & Romanowicz, B. (2006). A three-dimensional radially anisotropic model of shear velocity in the whole mantle. *Geophysical Journal International, 167*(1), 361-379. doi:10.1111/j.1365-246X.2006.03100.x

Plancon, A., Tsipurski, S. I., & Drits, V. A. (1985). Calculation of intensity distribution in the case of oblique texture electron diffraction. *Journal of Applied Crystallography, 18*(4), 191-196.

Popa, N., & Balzar, D. (2002). An analytical approximation for a size-broadened profile given by the log normal and gamma distributions. *Journal of Applied Crystallography, 35*(3), 338-346. doi:10.1107/S0021889802004156

Randle, V., & Engler, O. (2000). *Introduction to texture analysis: Macrotexture, microtexture and orientation mapping.* London: Gordon and Breach Science.

Reuss, A. (1929). Berechnung der Fließgrenze von Mischkristallen auf Grund der plastizitätsbedingung für Einkristalle. *Zeitschrift für Angewandte Mathematik und Mechanik, 9*, 49-58.

Rietveld, H. M. (1969). A profile refinement method for nuclear and magnetic structures. *Journal of Applied Crystallography, 2*(2), 65-71.

Rodi, V., & Babel, D. (1965). Ternäre Oxide der Übergangsmetalle. IV. Erdalkaliiridium(IV)-oxide: Kristallstruktur von CaIrO3. *Zeitschrift Für Anorganische Und Allgemeine Chemie, 366*, 17-23.

Santillan, J., Shim, S., Shen, G., & Prakapenka, V. (2006). High-pressure phase transition in Mn2O3: Application for the crystal structure and preferred orientation of the CaIrO3 type. *Geophysical Research Letters, 33*(15), L15307. doi:10.1029/2006GL026423

Sayers, C. M. (1994). The elastic anisotropy of shales. *Journal of Geophysical Research, 99*(B1), 767-774. doi:10.1029/93JB02579

Shim, S. (2008). The postperovskite transition. *Annual Review of Earth and Planetary Sciences, 36*, 569-599. doi:10.1146/annurev.earth.36.031207.124309

Shim, S., Duffy, T., Jeanloz, R., & Shen, G. (2004). Stability and crystal structure of MgSiO3 perovskite to the core-mantle boundary. *Geophysical Research Letters, 31*(10), L10603. doi:10.1029/2004GL019639

Smith, M. E., Singer, B., & Carroll, A. (2003). 40Ar/39Ar geochronology of the Eocene Green River Formation, Wyoming. *GSA Bulletin, 115*(5), 549-565. doi:10.1130/0016-7606(2003)115<0549:AGOTEG>2.0.CO;2

Tackley, P. (2000). Mantle convection and plate tectonics: Toward an integrated physical and chemical theory. *Science, 288*(5473), 2002-2007. doi:10.1126/science.288.5473.2002

Tateno, S., Hirose, K., Sata, N., & Ohishi, Y. (2005). Phase relations in Mg3Al2Si3O12 to 180 GPa: Effect of Al on post-perovskite phase transition. *Geophysical Research Letters, 32*(15), L15306. doi:10.1029/2005GL023309

Thomsen, I. (1986). Weak elastic anisotropy. *Geophysics, 51*(10), 1954-1966.

Tsuchiya, T., & Tsuchiya, J. (2007). Structure and elasticity of Cmcm CaIrO3 and their pressure dependences; Ab initio calculations. *Physical Review B, 76*(14), 144119. doi:10.1103/PhysRevB.76.144119

Tsuchiya, T., Umemoto, K., Wentzcovitch, R., & Tsuchiya, J. (2004). Elasticity of post-perovskite MgSiO3. *Geophysical Research Letters, 31*(14), L14603. doi:10.1029/2004GL020278

Valcke, S. A., Casey, M., Lloyd, G. E., Kendall, J.-M., & Fisher, Q. J. (2006). Lattice preferred orientation and seismic anisotropy in sedimentary rocks. *Geophysical Journal International, 166*(2), 652-666. doi:10.1111/j.1365-246X.2006.02987.x

Vanden Berg, M. D. (2008). Basin-wide evaluation of the uppermost Green River Formation's oil-shale resource, Uinta Basin, Utah and Colorado. *Utah Geological Survey Special Study, 129*, 19.

Voigt, W. (1928). *Lehrbuch der Kristallphysik.* Leipzig: Teubner-Verlag.

Voltolini, M., Wenk, H.-R., Mondol, N. H., Björlykke, K., & Jahren, J. (2009). Anisotropy of experimentally compressed kaolinite-illite-quartz mixtures. *Geophysics, 74*(1), 13-23. doi:10.1190/1.3002557

Walte, N., Heidelbach, F., Miyajima, N., & Frost, D. (2007). Texture development and TEM analysis of deformed CaIrO3: Implications for the D" layer at the core-mantle boundary. *Geophysical Research Letters, 34*(8), L08306. doi:10.1029/2007GL029407

Walte, N., Heidelbach, F., Miyajima, N., Frost, D., Rubie, D., & Dobson, D. (2009). Transformation textures in post-perovskite: Understanding mantle flow in the D" layer of the Earth. *Geophysical Research Letters, 36*(4), L04302. doi:10.1029/2008GL036840

Wang, Z. (2002). Seismic anisotropy in sedimentary rocks: Part 2 - Laboratory Data. *Geophysics, 67*(5), 1423-1440. doi:10.1190/1.1512743

Wenk, H.-R. (1991). Standard project for pole-figure determination by neutron diffraction. *Journal of Applied Crystallography, 24*(5), 920-927. doi:10.1107/S0021889891004661

Wenk, H.-R., & Grigull, S. (2003). Synchrotron texture analysis with area detectors. *Journal of Applied Crystallography, 36*(4), 1040-1049. doi:10.1107/S0021889803010136

Wenk, H.-R., & Van Houtte, P. (2004). Texture and anisotropy. *Reports on Progress in Physics, 67*(8), 1367.

Wenk, H.-R., Cottaar, S., Tome, C. N., McNamara, A., & Romanowicz, B. (2011). Deformation in the lowermost mantle: From polycrystal plasticity to seismic anisotropy. *Earth and Planetary Science Letters, 306*(1), 33-45. doi:10.1016/j.epsl.2011.03.021

Wenk, H.-R., Franz, H., Nihei, K., & Nakagawa, S. (2007). Preferred orientation and elastic anisotropy of illite-rich shale. *Geophysics, 72*(2), E69-E75. doi:10.1190/1.2432263

Wenk, H.-R., Kanitpanyacharoen, W., & Voltolini, M. (2010). Preferred orientations of phyllosilicates. Comparison of fault gouge, shale and schist. *Journal of Structural Geology, 32*(4), 478-489. doi:10.1016/j.jsg.2010.02.003

Wenk, H.-R., Lutterotti, L., Kaercher, P., Kanitpanyacharoen, W., Miyagi, L., & Vasin, R. (2014). Rietveld texture analysis from synchrotron diffraction images. II. Complex multiphase materials and diamond anvil cell experiments. *Powder Diffraction, 29*(3), 220-232. doi:10.1017/S0885715614000360

Wenk, H.-R., Matthies, S., Donovan, J., & Chateigner, D. (1998). BEARTEX: A windows-based program system for quantitative texture analysis. *Journal of Applied Crystallography, 31*(2), 262-269. doi:10.1107/S002188989700811X

Wenk, H.-R., Voltolini, M., Kern, H., Popp, T., & Mazurek, M. (2008b). Anisotropy in shale from Mont Terri. *The Leading Edge, 27*(6), 742-748.

Wenk, H.-R., Voltolini, M., Mazurek, M., van Loon, L. R., & Vinsot, A. (2008a). Preferred orientations and anisotropy in shales. Callovo-Oxfordian shale (France) and Opalinus Clay (Switzerland). *Clays and Clay Minerals, 56*(3), 285-306.

Wookey, J., & Dobson, D. (2008). Between a rock and a hot place: The core-mantle boundary. *Philosophical Transactions of the Royal Society of London A: Mathematical, Physical and Engineering Sciences, 366*(1885). doi:10.1098/rsta.2008.0184

Wookey, J., & Kendall, J. (2007). Seismic anisotropy of post-perovskite and the lowermost mantle. In K. Hirose, D. Yuen, T. Lay, & J. P. Brodholt (Eds.), *Post-perovskite, the last mantle phase transition* (pp. 171-189). Washington, DC: American Geophysical Union.

Wookey, J., Stackhouse, S., Kendall, J., Brodholt, J., & Price, G. (2005). Efficacy of the post-perovskite phase as an explanation for lowermost-mantle seismic properties. *Nature, 438*(7070), 1004-1007. doi:10.1038/nature04345

Yamazaki, D., Yoshino, T., Ohfuji, H., Ando, J., & Yonedu, A. (2006). Origin of seismic anisotropy in the D" layer inferred from shear deformation experiments on post-perovskite phase. *Earch and Planetary Science Letters, 252*(3), 372-378. doi:10.1016/j.epsl.2006.10.004

Yoshida, S. (2000). Facies architecture and sequence stratigraphy of the Blackhawk Formation and the Castlegate Sandstone (Upper Cretaceous), Book Cliffs, Utah, USA. *Sedimentary Geology, 136*(3), 239-276. doi:10.1016/S0037-0738(00)00104-4